On the System Level Performance of MC-CDMA Systems in the Downlink

Article · January 2006

CITATIONS
9

READS
280

1 author:

Alain Mourad
InterDigital
79 PUBLICATIONS **1,561** CITATIONS

SEE PROFILE

On the System Level Performance of MC-CDMA Systems in the Downlink

Abdel-Majid Mourad

N° d'ordre : 2006TELB0005

THÈSE

Présentée à

l'ECOLE NATIONALE SUPERIEURE DES TELECOMMNUNICATIONS DE BRETAGNE

en habilitation conjointe avec l'Université de RENNES 1

pour obtenir le grade de

DOCTEUR de l'ENST Bretagne

Mention **Traitement du Signal et Télécommunication**

par

Abdel-Majid MOURAD

ON THE SYSTEM LEVEL PERFORMANCE OF MC-CDMA SYSTEMS IN THE DOWNLINK

PERFORMANCES AU NIVEAU SYSTÈME DES TRANSMISSIONS MC-CDMA EN VOIE DESCENDANTE

Soutenue le 10 janvier 2006 devant la Commission d'Examen :

Composition du Jury

- *Rapporteurs* : Luc VANDENDORPE, Professeur, UCL, Louvain, Belgique
  Djamal ZEGHLACHE, Professeur, INT, Evry, France
- *Examinateurs* : Ghaïs ELZEIN, Professeur, INSA, Rennes, France
  Xavier LAGRANGE, Professeur, ENST Bretagne, Rennes, France
  Jacques PALICOT, Professeur, SUPELEC, Rennes, France
  Ramesh PYNDIAH, Professeur, ENST Bretagne, Brest, France

This work has been carried out at MITSUBISHI ELECTRIC
Information Technology Centre Europe B.V. (ITE-TCL)

1, Allée de Beaulieu – CS 10806 – 35708 Rennes Cedex 7 – France
Tel: +33 (0)2 23 45 58 58 – Fax: +33 (0)2 23 45 58 59
www.mitsubishi-electric-itce.fr

Acknowledgments

First and foremost, I would like to thank Allah, praised and exalted is He, for giving me patience and helping me finish this thesis.

Many are those who have supported, encouraged, and helped me during this thesis, and it is a pleasure to acknowledge their guidance and support. I would like to begin by expressing my gratitude to my industrial advisor at Mitsubishi Electric ITE-TCL Arnaud Guéguen for his guidance and technical assistance. I wish to express sincere thanks to my academic advisor at ENST Bretagne, Professor Ramesh Pyndiah, for his support all along the past three years.

I wish to thank the company Mitsubishi Electric ITE-TCL and ANRT French foundation for providing me with generous financial support. I am grateful to my colleagues in the *Radio Access Techniques* team Damien Castelain, Loïc Brunel, and David Mottier for their support and their many appropriate suggestions to the manuscript and oral presentation of my thesis. A special thanks to the CEO Jean-Pierre Coudreuse and all my colleagues at ITE-TCL for their patience and encouragement. I would particularly like to thank Magali, Marie, Jacqueline, Louis-Marie, Issam, Mohamad, Nicolas, Thomas, Nathalie, Gwillerm, Christophe, and Stéphane.

I am thankful to Professor Ghaïs Elzein for honoring me by accepting to be the chair of my committee. I am grateful to Professor Luc Vandendorpe and Professor Djamal Zeghlache for their careful review of my work, and to Professor Xavier Lagrange and Professor Jacques Palicot for accepting to participate to my committee and for their valuable remarks.

I would like to thank all my friends for their friendship and in particular Khadija, Ali, Jad, Chadi, Samer, Mirna, and Brigitte.

Finally, I would like to dedicate this work to my parents, brothers Ayman, Hussein, and Ali, and sisters Youmna and Jana for standing with me throughout both difficult and good times, and for their patience and love.

To my parents, brothers Ayman, Hussein, and Ali, and sisters Youmna and Jana.

Abdel-Majid
February 2, 2006.

Abstract

The MC-CDMA multi-carrier spread spectrum scheme is a potential candidate for the air interfaces of future mobile radio systems. This scheme benefits from the robustness of OFDM multi-carrier transmission to multi-path propagation on one hand and on the other hand from the flexibility of CDMA code division multiple access technique. This thesis investigates the system level performance of MC-CDMA scheme in the downlink. The goal is to validate at the system level the concepts and algorithms of MC-CDMA physical layer.

The thesis addresses two connected themes. The first theme concerns the abstraction of the physical layer at the system level. This theme is also referred to as the link to system level interfacing. The main objective of the physical layer abstraction is to define an adequate measure that allows to predict the transmission quality at the system level. In this thesis, we consider the physical layer abstraction with respect to two time scales. The first time scale is macroscopic and averages the transmission of several data frames experiencing independent channel fading realizations. The second time scale is microscopic and includes only one data frame experiencing a particular channel fading realization. The macroscopic abstraction is appropriate for evaluating the system level performance through static system level simulations, whereas the microscopic abstraction is more appropriate for more accurate evaluation of the system level performance and for proper investigation of link adaptation algorithms through dynamic system level simulations. In our study, we analyze the problems raised by the two types of abstraction and propose novel and appropriate solutions.

The second theme concerns the evaluation of the cellular capacity performances of the MC-CDMA physical layer for different algorithms and configurations. Using the macroscopic abstraction, we develop a semi-analytical methodology for evaluating the cellular capacity. The capacity is evaluated at both the link level through a novel capacity indicator and at the system level through Monte Carlo static system simulations. The methodology developed here is a pragmatic and efficient tool to identify the physical layer configurations that are best suited for a given environment.

Keywords - MC-CDMA, interference modeling, link to system interface, cellular capacity, system level simulations.

Abrégé en Français

La technique de transmission multi-porteuse à étalement de spectre, MC-CDMA, est un candidat potentiel pour les interfaces radio des futurs systèmes radio mobiles. Cette technique bénéficie d'une part de la robustesse de la transmission multi-porteuse OFDM face à la propagation multi-trajets et d'autre part de la flexibilité de l'accès multiple à répartition par codes CDMA. Cette thèse s'intéresse à l'étude des performances systèmes de la technique MC-CDMA en voie descendante. L'objectif est de valider au niveau système les concepts et algorithmes de la couche physique MC-CDMA.

La thèse s'articule autour de deux thématiques qui sont liées. La première thématique concerne l'abstraction de la couche physique au niveau système. Cette thématique est aussi connue sous le nom d'interfaçage entre les niveaux lien physique et système. L'abstraction de la couche physique a pour principal objectif de définir une mesure adéquate pour prédire la qualité de transmission au niveau système. Dans cette thèse, nous étudions l'abstraction de la couche physique suivant deux échelles de temps. La première échelle est macroscopique et porte sur la transmission de plusieurs trames de données subissant des évanouissements de canal indépendants. La deuxième échelle est dite microscopique et porte sur la transmission d'une seule trame de données subissant un évanouissement particulier du canal. L'abstraction macroscopique est appropriée pour une évaluation des performances systèmes par des simulations systèmes statiques alors que l'abstraction microscopique est plus appropriée pour une évaluation plus précise des performances systèmes ainsi que pour étudier les algorithmes d'adaptation de lien par des simulations systèmes dynamiques. Dans notre étude, nous analysons les problèmes soulevés par les deux types d'abstraction et proposons des nouvelles solutions appropriées.

La deuxième thématique concerne l'évaluation de la capacité cellulaire des algorithmes et configurations de la couche physique MC-CDMA. En utilisant l'abstraction macroscopique, nous développons une méthodologie semi analytique d'évaluation de la capacité cellulaire. L'évaluation de la capacité est faite aussi bien au niveau lien à travers un nouvel indicateur de capacité qu'au niveau système à travers un simulateur statique de type Monte Carlo. La méthodologie développée ici est un outil simple et efficace pour identifier les algorithmes et configurations de couche physique les mieux adaptés pour un environnement donné.

Mots clefs - MC-CDMA, modélisation d'interférence, interfaçage lien système, capacité cellulaire, simulations systèmes.

Publications and Patents

[1] A.-M. Mourad, A. Guéguen, "Method of Determining a Metric for Evaluating the Transmission Quality of a Data Frame Transmitted by a Communication System," *European Patent* 04290765.2, filing Dec. 2004.

[2] A.-M. Mourad, A. Guéguen, R. Pyndiah, "Impact of the MC-CDMA Physical Layer Algorithms on the Downlink Capacity in a Multi-Cellular Environment," *Proc. of the 62nd IEEE Vehicular Technology Conference Fall 2005 (VTCF'05)*, Sep. 2005.

[3] A.-M. Mourad, A. Guéguen, R. Pyndiah, "Quantifying the Impact of the MC-CDMA Physical Layer Algorithms on the Downlink Capacity in a Multi-Cellular Environment," *Proc. of the 5th IEEE International Workshop on Multi-Carrier Spread Spectrum (MCSS'05),* Sep. 2005.

[4] A.-M. Mourad, A. Guéguen, R. Pyndiah, "Interface between Link and System Level Simulations for Downlink MC-CDMA Cellular Systems," *Proc. of the 11th European Wireless Conference 2005 (EWC'05),* Apr. 2005.

[5] A.-M. Mourad, A. Guéguen, R. Pyndiah, "Impact of the Spreading Sequences on the Performance of Forward Link MC-CDMA Systems," *Proc. of the 8th IEEE International Symposium on Spread Spectrum Techniques and Applications (ISSSTA'04)*, pp. 683-687, Aug. 2004.

[6] A.-M. Mourad, A. Guéguen, R. Pyndiah, "MAI Analysis for Forward Link Mono-Dimensionally Spread OFDM Systems," *Proc. of the 59th IEEE Vehicular Technology Conference Spring 2004 (VTCS'04)*, vol. 3, pp. 1528-1533, May 2004.

Table of Contents

List of Figures

List of Tables

Abbreviations

AAS	Arithmetic Average SINR
AFD	Average Fade Duration
AFM	Adjacent Frequency chip Mapping
ARQ	Automatic Repeat Request
ASK	Amplitude Shift Keying
AWGN	Additive White Gaussian Noise
BER	Bit Error Rate
CDF	Cumulative Distribution Function
CDMA	Code Division Multiple Access
CES	Chi-square Effective SINR
CLT	Central Limit Theorem
DFT	Discrete Fourier Transform
DS-CDMA	Direct Sequence CDMA
EES	Exponential Effective SINR
EGC	Equal Gain Combining
FDMA	Frequency Division Multiple Access
FER	Frame Error Rate
FH-CDMA	Frequency Hopping CDMA
FHT	Fast Hadamard Transform
GAS	Geometric Average SINR
GCES	Generalized Chi-square Effective SINR
GEES	Generalized Exponential Effective SINR
GSM	Global System for Mobile Communication
HIPERLAN2	High Performance Radio Local Area Network Type 2
HIPERMAN	High Performance Radio Metropolitan Area Network
IC	Interference Cancellation
ICI	Inter-Carrier Interference
IDFT	Inverse Discrete Fourier Transform
IFM	Interleaved Frequency chip Mapping
ISI	Inter-Symbol Interference
IS-95	Interim Standard for US code division multiple access
LCR	Level Crossing Rate
LDPC	Low-Density Parity-Check
LLN	Law of Large Numbers
LLR	Log Likelihood Ratio
LMSE	Least Mean Square Error
LOS	Line Of Sight
LQM	Link Quality Measure

MAI	Multiple Access Interference
MBES	Minimum Based Effective SINR
MC-CDMA	Multi-Carrier CDMA
MC-DS-CDMA	Multi-Carrier DS-CDMA
MCS	Modulation and Coding Scheme
ML	Maximum Likelihood
MMSEC	Minimum Mean Square Error Combining
MRC	Maximal Ratio Combining
MT-CDMA	Multi-Tone CDMA
MUD	Multi-User Detection
OFDM	Orthogonal Frequency Division Multiplex
OGN	Orthogonal Gaussian Noise
ORC	Orthogonality Restoring Combining
PAPR	Peak to Average Power Ratio
PDC	Pacific Digital Cellular
PDF	Probability Density Function
PIC	Parallel Interference Cancellation
PN	Pseudo Noise
PSK	Phase Shift Keying
QAM	Quadrature Amplitude Modulation
QoS	Quality of Service
QPSK	Quadrature Phase Shift Keying
RF	Radio Frequency
RGEES	Refined Generalized Exponential Effective SINR
RGCES	Refined Generalized Chi-square Effective SINR
SIC	Serial Interference Cancellation
SINR	Signal to Interference plus Noise Ratio
SSMA	Spread Spectrum Multiple Access
SUD	Single User Detection
TDMA	Time Division Multiple Access
TTI	Transmission Time Interval
UMTS	Universal Mobile Telecommunication System
W-CDMA	Wideband CDMA
WLAN	Wireless Local Area Network
WLL	Wireless Local Loop
ZF	Zero Forcing

Notations

x, X	Scalar variable
$\mathbf{x}$	Vector
$\mathbf{X}$	Matrix
$\{x_n\}$	Set of the variables x_n, $n = 1 \ldots N$
$\mathbf{x}^T$	Transpose of vector $\mathbf{x}$
z^*	Complex conjugate of variable z
$\Re(z)$	Real part of complex variable z
$\Im(z)$	Imaginary part of complex variable z
$\|z\|$	Magnitude of complex variable z
$\mathbf{z}^H$	Hermitian, i.e., transpose conjugate, of complex vector $\mathbf{z}$
$\|\|\mathbf{z}\|\|^2$	Euclidean norm of complex vector $\mathbf{z}$
$\mathbf{A}^{-1}$	Inverse of matrix $\mathbf{A}$
$\mathbf{I}$	Identity matrix
$\mathbf{0}$	All zero vector
$\mathbf{1}$	All one vector
$\text{diag}(x_0, \ldots, x_{N-1})$	Diagonal matrix with diagonal elements $\{x_n\}$
$\prod x_n$	Product of the N elements $\{x_n\}$
$\sum x_n$	Summation of the N elements $\{x_n\}$
$\text{E}\{x\}$	Expectation value of random variable z
$\text{var}\{x\}$	Variance of random variable z
$\Pr\{\text{A}\}$	Probability of event A to occur
p_x	Probability density function of random variable x
$\Pr\{\text{A}\|\text{B}\}$	Probability of event A conditioned on event B
$\propto$	Proportional to
$\approx$	Approximately equal to
$\otimes$	Convolutional product
$\circ$	Compound function, $f \circ g(x) = f(g(x))$
$\text{argmin}(f(x))$	Value of x that minimizes the function $f(x)$
$\text{argmax}(f(x))$	Value of x that maximizes the function $f(x)$
$\delta(x)$, δ_{ij}	Dirac and Kronecker delta functions
e^x, $\exp(x)$	Exponential function
$Q(x)$	Complementary error function
$J_0(x)$	Zero-order Bessel function of the first kind
$\text{rect}_T(t)$	Rectangular function

Résumé en Français

1 Contexte

Afin de fournir de nouveaux services attractifs pour les abonnés avec une meilleure qualité de service, une quatrième génération (4G) des systèmes radio mobiles est attendue sur le marché dans les 5 à 10 années à venir. Le MC-CDMA est une technique de transmission prometteuse pour l'interface radio en voie descendante des futurs systèmes 4G. Elle a fait l'objet de nombreux projets collaboratifs tels que les projets européens IST MATRICE, 4MORE et WINNER, et aussi de nombreux projets internes aux grands opérateurs comme NTT DoCoMo au Japon et France Télécom en France.

Le MC-CDMA combine la transmission multi-porteuse OFDM avec la technique d'accès multiple à répartition par codes CDMA. L'OFDM est couramment utilisée dans les systèmes récents de communication sans fils. Elle bénéficie de nombreux avantages comme par exemple une capacité à fournir un haut débit tout en restant robuste face à la propagation multi-trajets, une mise en œuvre simplifiée avec les opérations IDFT et DFT et une faible complexité du récepteur grâce à une égalisation dans le domaine fréquentiel. Le CDMA quant à lui est un accès multiple très flexible qui offre une grande capacité cellulaire et une planification fréquentielle simple du réseau. Il est notamment utilisé dans le système radio mobile de troisième génération l'UMTS.

Le but de la thèse est de valider au niveau système les concepts de la couche physique MC-CDMA en voie descendante dans le contexte des futurs systèmes 4G. Une telle validation est nécessaire pour mettre en évidence l'apport en terme de la capacité cellulaire des algorithmes de la couche physique MC-CDMA en voie descendante.

2 Problématique

L'évaluation des performances d'un système radio mobile peut se faire à deux niveaux : le niveau lien et le niveau système, avec une interface adéquate entre les deux niveaux.

Le niveau lien comporte un émetteur, un canal multi-trajets et un récepteur. Sa granularité est très fine et elle est considérée au niveau bit. Le principal objectif au niveau lien est d'étudier l'impact des algorithmes de la couche physique sur la qualité de transmission de l'information binaire. Le but est de concevoir une couche physique efficace et robuste face aux effets de la propagation multi-trajets et de l'interférence multi-utilisateurs. Les performances sont mesurées par les courbes traditionnelles de taux d'erreurs binaires en

fonction du rapport E_b/N_0, où E_b est l'énergie émise par bit d'information et N_0 est la densité spectrale de puissance du bruit.

Le niveau système quant à lui comporte plusieurs stations de base et tous les utilisateurs qui y sont connectés. Sa granularité est plus large et elle est considérée au niveau trame(s) de données. L'objectif au niveau système est d'étudier les performances globales du système qui sont typiquement caractérisées par la capacité cellulaire, le débit effectif et la couverture. Le but ici est de concevoir des algorithmes appropriés aussi bien de couche physique que de gestion de ressources radios et de couches supérieures.

En raison de sa granularité très fine, la couche physique ne peut pas être intégrée au niveau système, ce qui soulève le problème d'abstraction de la couche physique au niveau système. Ce problème connu sous le nom d'interfaçage entre les niveaux lien et système consiste à définir une méthode appropriée pour permettre la prédiction de la qualité de transmission au niveau système.

Dans la thèse, nous adressons le problème d'interfaçage entre les niveaux lien et système pour la couche physique MC-CDMA en voie descendante. Nous adressons également l'évaluation de la capacité cellulaire pour identifier les algorithmes et configurations de la couche physique MC-CDMA les mieux adaptés pour un environnement donné.

3 Objectifs

La thèse a deux principaux objectifs qui sont présentés ci-après.

3.1 Interfaçage Lien Système

Le premier objectif concerne l'interfaçage lien système spécifique au MC-CDMA. Il s'agit de définir une méthode simple et précise pour la prédiction de la qualité de transmission au niveau système. Dans la thèse, nous étudions deux types d'interfaçage selon que la qualité de transmission est mesurée sur une échelle de temps macroscopique ou microscopique. Le premier type d'interfaçage est orienté multi-trame. Il est caractérisé par une échelle de temps macroscopique qui porte sur un grand nombre de trames subissant des évanouissements de canal indépendants. Le deuxième type d'interfaçage est orienté trame avec une échelle de temps microscopique qui porte sur une seule trame de données subissant un évanouissement particulier du canal. L'interfaçage orienté multi-trame trouve sa principale application dans un simulateur système statique pour mener des études préliminaires au niveau système dans le cas de services temps réels. L'interfaçage orienté trame quant à lui trouve son application

plutôt dans des simulations systèmes dynamiques pour mener des études plus avancées au niveau système et développer des mécanismes d'adaptation de lien et de gestion de ressources radios par exemple.

3.2 Évaluation de la Capacité Cellulaire

Le deuxième objectif de la thèse concerne l'évaluation de la capacité cellulaire pour différents algorithmes et configurations de la couche physique MC-CDMA. Le but est de définir une méthodologie qui permet d'identifier les algorithmes et configurations les mieux adaptés pour un environnement donné. La capacité cellulaire est définie par le nombre maximal d'utilisateurs simultanément servis avec une qualité de transmission suffisante. Nous avons choisi d'évaluer la capacité au niveau système au moyen d'un simulateur système statique de type Monte Carlo utilisant l'interface lien système orientée multi-trame.

4 Contenu et Contributions

La thèse comprend 7 chapitres dont le contenu et les contributions sont décrits ci-après.

Le chapitre 1 est introductif. Il décrit le contexte général de la thèse, les motivations et les contributions apportées, chapitre par chapitre.

Le chapitre 2 porte sur la modélisation du canal radio mobile avec ses deux composantes qui sont les atténuations à court et long terme. La composante à long terme est caractérisée par des évanouissements lents du signal dus à la distance et à l'effet de masque. La composante à court terme quant à elle est caractérisée par des évanouissements beaucoup plus rapides dus à la propagation par trajets multiples. Dans ce chapitre, nous présentons les modèles et caractéristiques de chaque composante. Nous validons aussi notre méthode choisie pour générer les évanouissements rapides du canal en utilisant des facteurs de mérite adéquats, comme le taux de dépassement d'un seuil et la durée moyenne d'un évanouissement en fonction de la fréquence Doppler. Les modèles présentés dans ce chapitre sont utilisés dans la suite de la thèse pour l'analyse et l'évaluation des performances aussi bien au niveau lien qu'au niveau système.

Dans le chapitre 3, nous passons en revue les systèmes OFDM et CDMA. Pour la transmission multi-porteuse OFDM, nous présentons son principe de base, sa mise en œuvre avec les opérations IDFT et DFT et ses principaux avantages et inconvénients. Nous développons aussi son modèle temps fréquence dans le cas le plus souvent considéré où l'interférence entre symboles est absorbée par l'intervalle de garde et le canal est invariant sur

la durée utile du symbole OFDM. Pour l'accès multiple à répartition par codes CDMA, nous décrivons son concept général et ses principaux points forts. Nous présentons également ses deux techniques de base : DS-CDMA et FH-CDMA. Nous terminons ce chapitre par une description des concepts généraux des quatre techniques multi-porteuses à étalement de spectre : MC-CDMA, MC-DS-CDMA, MT-CDMA et FLASH-OFDM.

Le chapitre 4 présente de manière plus détaillée la transmission MC-CDMA en voie descendante dans un environnement multi-cellulaire. Les principaux modules de l'émetteur de la station de base sont décrits : codage correcteur d'erreur, entrelacement, modulation, étalement, multiplexage, embrouillage et placement des chips. La structure du récepteur est ensuite exposée et la forme du signal reçu est présentée en présence de l'interférence intra-cellulaire et inter-cellulaire. L'interférence intra-cellulaire regroupe les contributions des utilisateurs connectés à la même station de base que l'utilisateur désiré, alors que l'interférence inter-cellulaire regroupe les contributions des autres stations de base, supposées toutes synchronisées. Les différentes techniques de détection sont présentées : mono-utilisateur (MRC, EGC, ORC et MMSEC) et multi-utilisateur (ML, ZF-MUD, MMSEC-MUD et IC). Dans ce chapitre, nous faisons le choix pragmatique de la détection mono-utilisateur pour des raisons de complexité du terminal mobile. La structure de l'interférence résiduelle après détection mono-utilisateur est précisée pour permettre une analyse de l'interférence dans la suite de la thèse.

4.1 Interface Lien Système Orientée Multi-trame

Le chapitre 5 se focalise sur l'interface lien système orientée multi-trame. Cette interface est caractérisée par une qualité de transmission mesurée par les taux d'erreurs binaires BER et FER moyennés sur un grand nombre de trames subissant des évanouissements de canal indépendants. Le problème à résoudre ici est de définir une mesure de qualité au niveau système permettant de prédire les BER et FER à partir du vecteur des puissances allouées aux utilisateurs. La relation entre la mesure de qualité et les BER et FER s'appelle la fonction de correspondance. Elle est obtenue au moyen des simulations au niveau lien. Idéalement, cette fonction devrait être invariante par rapport aux conditions de propagation et d'interférence au niveau système. De l'autre côté, la relation entre la mesure de qualité et le vecteur des puissances s'appelle la fonction de compression. Cette fonction devrait être simple à évaluer au niveau système.

Pour résoudre le problème, nous suivons une approche en trois étapes :

1) Analyse et modélisation de l'interférence intra-cellulaire et inter-cellulaire au niveau lien.
2) Analyse de la probabilité d'erreur binaire et identification d'une mesure de qualité.
3) Validation de la mesure de qualité identifiée au moyen d'un simulateur d'interface.

Dans la première étape, nous analysons les propriétés statistiques de l'interférence intra-cellulaire et inter-cellulaire en sortie du détecteur. Nous établissons d'abord des expressions mathématiques pour les facteurs d'interférence afin de pouvoir calculer de manière simple et précise la puissance reçue de l'interférence au niveau système. Nous montrons que les facteurs d'interférence intra-cellulaire varient avec le couple de codes d'étalement interférents (cf. Equation (5.5)), alors que le facteur d'interférence inter-cellulaire est fonction seulement du facteur d'étalement et de l'espérance du module au carré des coefficients d'égalisation du canal (cf. Equation (5.22)). Nous abordons ensuite la modélisation statistique de l'interférence intra-cellulaire et inter-cellulaire pour permettre de les prendre en compte de manière simple et précise au niveau lien. Nous montrons qu'un bruit gaussien orthogonal (OGN) est bien approprié pour modéliser l'interférence intra-cellulaire à l'émission (cf. Figure 5-2). Pour l'interférence inter-cellulaire, nous adoptons le modèle d'un bruit blanc gaussien additif (AWGN) en entrée du récepteur.

En utilisant les modèles OGN et AWGN respectivement pour l'inférence intra-cellulaire et inter-cellulaire, nous analysons dans la deuxième étape la probabilité d'erreur binaire (cf. Section 5.3). Nous montrons que dans le cas d'un canal non corrélé, la probabilité d'erreur binaire avec et sans codage est directement liée au SINR local moyen en sortie du détecteur. Ce SINR local moyen est tout simplement le rapport entre la puissance du signal utile et la puissance totale de l'interférence plus bruit en sortie du détecteur. Cependant, dans le cas d'un canal corrélé, le théorème de la limite centrale et la loi des grands nombres ne s'appliquent plus pour justifier l'existence d'une telle relation directe. Des simulations au moyen d'un simulateur d'interface sont donc nécessaires pour vérifier l'existence d'une relation directe entre la probabilité d'erreur binaire et le SINR local moyen en sortie du détecteur, ce que nous faisons dans la troisième étape.

Grâce aux expressions mathématiques des facteurs d'interférence et aux modèles OGN et AWGN pour l'interférence intra-cellulaire et inter-cellulaire, nous développons un simulateur d'interface précis et de faible complexité. Ce simulateur fournit les tables de correspondances entre le FER et le SINR local moyen en sortie du détecteur. Ces tables sont spécifiques à la configuration de la couche physique, au modèle du canal multi-trajets et au couple (charge

intra-cellulaire K_0, variance de l'interférence inter-cellulaire plus bruit $\sigma_{\xi+\nu}^2$). Le couple $(K_0,\sigma_{\xi+\nu}^2)$ est une représentation au niveau lien des conditions d'interférence au niveau système. Le but des simulations est de vérifier l'invariance de la relation SINR-FER avec le couple $(K_0,\sigma_{\xi+\nu}^2)$ pour conclure sur la pertinence du SINR local moyen comme mesure de qualité au niveau système.

Par simulations, nous montrons que la variance $\sigma_{\xi+\nu}^2$ a une influence négligeable sur la relation SINR-FER et ceci dans les deux cas corrélé et non corrélé (cf. Figure 5-4). Nous montrons que la charge intra-cellulaire K_0 a aussi une influence négligeable sur la relation SINR-FER mais seulement dans le cas d'un canal peu corrélé (cf. Figure 5-5). Ce dernier résultat confirme l'analyse théorique de la probabilité d'erreur binaire. Le SINR local moyen en sortie du détecteur est donc une mesure pertinente pour le cas peu corrélé mais mal adaptée pour le cas corrélé. Dans ce dernier cas, nous choisissons de l'utiliser avec différentes tables SINR-FER pour différentes valeurs de la charge intra-cellulaire K_0 en raison de son évaluation simple au niveau système.

4.2 Évaluation de la Capacité Cellulaire

Dans le chapitre 6, nous étudions la capacité cellulaire pour différents algorithmes et configuration de la couche physique MC-CDMA en voie descendante. Le but est d'identifier les algorithmes et configurations les mieux adaptés pour un environnement donné.

Nous considérons un système macro-cellulaire hexagonal régulier avec une cellule centrale entourée de plusieurs couches de cellules voisines. Une station de base est placée au centre de chaque cellule et les utilisateurs sont uniformément distribués dans le disque délimitant les cellules (cf. Figure 6-2). Les résultats sont collectés à la station de base centrale BS_0 alors que les autres stations de base sont supposées émettre avec une même puissance P_o.

La capacité est mesurée par le nombre maximal d'utilisateurs simultanément servis avec une qualité de transmission satisfaisante. Le problème d'évaluation de la capacité se traduit donc par un problème de satisfaction d'un FER cible pour les utilisateurs connectés à BS_0. En utilisant les tables de correspondance SINR-FER fournies par l'interface lien système orientée multi-trame, le problème est reformulé par la satisfaction d'un SINR cible pour les utilisateurs connectés à BS_0 tout en respectant une contrainte d'une puissance maximale d'émission P_{max}. Le SINR cible est spécifique à la configuration de la couche physique, au modèle du canal et à la charge intra-cellulaire K_0 de BS_0. Le problème de satisfaction du SINR cible revient à un problème d'allocation de puissance pour BS_0 (cf. Equation (6.8)). Nous montrons qu'une

solution positive au problème d'allocation de puissance existe si et seulement si une condition sur pôle est vérifiée. Cette condition s'exprime par une valeur propre maximale de la matrice des facteurs d'interférence intra-cellulaire inférieure à l'inverse du SINR cible.

A partir de la condition sur pôle, une capacité sur pôle est définie par la charge maximale de BS_0 vérifiant cette condition. Cette capacité correspond aussi à la charge maximale de BS_0 pour laquelle la puissance maximale de BS_0 tend vers l'infinie. En prenant en compte la contrainte de puissance limitée P_{max}, une capacité de coupure est définie par la charge maximale de BS_0 pour laquelle la probabilité que la condition sur pôle ou la contrainte de puissance limitée soit violée reste inférieure à un certain seuil de coupure ε (cf. Equation (6.11)). La capacité de coupure est évaluée au moyen d'un simulateur système statique de type Monte Carlo. Pour une configuration donnée de la couche physique, la capacité de coupure est mesurée par la charge maximale de BS_0 pour laquelle la fonction de répartition de la puissance de BS_0 respecte le seuil de coupure ε pour une puissance donnée P_{max} et une puissance d'émission donnée P_o des stations de base interférentes.

Par analyse théorique, nous montrons que la puissance de BS_0 se factorise en deux composantes. La première notée $C_\phi^{(0)}$ est spécifique à la configuration ϕ de la couche physique, au modèle du canal et à la charge de BS_0. La deuxième composante $T^{(0)}$ est spécifique aux paramètres au niveau système. Grâce à la loi des grands nombres, nous montrons que la composante $T^{(0)}$ est quasiment invariante par rapport à la charge de BS_0. Seule $C_\phi^{(0)}$ dépend donc de la charge, et par conséquent cette composante peut être utilisée comme un indicateur de capacité au niveau lien. L'indicateur de capacité ne dépend que de la charge de BS_0, du SINR cible, de la valeur propre de la matrice des facteurs d'interférence intra-cellulaire et du facteur d'interférence inter-cellulaire (cf. Equation (6.14)). Il est donc simple à évaluer à partir des résultats fournis par l'interface lien système orientée multi-trame. Pour une configuration donnée de la couche physique, nous obtenons une valeur de la capacité mesurée par la charge maximale de BS_0 pour laquelle l'indicateur de capacité reste inférieure à un certain seuil. L'indicateur de capacité permet donc de comparer la capacité pour différentes configurations de la couche physique relativement à un certain seuil donné. La seule limitation de l'indicateur de capacité au niveau lien est que la valeur de la capacité obtenue n'est pas associée à une grandeur physique contrairement à la capacité de coupure obtenue à partir du simulateur système.

Par simulations, nous évaluons la capacité pour différentes configurations de la couche physique MC-CDMA. Nous montrons une bonne concordance entre les résultats obtenus au moyen de l'indicateur de capacité au niveau lien et ceux obtenus au moyen du simulateur système. Nous montrons aussi l'intérêt d'utiliser la capacité comme facteur de mérite pour comparer les performances des configurations de la couche physique. A titre illustratif, voici quelques résultats obtenus dans un environnement urbain :

- La détection MMSEC fournie une capacité plus élevée que les détections EGC et MRC (cf. Figure 6-6 et Figure 6-9).
- Le placement fréquentiel adjacent des chips (AFM) est généralement plus performant que le placement fréquentiel entrelacé (IFM) (cf. Figure 6-6 et Figure 6-9).
- La modulation QPSK offre un débit supérieur à la modulation 16QAM dans la limite de son débit maximal accessible (cf. Figure 6-7 et Figure 6-10).
- Le turbo code de l'UMTS offre un gain de capacité de près de 30% par rapport au code convolutif de l'UMTS (cf. Figure 6-7 et Figure 6-10).

4.3 Interface Lien Système Orientée Trame

Le chapitre 7 aborde le problème d'interfaçage lien système orienté trame. Ici, l'échelle de temps porte sur une seule trame de données subissant un évanouissement particulier du canal. La qualité de transmission est mesurée par la probabilité d'erreur binaire conditionnée par l'évanouissement particulier du canal. L'interface orientée trame est utile pour l'évaluation des performances au niveau système au moyen d'un simulateur système dynamique et aussi pour la conception d'algorithmes d'adaptation de lien et de gestion de ressources radios.

Le problème à résoudre ici est de définir une fonction adéquate pour prédire la probabilité d'erreur conditionnelle à partir du vecteur des SINR instantanés des bits dans la trame. La fonction de prédiction doit remplir certaines conditions comme l'invariance par rapport à la réalisation particulière du canal, au profil du canal multi-trajets et aux paramètres au niveau système, et le fait qu'elle reste valable pour différents schémas de codage et de modulation par un simple changement de valeur des paramètres génériques.

Nous analysons le problème suivant le concept du SINR effectif pour les transmissions avec codage convolutif. Le SINR effectif introduit par Sanjiv N. et al. en 1998 est défini par le SINR sur un canal gaussien produisant la même probabilité d'erreur binaire que le vecteur des SINR instantanés sur un canal à évanouissements. Dans ce chapitre, nous passons en

revue l'état de l'art des principales solutions de SINR effectif et nous proposons de nouvelles solutions. La solution de l'état de l'art la plus couramment utilisée s'appelle le SINR effectif exponentiel généralisé (GEES). Cette solution introduite dans le cadre du 3GPP en 2003 fait l'hypothèse que les positions des bits erronés dans la trame sont indépendantes et uniformément distribuées sur la trame. Le GEES est fonction d'un paramètre β et il nécessite le calcul de la somme des exponentielles des SINR des symboles modulés dans la trame (cf. Equation (7.25)). Nous proposons une nouvelle solution que l'on nomme le SINR effectif de χ^2 généralisé (GCES). Dans cette nouvelle solution, nous supposons que la somme des SINR des bits erronés dans la trame suit une loi de χ^2 non centrée. Nous obtenons une forme simple pour le GCES qui nécessite le calcul de la moyenne et de la variance des SINR des symboles modulés dans la trame (cf. Equation (7.27)). La mise en œuvre du GCES est donc plus simple que le GEES.

Les solutions GEES et GCES sont obtenues par généralisation intuitive d'une analyse de la probabilité d'erreur par paire d'un décodeur de Viterbi utilisant la modulation QPSK. Par analyse avancée de la probabilité d'erreur par paire d'un décodeur de Viterbi utilisant la modulation d'ordre supérieure 16QAM, nous proposons des raffinements pour le GEES et GCES qu'on nomme respectivement RGEES et RGCES. Ces raffinements utilisent deux paramètres β_1 et β_2 au lieu d'un seul paramètre β utilisé dans GEES et GCES (cf. Equations (7.41) et (7.43)).

Nous comparons les performances de différentes solutions de l'état de l'art et des nouvelles solutions proposées dans le contexte de la couche physique MC-CDMA. La comparaison des performances est basée sur la différence entre les valeurs du SINR effectif en dB obtenues par prédiction et par simulation. Nous montrons que la solution proposée RGEES offre les meilleures performances avec une différence maximale sur 95% du temps inférieure à 0.1 dB pour les deux modulations QPSK et 16QAM. La solution RGCES quant à elle offre des très bonnes performances légèrement inférieures à celles de RGEES (une différence maximale sur 95% inférieure à 0.15 dB au lieu de 0.1 dB pour le RGEES (cf. Tables 7-2 et 7-3)). Par contre, elle est plus simple à mettre en œuvre que la RGEES ce qui constitue son principal intérêt.

5 Conclusions et Perspectives

La thèse s'intéresse à l'étude des performances au niveau système de la couche physique MC-CDMA en voie descendante. Elle se focalise sur la problématique d'interfaçage entre le

niveau lien et le niveau système ainsi que sur l'évaluation de la capacité cellulaire pour différents algorithmes et configurations de la couche physique. L'interfaçage lien système est étudié suivant deux échelles de temps : *multi-trame* portant sur un grand nombre de trames de données et *trame* portant sur une seule trame de données. Sur l'échelle multi-trame, nous avons développé une interface précise et de faible complexité. Cette interface utilise le SINR local moyen en sortie du détecteur comme mesure de qualité au niveau système. Sur l'échelle trame, nous avons analysé le problème d'interfaçage suivant le concept du SINR effectif. Nous avons étudié différentes solutions de l'état de l'art et nous avons proposé de nouvelles solutions très performantes. En utilisant l'interface orientée multi-trame, nous avons développé un outil simple et efficace pour évaluer la capacité cellulaire pour les algorithmes et configurations de la couche physique MC-CDMA. Cet outil comprend un indicateur de capacité au niveau lien et un simulateur système statique de type Monte-Carlo.

La thèse ouvre la voie à de plusieurs perspectives parmi lesquelles nous citons :

1) Quantifier les gains de capacité cellulaire apportés par les techniques d'antennes multiples dans le contexte de la couche physique MC-CDMA en voie descendante.
2) Évaluer la capacité cellulaire pour la couche physique OFDMA et comparaison avec la couche physique MC-CDMA, l'OFDMA étant un concurrent du MC-CDMA pour la voie descendante des futurs systèmes 4G.
3) Étudier l'application des nouvelles solutions proposées de SINR effectif aux systèmes utilisant les antennes multiples et les techniques de codage avancées.
4) Concevoir des algorithmes d'adaptation de lien et de gestion de ressources radios en utilisant l'interface lien système orientée trame.

Chapter 1
Introduction

1.1 Background and Context

At the beginning of the 1990s, the first generation of analog mobile radio systems was replaced by the current second generation (2G) digital systems, such as GSM, IS-95 and PDC. Basically, the 2G digital systems were designed and optimized to provide speech and low-rate data services. The evolution is still continuing today with the deployment of the third generation (3G) systems, such as UMTS and cdma2000. The objectives of 3G systems went far beyond 2G systems, especially with respect to the wide range of multimedia services, high and variable data rates, wide and scalable bandwidth, high QoS requirements, operability in different environments, and flexibility in radio resource management. While 3G systems are currently being deployed, there has been already a significant research activity towards what is frequently referred to as beyond 3G or 4G systems. The rapid growth of internet services and increasing interest in portable computing devices are likely to create a strong demand for new wireless multimedia services requiring higher data rates than what is provided by 3G systems. Especially in the downlink, higher data rates are needed to accommodate emerging and new multimedia services such as video streaming, but also large data files downloading. Besides offering new services with higher capacity and data rates, the goal of 4G systems is also to integrate the existing technologies in a common platform and to support multiple classes of terminals. Hence, a new generic high-performance technology is required for future 4G systems, starting with a new generic physical layer.

In the downlink, a broadband component is envisioned for 4G systems with an information bit rate in the range of 2-20 Mbit/sec for a vehicular environment and 50-100 Mbit/sec for indoor to pedestrian environments, using a 50-100 MHz bandwidth [1]. One of the most promising technologies for this broadband component is *Multi-Carrier Code Division Multiple Access* (MC-CDMA), which combines *Orthogonal Frequency Division Multiplex* (OFDM) modulation and *Code Division Multiple Access* (CDMA) technique. The main advantages of OFDM multi-carrier modulation are its robustness in frequency selective channels and its low-complexity receivers thanks to equalization in the frequency domain. The advantages of OFDM multi-carrier modulation on the one hand and the flexibility offered by CDMA spread spectrum multiple access technique on the other hand make MC-CDMA a

promising technology for broadband 4G systems. In the recent years, there has been a very strong focus on this technology, including the realization of prototypes and field trials [1][2].

The goal of this thesis is to validate at the system level the concepts and algorithms of MC-CDMA physical layer developed at the link level. The focus is on the downlink, where MC-CDMA has particularly proved its efficiency.

1.2 Problem Statement

A complete and realistic evaluation of the performance of a cellular system requires joint consideration of both microscopic and macroscopic aspects, from the microscopic level of binary information transmission to the macroscopic level of network control mechanisms. A typical cellular system usually includes several cells and a large number of mobile users, and therefore a combined approach where the microscopic and macroscopic aspects are modeled into one single simulator would lead to complex simulations with large time consumption. Thus, for obvious complexity and feasibility reasons, the combined approach is usually discarded in practice and another splitting approach is used instead. The splitting approach carries out the performance evaluation in two simulation phases: at *link level* and at *system level*, with suitable interfacing between the two levels [3]. This is illustrated in Figure 1-1.

A *link level simulator* typically includes a transmitter, a fading channel, and a receiver. It operates with a bit level granularity. The main concern here is to investigate the impact of the physical layer algorithms on the quality of the binary information transmitted through the fading channel between the transmitter and receiver. This is with the aim of accounting for the effectiveness of the physical layer algorithms and their robustness to channel impairments and multi-user interference. The transmission quality of the binary information is measured in terms of the average bit (BER) and frame (FER) error rates, which are usually calculated through Monte Carlo simulations spanning a large number of data frames experiencing independent fading realizations. Here at the link level, the performance evaluation of the physical layer algorithms is based on the traditional curves of average BER and FER versus the E_b/N_0 ratio, where E_b is the transmitted energy per information bit and N_0 is the noise power spectral density at the receiver side.

The *system level simulator* typically includes several base stations and all the mobiles that are connected to these base stations. The main interests here are to evaluate the whole system performance measured in terms of the cellular capacity and coverage and to develop proper *Radio Resource Management* (RRM) algorithms for appropriate sharing of the system

resources among the mobile users. The system level accounts for larger scale phenomena that cannot be accounted for with link level evaluation, such as the near far effect and the impact of the intra-cell and inter-cell interference in particular. The system level simulations are more or less complex depending on how accurate and how realistic the models represented are. Two approaches of system level simulations are generally used: the *static* and *dynamic* approaches [3]. The static approach requires lower computational costs and does not have time dependency, which prevents from rendering the effect of upper layers algorithms, which are beyond the scope of this thesis. It has been extensively used in the literature for preliminary system level studies as it can easily and efficiently provide meaningful statistical capacity and coverage estimates. The dynamic approach is a sophisticated time-based approach, which is more accurate and realistic than the static approach, but at the expense of much higher complexity. In the dynamic approach, time varying phenomena are represented, such as movements of mobiles, starting and ending of calls, fast fading, etc., which is well suited to account for mechanisms above the physical layer such as dynamic power control, time scheduling, channel allocation, etc. Typically, the dynamic system level simulations operate with a *Transmission Time Interval* (TTI) granularity, which usually includes one or multiple data frames.

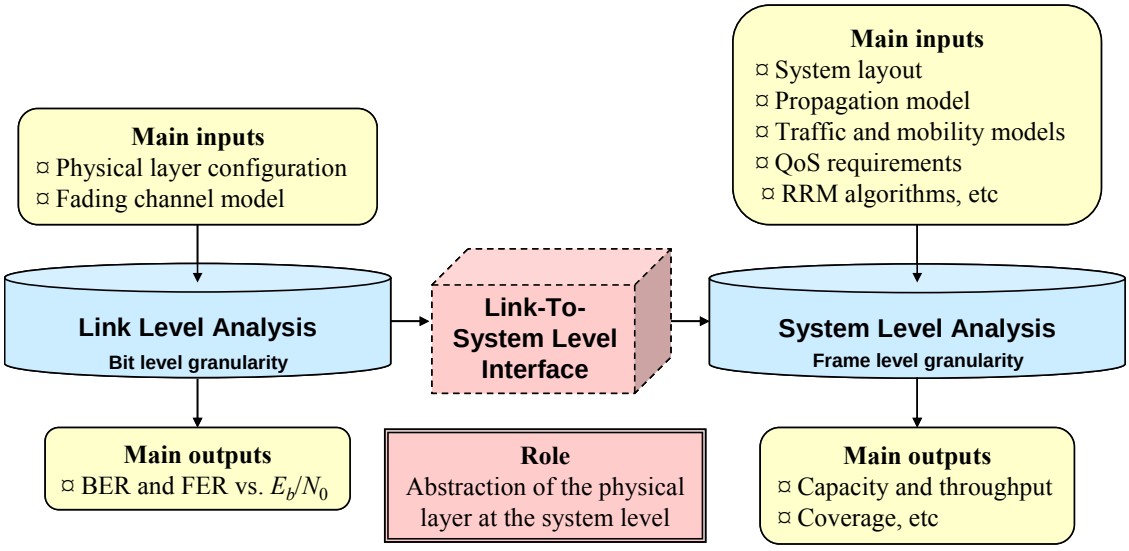

Figure 1-1: General approach for evaluating the performances of a cellular system.

Because of the separation between link and system levels, a suitable interface between the two levels is required. The target of the interface is to enable the system level simulator to predict easily and accurately the actual transmission quality of the different links in the system. Such prediction is required because the transmission quality cannot be measured

online within the system level simulations. Usual procedure to interface link and system levels is to use a set of *Look-Up Tables* (LUTs) mapping the BER and FER transmission quality measures to an adequate *Signal to Interference plus Noise Ratio* (SINR)-based measure that can easily be calculated at the system level. Different LUTs generally need to be produced for different operating conditions, and different levels of accuracy can be targeted depending on the particular study carried out at the system level. However, although such procedure has been adopted with more or less satisfaction in the context of single carrier systems, it at least needs to be revisited before transposing to the current multi-carrier context. More generally, it sounds honest and reasonable to reconsider from the beginning the problem of interfacing with the physical layer, when the physical layer under consideration is based on a technique that significantly differs from traditional single-carrier techniques.

This thesis addresses the two following issues in the context of MC-CDMA technology in the downlink of a multi-cellular environment:

- Provide an adequate link to system level interface which takes into account the specificity of MC-CDMA technology.
- Evaluate the cellular capacity for different MC-CDMA physical layer algorithms and configurations in order to identify their suitability for a given environment.

1.3 Scope and Objectives

The scope and main objectives of the thesis are described hereafter.

1.3.1 Link to System Level Interface

The first objective concerns the issue of link to system level interface. The goal here is to provide adequate abstraction of the MC-CDMA physical layer at the system level. The abstraction is carried out by defining an appropriate measure that allows to predict the link transmission quality at the system level. Two types of abstraction are investigated depending on whether the link transmission quality is defined in term of the short or long term error probability. The short term error probability refers to the probability of bit or frame error given a particular realization of the fast fading, whereas the long term error probability refers to the probability of bit or frame error averaged over a long time period during which a large number of independent fast fading realizations occur. The short term abstraction is said to be *frame oriented*, while the long term abstraction is said to be *multi-frame oriented*. The multi-frame oriented abstraction is appropriate for evaluating the cellular capacity through static

system level simulations, while the frame oriented abstraction is more appropriate within the scope of providing more accurate and realistic capacity results and for proper development of RRM algorithms through dynamic system level simulations.

1.3.2 Capacity Benefits of MC-CDMA Physical Layer Configurations

The second objective is to quantify the capacity benefits of the MC-CDMA physical layer algorithms and configurations in an urban macro-cellular environment. This is with the aim of identifying the most suitable algorithms and configurations for the given environment. The cellular capacity is evaluated through static system level simulations using the multi-frame oriented link to system level interface. The choice of static system level simulations using the multi-frame oriented interface is justified by their ability to provide meaningful results and by their much lower complexity compared to dynamic system level simulations.

1.4 Contents and Major Achievements

The rest of this thesis is composed of six chapters. The contents and major achievements are described below.

In Chapter 2, we describe the mobile radio channel with its large and small scale fading components. The large-scale fading includes path and shadowing losses, whereas small-scale fading represents the rapid distortions of the signal caused by multi-path propagation. In this chapter, we present the conventional statistical models and major characteristics for both fading components, and we also provide some simulation results that validate our approach for generating the small-scale fading. The models presented in this chapter are used in the thesis for analyzing and evaluating the performances at both link and system levels.

Chapter 3 presents an overview of OFDM multi-carrier modulation and CDMA code division multiple access technique. For OFDM modulation, we present its principle, its digital implementation using the IDFT and DFT operations, and its main advantages and drawbacks. We also develop its simplified time-frequency model in the most usual case when the inter symbol interference is completely absorbed by the guard interval and when the channel is invariant during the useful time period of an OFDM symbol. For CDMA technique, we describe its general concept, its main key strengths, and its two basic techniques, namely, DS-CDMA and FH-CDMA. At last, we briefly describe in this chapter the principles of four basic multi-carrier spread spectrum techniques, namely, MC-CDMA, MC-DS-CDMA, MT-CDMA,

and FLASH-OFDM. All these techniques have received wide interest in the literature for the broadband component of future 4G systems.

Next, in Chapter 4, we describe in details the conventional MC-CDMA physical layer with a single antenna in the downlink of a multi-cellular environment. This is the main concern of the thesis. The major modules that are of interest at the base station transmitter are described, namely, channel coding and interleaving, symbol mapping, spreading and multiplexing, chip mapping, and scrambling. The receiver structure is then presented and the received signal is calculated in the presence of intra-cell and inter-cell interference. The different detection techniques are presented: single user detection (MRC, EGC, ORC, and MMSEC) and multi-user detection (ML, ZF-MUD, MMSE-MUD, SIC, and PIC). In this chapter, we make the pragmatic choice of the single user detection for complexity reasons at the mobile terminal. The analytical expressions for the contributions of the desired signal, intra-cell interference, inter-cell interference, and thermal noise, are derived at the output of the MC-CDMA single user detector. These expressions are particularly used in the next chapter. This chapter defines the framework of the thesis and highlights the specificity of the MC-CDMA physical layer in the downlink of a multi-cellular environment.

Chapter 5 deals with the multi-frame oriented link to system interface. In this chapter, we first analyze the statistical characteristics of the received intra-cell and inter-cell interference. Besides analytical derivation of the intra-cell and inter-cell interference power factors, we propose an *Orthogonal Gaussian Noise* (OGN) to model the intra-cell multiple access signal at the transmitter and an *Additive White Gaussian Noise* (AWGN) to model the inter-cell interference at the receiver. Then, we perform theoretical analysis of the long term bit error probability with and without channel coding with the aim of extracting an appropriate link quality measure. From this theoretical analysis, the local mean SINR at the output of the detection module is identified as a potential measure that maps directly to the long term bit error probability. An accurate and low complexity link to system level interface simulator is then proposed using the OGN and AWGN interference models. The interface simulator provides the mappings between the local mean SINR and average BER and FER for a given MC-CDMA physical layer configuration and multi-path channel model. The SINR-FER mappings are used in the next chapter for evaluating the cellular capacity for different MC-CDMA physical layer configurations in an urban macro-cellular environment.

Chapter 6 focuses on the evaluation of the cellular capacity for different MC-CDMA physical layer configurations in an urban macro-cellular environment. In this chapter, we first

describe the system model and then present the methodology adopted for capacity evaluation at the system level. In addition to the capacity evaluation through Monte-Carlo system level simulations, we introduce a novel link level capacity indicator that enables analyzing the capacity behavior for a given physical layer configuration from the only knowledge of the outputs of the multi-frame oriented link to system interface, thus, without performing system level simulations. We then evaluate and compare the capacity results for different MC-CDMA physical layer configurations in the urban ETSI BRAN E macro-cellular environment by using both the link level capacity indicator and system level simulations. For performance evaluation, we put the emphasis on the trade-off between diversity and *Multiple Access Interference* (MAI), which is a major issue in the design of MC-CDMA systems.

In Chapter 7, we investigate the problem of frame oriented link to system interface for frame oriented convolutionally encoded transmissions over fading channels. The aim here is to determine adequate link quality measures for accurate prediction of the probability of frame error given a particular fading channel realization. In this chapter, we first state the problem and introduce the concept of effective SINR. Then, we describe some state of the art solutions and introduce novel solutions, namely, the *Generalized Chi-square Effective SINR* (GCES), *Refined Generalized Exponential Effective SINR* (RGEES), and *Refined Generalized Chi-square Effective SINR* (RGCES). The performances of all presented solutions are evaluated and compared in the context of MC-CDMA using both QPSK and 16QAM modulations with UMTS convolutional code.

Finally, we conclude the thesis with a summary of the achieved results and present some perspectives for future research.

1.5 References

[1] IST European project 4MORE, "4G MC-CDMA multiple antenna system On chip for Radio Enhancements," *website: www.ist-4more.org*.

[2] IST European project MATRICE, "MC-CDMA Transmission Techniques for Integrated Broadband Cellular Systems," *website: www.ist-matrice.org*.

[3] H. Holma, "A Study of UMTS Terrestrial Radio Access Performance," *Ph.D. thesis, Helsinki University of Technology*, Oct. 2003.

[4] K. Fazel, S. Kaiser, "Multi-Carrier and Spread Spectrum Systems," *John Wiley & Sons Ltd.*, 2003.

[5] IST European project I-METRA, "Performance Evaluation," *Deliverable D4, website: www.ist-imetra.org,* Sep. 2003.

[6] IST European project FITNESS, "System-Level Simulation Methodology Defined," *Deliverable 4.1*, Oct. 2002.

[7] T. S. Rappaport, "Wireless Communications: Principles and Practice," *Second edition, Prentice Hall,* 2002.

[8] Third Generation Partnership Project (3GPP) for Wideband CDMA standards, *website: www.3gpp.org*.

[9] Wireless World Research Forum (WWRF), *website: www.wireless-world-research.org*.

[10] J. Zander, S. Kim, "Radio Resource Management for Wireless Networks," *Artech House Publishers*, 2001.

Chapter 2

The Mobile Radio Channel

This chapter presents an overview of the conventional stochastic model commonly used for describing the mobile radio channel. This model is decomposed into two fading components: the large-scale fading which regroups the path loss and shadowing, and the small-scale fading which reflects the most rapid distortions caused by multi-path propagation. In this chapter, we present the analytical models for both fading components and perform simulations in order to validate our simulation approach for generating the small-scale fading.

2.1 Physical Propagation Mechanisms

In mobile radio communications, the signal path from a base station antenna to a mobile receiver antenna or vice-versa is referred to as the *mobile radio channel*. A radio signal transmitted through a mobile radio channel undergoes all the mechanisms that govern the propagation of electromagnetic waves. Three basic mechanisms influence the propagation of electromagnetic waves, namely, *reflection*, *diffraction*, and *scattering* [1].

Two kinds of reflection are generally considered [2]: *specular reflection* and *diffuse reflection*. Specular reflection occurs when a propagating wave strikes a smooth surface of large dimensions compared to the wavelength. In specular reflection, the energy is reflected in one direction only as illustrated in Figure 2-1. If the surface has considerable roughness, however, the reflected energy spreads in all directions instead of one specular direction. This is called diffuse reflection and it is more complicated to model than specular reflection.

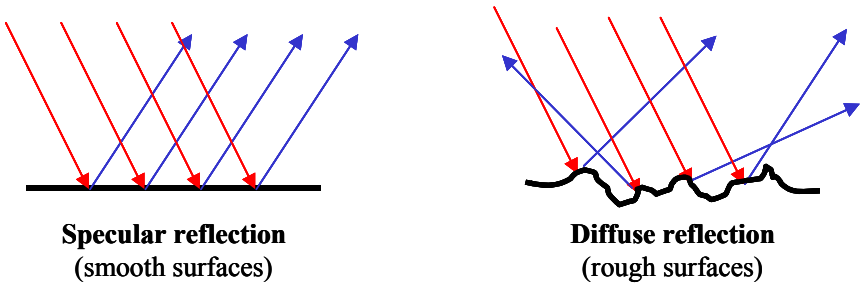

Figure 2-1: Specular and diffuse reflections.

In the considered carrier frequency range around 5 GHz, corresponding to wavelengths around 6 cm, reflections from building walls are neither purely specular nor radically diffuse. The same holds for the ground reflections where the surface roughness is usually greater but

the angle of incidence is nearly 90°. Diffuse reflections occur within building walls when the angle of incidence is small and from the ground when it is very rough [2].

Diffraction takes place when a propagating wave encounters an edge of a large obstacle, causing part of the wave to bend into shaded areas behind the edge [1]. This phenomenon is more important at lower frequencies, but not negligible at 5 GHz.

Scattering generally refers to the interaction between the radio wave and small obstacles of irregular shapes [1]. Here, small means that the obstacle has dimensions on the order or smaller than the wavelength. These objects scatter the wave energy into all directions, in such a way that it is extremely difficult to determine the energy scattered in each direction. Examples of such objects are raindrops, snowflakes, leaves, lamp-posts, etc. The effects of scattering are difficult to determine and, thus, are usually accounted for statistically.

The propagation mechanisms described above lead to three different effects that influence the signal received after propagation through the radio channel. The first effect is called *path loss*. It describes a deterministic average attenuation of the signal strength depending only on the distance between the transmitter and receiver. The path loss plays an important role on large time scales like seconds or minutes, since the distance between the transmitter and receiver in most situations does not change significantly on smaller time scales.

The second effect is called *shadowing*. It reflects the changes in the propagation paths due to movements of the mobile, or possibly of the obstacles in the channel as well. Shadowing is not deterministic. It varies on the same time scale as the path loss and causes fluctuations of the received signal strength at locations with the same distance to the transmitter. These fluctuations follow a log normal distribution centered around the path loss value.

The third effect is called *multi-path fading*. It is a result of the multiple propagation paths created by reflection, diffraction, and scattering mechanisms. The received signal is the superposition of a large number of replicas of the transmitted signal arriving from different directions with random delays, phases, and amplitudes. The superposition of these randomly phase-shifted waves may be constructive or destructive causing fluctuations in the received signal amplitude and phase. Multi-path propagation is also of stochastic nature and yields the most rapid fluctuations within smaller time scales such as milliseconds or even microseconds depending on the mobility.

All three effects combined give the overall attenuation of the radio channel experienced by the received signal. The overall attenuation can be decomposed as follows [3]:

$$a(t) = a_{PL}(t)a_{SH}(t)a_{MF}(t) \tag{2.1}$$

where the subscripts are self explicit. Thus, by taking into account the attenuation factor $a(t)$ which summarizes the effects of the radio channel, the input-output relationship between the transmitted signal $s(t)$ and received signal $r(t)$ can then simply be written as

$$r(t) = a(t)s(t) \tag{2.2}$$

In the sequel, we distinguish two groups of fading depending on the time scale over which the received signal power fluctuates. The first group is called the *large-scale fading* and regroups the attenuations due to path loss and shadowing. The second group is called the *small-scale fading* and reflects the rapid fluctuations caused by multi-path propagation.

2.2 Large-Scale Fading

The large-scale fading also known as *slow fading* regroups the effects of path loss and shadowing. The fluctuations of the received signal power due to these effects vary on a large time scale typically of several hundreds of milliseconds.

2.2.1 Path Loss

The path loss expresses the loss in power that a transmitted signal experiences due to the distance separation between the transmitter and receiver. It is a function of several system design parameters like the carrier frequency, antenna gains and heights, etc. The path loss PL is usually expressed as the difference in dB between the transmitted power P_t and received power P_r [3]:

$$PL[dB] = P_t[dBW] - P_r[dBW] \tag{2.3}$$

The path loss is constant in time for a specific non-changing environment, distance and carrier frequency. Thus, it is deterministic.

The path loss models are always considered for a receiver location beyond the *Fraunhofer region*, which is the region beyond the far-field distance of the transmitter antenna. These models use a so-called *close-in distance* d_0, which serves as a known power reference point [1]. Hence, the path loss at distance d is usually expressed as

$$PL(d)[dB] = PL(d_0)[dB] + P_r(d_0)[dBW] - P_r(d)[dBW] \tag{2.4}$$

The reference path loss $PL(d_0)$ is calculated through field measurements at distance d_0. Typical values of the reference distance d_0 are 1 m in indoor environments and 100 m or more in outdoor environments for systems operating at few GHz frequencies [1].

In wave propagation theory, the strength of a propagating wave decreases with respect to distance, due in particular to the conservation of the radiated energy flux. Thus, the loss in power increases with respect to the distance between the transmitter and receiver. The path loss increase with respect to distance is usually described by using an exponent μ as

$$PL(d)[dB] = PL(d_0)[dB] + 10\mu \log_{10}\left(\frac{d}{d_0}\right) \tag{2.5}$$

The value of μ is specific to the environment under consideration and to whether there is a *line of sight* (LOS) component, i.e. a direct path, between transmitter and receiver antennas or not. Table 2-1 provides figures of the values of μ for some typical environments [1].

Environment	**Exponent μ**
Free space	2
Two-Ray ground reflection model	4
Urban (LOS)	2.7 to 3.5
Urban (NLOS)	3 to 5

Table 2-1: Path loss exponent for different environments.

2.2.2 Shadowing

The path loss model presented previously performs a deterministic calculation of the power loss for a given distance between the transmitter and receiver. However, measurements done under several conditions have shown stochastic variations of the average received signal power for a given fixed distance. The received signal power is therefore not deterministic, but varies due to the objects in and around the radio channel. These stochastic variations are referred to as *shadowing* and were denoted by $a_{SH}(t)$ in (2.1). Note that these variations are constant in time, as long as the mobile and its complete environment do not move, and in case of motions, they take several hundreds of milliseconds at least to significantly change depending on the mobility and on the environment [1][3].

From measurements of the received signal power for a variety of environments and distances, the variations of the logarithm of the measured signal power relative to the average power predicted by path loss were shown to follow a normal distribution with 0 mean in dB. This implies a log-normal distribution of the received power around the mean value

corresponding to the path loss. The theoretical basis to the log-normal distribution is that the different propagation paths in the radio channel suffer from several successive random reflections and diffractions. Expressed in dB, the loss in each propagation path corresponds to adding or subtracting a random loss from the path loss average value. As the different propagation paths are independent, the sum of all the dB losses for a large number of paths converges to a normally distributed random variable. This is justified by the central limit theorem. In the linear scale, that becomes a log-normal distribution.

The shadowing variations can therefore be calculated from the normal distribution

$$p_{SH}(x) = \frac{1}{\sqrt{2\pi\sigma_{SH}^2}} \exp\left(-\frac{x^2}{2\sigma_{SH}^2}\right) \tag{2.6}$$

The standard deviation σ_{SH} usually takes values between 5 dB and 12 dB, depending on the communication system used and the geographical context of the propagation environment. For cellular communication systems, a value of 8 dB is typically used [1][3].

By combining the effects of path loss and shadowing, the overall resulting attenuation also known as the *Local Mean (LM*) attenuation can therefore be written as

$$LM[dB] = PL[dB] + SH[dB] \tag{2.7}$$

Thus, by substituting (2.5) in (2.7), *LM* expressed in the linear scale takes the form

$$LM = \frac{P_t}{P_r} = PL(d_0)\left(\frac{d}{d_0}\right)^{\mu} 10^{\frac{SH[dB]}{10}} = C_0 d^{\mu} 10^{\frac{SH[dB]}{10}} \tag{2.8}$$

where C_0 is a constant determined from measurements at the reference distance d_0, μ is the path loss exponent, and *SH* is the log-normal shadowing variable.

The model given in (2.8) is referred in the literature as the *local mean propagation model* and it is commonly used to provide the average received signal power for random locations in mobile radio communication systems [1].

2.3 Small-Scale Fading

The small-scale fading also referred to as *fast fading* reflects the rapid fluctuations of the received signal strength and phase. These fluctuations are caused by multi-path propagation and are experienced on a small time scale of a few milliseconds or shorter depending on the carrier frequency and mobility.

2.3.1 Multi-path Channel Model

The physical basis of multi-path propagation is given by the reception of multiple copies of the transmitted signal, each having traveled along a different propagation path. In a typical environment, each propagation path has a different length and, thus, the signal copy having traveled along this path arrives at the receiver with a different delay. Signal copies traveling along short paths will arrive earlier, while other copies traveling along longer paths will arrive later. The channel is said to have a *memory* since it "stores" the signal copies for a certain time period, i.e., the duration of the propagation.

Beside the different delays, the signal copies are attenuated differently, since along their different propagation paths they traverse different obstacles of different shapes and sizes. Moreover, the signal copies arrive at the receiver from different directions and with different phases. The superposition of all these differently delayed, attenuated, and phase-shifted signal copies at the receiver results in an interference pattern, which alternately behaves constructively and destructively. If nothing moves within the propagation environment, the received signal will remain constant, and therefore the channel is said to be *time invariant*. In contrast, if any kind of change is encountered in the propagation environment, all or some paths will change in time and, thus, the interference pattern will change in time. As a consequence the channel becomes *time variant*.

The multi-path channel model is a mathematical model that is meant to account for all the effects of multi-path propagation. Let us first consider the transmission of a bandpass signal $s(t)$ at carrier frequency f_c in the case of a time invariant channel. By associating to each path p a different length l_p and a different attenuation a_p, the received bandpass signal $r(t)$ being the superposition of all copies can be written as

$$r(t) = \sum_p a_p s\left(t - \frac{l_p}{c}\right) \tag{2.9}$$

Considering the complex envelope representations, $s_e(t)$ and $r_e(t)$ of the bandpass signals $s(t)$ and $r(t)$ respectively, the input-output relationship given in (2.9) becomes

$$r_e(t) = \sum_p a_p \, \mathrm{e}^{-j\varphi_p} \, s_e(t - \tau_p) \tag{2.10}$$

where $\varphi_p = 2\pi f_c l_p / c$ and $\tau_p = l_p / c$ denote respectively the phase shift of the carrier frequency and the delay caused by the different length of path p, and c is the speed of light.

Thus, in a static environment, a multi-path propagation leads to the interference of multiple copies with different attenuations $\{a_p\}$, different phase shifts $\{\varphi_p\}$, and different delays $\{\tau_p\}$. The time invariant channel model can then be modeled as a *linear time invariant causal filter* with baseband impulse response

$$h_e(\tau) = \sum_p a_p \, \mathrm{e}^{-j\varphi_p} \, \delta(\tau - \tau_p) \tag{2.11}$$

where δ(.) denotes Dirac's delta function.

Now let us consider the effect of motion in the channel. Let α_p denote the angle of arrival of path p with respect to the direction of motion of the receiver, as shown in Figure 2-2.

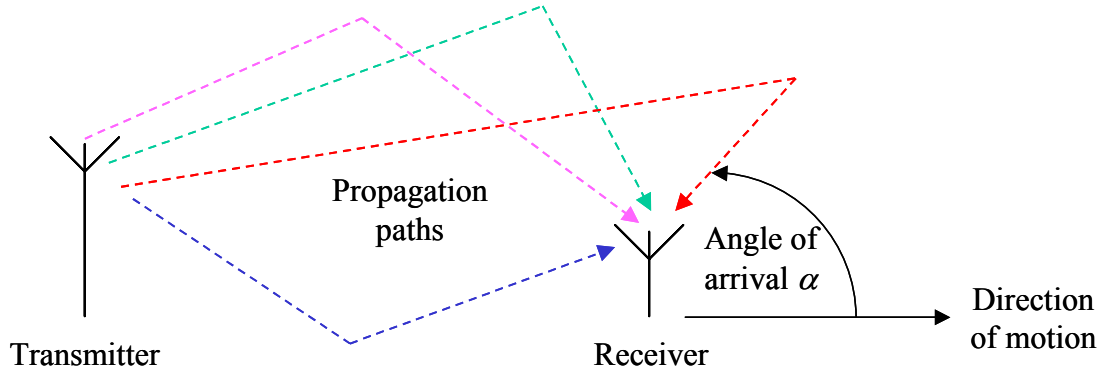

Figure 2-2: Sketch of signal arrival in a multi-path environment.

The path length is now time variant and it relates to the mobile speed v as [3]

$$l_p(t) = l_p(0) - v\cos(\alpha_p)t \tag{2.12}$$

From (2.12), we obtain a different function for the complex envelope of the received signal, which now depends on time t, as given below

$$r_e(t) = \sum_p a_p \, \mathrm{e}^{-j\varphi_p} \mathrm{e}^{j2\pi\frac{v}{c}\cos(\alpha_p)t} \, s_e\left(t - \tau_p + \frac{v}{c}\cos(\alpha_p)t\right) \tag{2.13}$$

Equation (2.13) can be simplified by making the three following operations. First, we regroup into the complex A_p the attenuation a_p and the term of phase φ_p. Secondly, we neglect the extra delay caused by $l_p(t)$ compared to the delay τ_p caused by the path length $l_p(0)$. At last, we introduce the *Doppler frequency* $f_d = f_c v/c$ and the *Doppler shift* $\nu_p = \cos(\alpha_p) f_d$. With this, we obtain the simplified form

$$r_e(t) = \sum_p A_p \, e^{j2\pi\nu_p t} \, s_e(t - \tau_p) \tag{2.14}$$

Thus, from (2.14), we can observe that motion introduces a frequency offset $\{\nu_p\}$ of the carrier in addition to the signal changes that are already present in static conditions.

As for the time invariant channel, the time variant channel is modeled by a *linear time variant causal filter* with impulse response

$$h_e(t,\tau) = \sum_p A_p \, e^{j2\pi\nu_p t} \delta(\tau - \tau_p) \tag{2.15}$$

The received signal can therefore be expressed as the convolution of the transmitted signal with the impulse response $h_e(t,\tau)$ with respect to the time delay τ:

$$r_e(t) = \int_0^{+\infty} h_e(t,\tau) s_e(t-\tau) d\tau = h_e(t,\tau) \otimes s_e(t) \tag{2.16}$$

Equivalently to the time domain response $h_e(t,\tau)$, the channel can also be characterized in the frequency domain by the *time variant transfer function* $H(t,f)$, which is the Fourier transform of $h_e(t,\tau)$ with respect to τ. It is obtained from (2.15) as

$$H(t,f) = \sum_p A_p \, e^{j2\pi(\nu_p t - f\tau_p)} \tag{2.17}$$

In the frequency domain, the spectra of transmitted and received signals are related by simple multiplication with the transfer function $H(t,f)$:

$$R(t,f) = H(t,f) S(f) \tag{2.18}$$

Thus, the transfer function $H(t,f)$ determines the attenuation experienced at time t by the spectrum component $S(f)$ at frequency f.

For a large number of paths in the propagation environment and in the absence of a LOS component, the central limit theorem applies to the time variant transfer function $H(t,f)$ and justifies its Gaussian distribution in both time and frequency. By using polar coordinates, the amplitude ρ of $H(t,f)$ thus follows a Rayleigh distribution while its phase θ follows a uniform distribution in $[0,2\pi[$ [4]. In the presence of a LOS component, however, a Rice distribution is more generally assumed for the amplitude ρ of $H(t,f)$. On the other hand, for a small number of paths, the assumption of Gaussian random process as a result of the central limit theorem is

no more appropriate. In this case, ρ is generally assumed to follow a Nakagami distribution either in the presence or absence of a LOS component [4].

The Rayleigh distribution shows up in most non-LOS scenarios, which are encountered mostly in indoor and macro-cellular urban environments. In these scenarios, the performance of communication systems are worse than in scenarios where Rice distribution applies. This is because Rice fading is less destructive than Rayleigh fading. In this thesis, Rayleigh fading is assumed since our focus is on macro-cellular urban environments.

2.3.2 Characterization in Time and Frequency

As shown in (2.17), the Doppler shifts $\{\nu_p\}$ and time delays $\{\tau_p\}$ are responsible of the time and frequency variations of the attenuation experienced by the received signal. Although Doppler shifts are frequency offsets of the carrier frequency that may induce *Inter-Carrier Interference* (ICI) in multi-carrier systems, their overall impact on the received signal is interpreted as a time selective behavior. For the time delays it is the opposite. While the delays are time offsets of the transmitted signal that may induce *Inter-Symbol Interference* (ISI), their impact on the received signal is interpreted as a frequency selective behavior.

Two quantities are commonly used in practice to describe the impact of time delays and Doppler shifts on the received signal. They are the *delay spread* $\Delta\tau$ and *Doppler spread* $\Delta\nu$. The delay spread relates to the frequency selectivity of the channel, whereas the Doppler spread relates to the time selectivity of the channel.

2.3.2.1 Delay Spread and Frequency Selectivity

The delay spread describes the time spread of the signal caused by multi-path propagation with several paths of different lengths and, thus, of different delays. Since the delays $\{\tau_p\}$ are different for different paths, the transfer function $H(t,f)$ will then vary with respect to frequency f and the spectrum $S(f)$ will undergo different attenuations for different frequency components. This phenomenon is referred to as *frequency selectivity*.

The severity of the frequency selectivity is measured by the product of the delay spread $\Delta\tau$ with the bandwidth W of the signal. So, if the delay spread is small compared to the inverse of W, that is the symbol time T_s, which corresponds to values of $W\Delta\tau$ smaller than 1, the transfer function $H(t,f)$ is nearly constant within the bandwidth W and all frequency components of the spectrum $S(f)$ will then have almost the same attenuation. In this case the channel is said to be *flat* or *frequency non selective*. On the other hand, if the delay spread is significant compared

to the symbol time, which corresponds to values of $W\Delta\tau$ greater than 1, the transfer function varies within the bandwidth W and the frequency components of the signal will be differently attenuated. Here, the channel is said to be *frequency selective* and the receiver suffers in the time domain from ISI.

A detailed picture of the frequency selectivity of the multi-path channel is given by the *spaced frequency correlation function* of $H(t,f)$. This function gives us the correlation between the transfer function at different frequencies and it is given by [4]

$$\Phi_H(\Delta f) = \frac{1}{2} E\left\{H(t,f)H^*(t,f-\Delta f)\right\} \tag{2.19}$$

Substituting of (2.17) in (2.19) yields

$$\Phi_H(\Delta f) = \frac{1}{2} E\left\{\sum_p \sum_q A_p A_q^* \, \mathrm{e}^{j2\pi(\nu_p-\nu_q)t} \mathrm{e}^{-j2\pi f(\tau_p-\tau_q)} \mathrm{e}^{-j2\pi\Delta f\tau_q}\right\} \tag{2.20}$$

If scatterers at different delays $\{\tau_p\}$ are uncorrelated, the autocorrelation function depends only on the frequency spacing Δf. This assumption is called the *Uncorrelated Scattering* (US) assumption of multi-path channels. It can be written as

$$\frac{1}{2} E\left\{A_p A_q^* \, \mathrm{e}^{j2\pi(\nu_p-\nu_q)t}\right\} = \sigma_p^2 \, \delta_{pq} \tag{2.21}$$

The variance σ_p^2 is the average power of the p-th signal copy. From (2.21), the spaced frequency correlation function in (2.20) turns into

$$\Phi_H(\Delta f) = \sum_p \sigma_p^2 \, \mathrm{e}^{-j2\pi\Delta f\tau_p} \tag{2.22}$$

In the time delay domain, the inverse Fourier transform of $\Phi_H(\Delta f)$ is called the *power delay profile* of the channel and gives the average power of the multi-path components as a function of time delays. It is given by [4]

$$P(\tau) = \int_{-\infty}^{+\infty} \Phi_H(\Delta f) \mathrm{e}^{j2\pi\Delta f\tau} \, d\Delta f = \sum_p \sigma_p^2 \, \delta(\tau-\tau_p) \tag{2.23}$$

The maximum delay τ_{max} or the standard deviation σ_τ of the power delay profile are often used to measure the delay spread $\Delta\tau$ [4][5]. The standard deviation σ_τ is obtained as

$$\sigma_\tau^2 = \frac{1}{\Phi_H(0)} \int_0^\infty (\tau - \tau_m)^2 P(\tau) d\tau \tag{2.24}$$

where τ_m denotes the mean of the power delay profile.

From the autocorrelation function $\Phi_H(\Delta f)$, a measure called the *coherence bandwidth* is derived in order to estimate the frequency spacing for which the channel transfer function does not change significantly. The mathematical definition of the coherence bandwidth is somewhat subjective and it mainly depends on the form of the power delay profile. In general, the coherence bandwidth is related to the delay spread by

$$B_{coh} = \frac{1}{2\pi\sigma_\tau} \tag{2.25}$$

Figure 2-3 depicts the normalized power delay profile and frequency autocorrelation function for the ETSI BRAN E channel model (cf. Appendix A.1). The normalization is done such that $\Phi_H(0) = 1$. The delay spread of this channel is found equal to 247.3 ns, which by applying (2.25) results in a coherence bandwidth of almost 0.64 MHz. This channel model will be mostly used within this thesis as it is well suited for cellular environments.

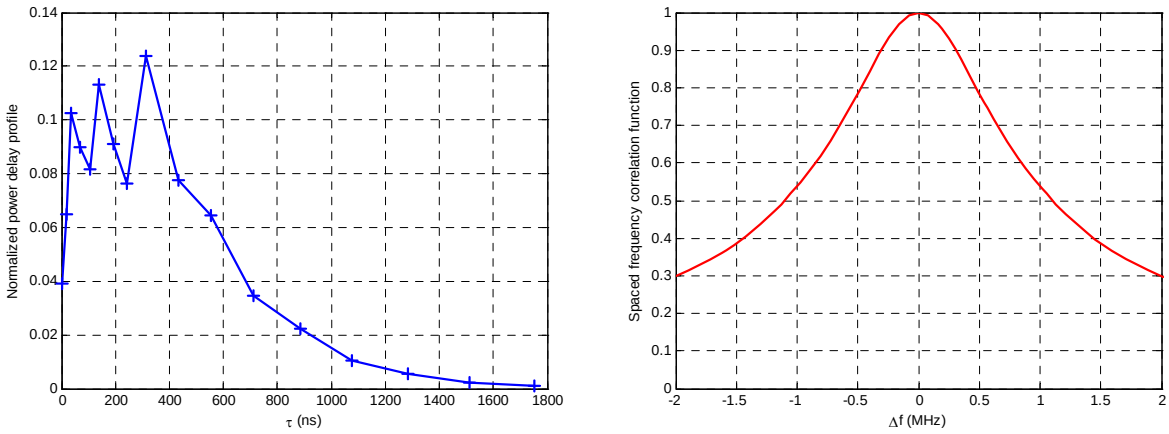

Figure 2-3: Power delay profile (left) and frequency correlation (right) for the ETSI BRAN E channel model.

2.3.2.2 Doppler Spread and Time Selectivity

The Doppler spread is the dual of the delay spread. It describes the shift in frequency of the signal spectrum caused by the motion of the objects within the propagation environment. The different Doppler shifts $\{\nu_p\}$ of the different paths make the transfer function $H(t,f)$ vary in

time (see (2.17)). The attenuation experienced by the signal spectrum $S(f)$ at frequency f is therefore time variant and this phenomenon is referred to as *time selectivity*.

The severity of the time selectivity is measured by the product of the Doppler frequency f_d with the time span the receiver needs to process the incoming signal. If coherent detection is assumed, where each data symbol is processed independently, the processing time is the symbol length T_s. So, if the Doppler frequency f_d is much lower than the processing rate $1/T_s$, the transfer function $H(t,f)$ stays almost constant within the symbol time T_s, and the channel is said to be *slow* or *time non selective*. In contrast, if the Doppler frequency is larger than the processing rate, then the transfer function varies within the processing time, and the channel is called to be *fast* or *time selective*.

By analogy to the spaced frequency correlation function $\Phi_H(\Delta f)$ for frequency selectivity, the *spaced time correlation function* $\Gamma_H(\Delta t)$ reflects the time selectivity. It measures the correlation between $H(t,f)$ at different time instants and is defined as [4]

$$\Gamma_H(\Delta t) = \frac{1}{2} E\left\{H(t,f) H^*(t-\Delta t, f)\right\} \tag{2.26}$$

The fact that the autocorrelation function $\Gamma_H(\Delta t)$ only depends on time difference Δt results from the assumption that the transfer function $H(t,f)$ is a *Wide Sense Stationary* (WSS) process. Under this assumption, the scatterers at different Doppler shifts $\{\nu_p\}$ are uncorrelated.

From the time autocorrelation function $\Gamma_H(\Delta t)$, the so-called *Doppler power spectrum* is derived by Fourier transform, which yields

$$S_H(\nu) = \int_{-\infty}^{+\infty} \Gamma_H(\Delta t) \mathrm{e}^{-j2\pi\nu\Delta t}\, d\Delta t \tag{2.27}$$

As for the coherence bandwidth, a measure called the *coherence time* is determined here from the time autocorrelation function in order to indicate the time span during which the transfer function $H(t,f)$ roughly stays constant. Again the definition of the coherence time is somewhat subjective and depends on the form of the Doppler power spectrum. Defined for an autocorrelation value of 0.5, the coherence time is related to the Doppler spread by [4]

$$T_{coh} \approx \frac{1}{2 f_d} \tag{2.28}$$

A commonly used model for the time correlation is the so-called *Clarke's model* [6]. This model assumes an isotropic scattering, which means that an isotropic antenna is used at the receiver and that the angles of arrival $\{\alpha_p\}$ are uniformly distributed in $[0,2\pi[$. Thus, under these assumptions, the time autocorrelation function takes the form [6]

$$\Gamma_H(\Delta t) = \mathrm{J}_0(2\pi f_d \Delta t) \tag{2.29}$$

where $\mathrm{J}_0(.)$ refers to the *zero-order Bessel function of the first kind*. The function $\Gamma_H(\Delta t)$ in (2.29) is normalized such that $\Gamma_H(0) = 1$. Taking the Fourier transform of (2.29) yields the so-called *Jakes Doppler power spectrum*, which is given by [7]

$$J(\nu) = \frac{1}{\pi f_d \sqrt{1-\left(\frac{\nu}{f_d}\right)^2}} \quad \forall\, \nu \in \left]-f_d, f_d\right[\tag{2.30}$$

Figure 2-4 illustrates the Bessel function and Jakes spectrum for a maximum Doppler frequency f_d of 100 Hz. At carrier frequency of 5 GHz, this corresponds to a mobile speed v of 6 m/s or 21.6 km/h. Thus, the coherence time according to (2.28) is equal to 5 ms, which is also verified by the Bessel function in Figure 2-4.

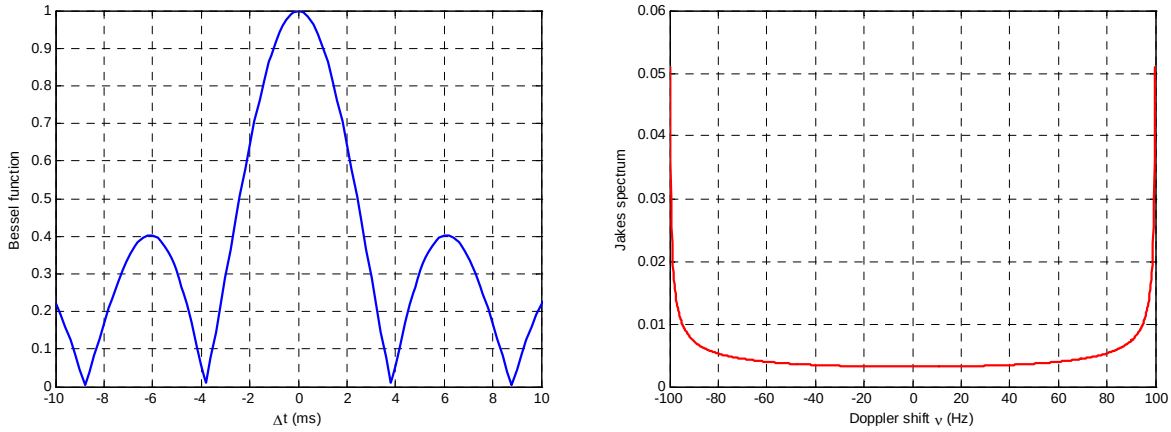

Figure 2-4: Bessel function (left) and Jakes spectrum (right) for 100 Hz Doppler frequency.

2.3.3 Level Crossing Rate and Fading Duration

Given a certain attenuation threshold X, it is of great interest for system design to know the average rate with which the amplitude ρ of the transfer function $H(t,f)$ will cross this threshold. This rate is called the *Level Crossing Rate* (LCR) [1]. In addition, it is also of interest to know the average duration the amplitude ρ will stay below the threshold X. This is

called the *Average Fading Duration* (AFD). The LCR and AFD are also two important measures for checking the validity of time variant Rayleigh channel simulations.

The LCR determines how many times per second the Rayleigh fading envelope ρ crosses the specified threshold X in an upward direction. It is given by [1][3]

$$LCR(X) = \sqrt{2\pi} f_d \frac{X}{\sqrt{2\sigma^2}} e^{-\frac{X^2}{2\sigma^2}} \tag{2.31}$$

where $\sigma^2 = \Phi_H(0)$ is the sum of all the average powers of all multi-path components. The maximum LCR occurs at threshold $X_0 = \sigma$, i.e., at the root mean square level of the Rayleigh fading envelope.

The AFD determines in average how long the Rayleigh fading envelope ρ stays below the threshold X. It is related to the level crossing rate by [1][3]

$$AFD(X) = \frac{1 - e^{-\frac{X^2}{2\sigma^2}}}{LCR(X)} \tag{2.32}$$

The AFD is useful to determine the most likely number of bits that may be lost during a fade. It decreases as the Doppler frequency f_d decreases or equivalently as the mobile speed v increases.

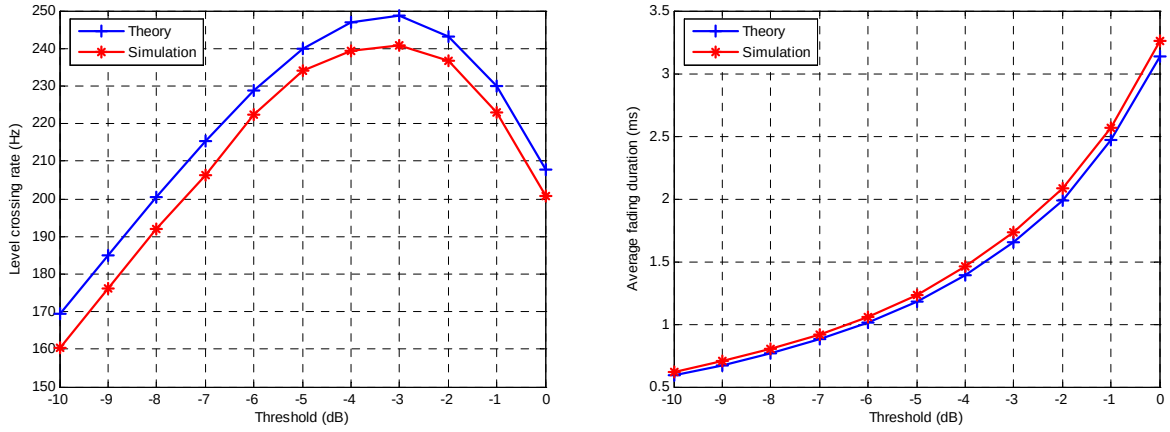

Figure 2-5: Level crossing rate (left) and average fading duration (right) for the ETSI BRAN E channel model.

Figure 2-5 illustrates the LCR and AFD versus the threshold X in dB for the ETSI BRAN E channel. The mobile speed v is 13.89 m/s, which yields a Doppler frequency f_d of 231.5 Hz at 5 GHz carrier frequency. The Doppler effect is simulated following Appendix A.2. Figure

2-5 shows a good agreement between the values obtained from simulation and those obtained from the formulas given in (2.31) and (2.32). The slight difference between simulation and theory is due to sampling and to the limited observation interval of the fading envelope considered in simulation. The sampling rate is considered equal to $50f_d \approx 11.57$ KHz and the observation interval has 5000 samples, which correspond to a time period of $100/f_d \approx 432$ ms.

Figure 2-6 depicts the time-variant Rayleigh channel envelope in dB and its autocorrelation function for the ETSI BRAN E channel model. From Figure 2-6, on the left, we can observe that at 3 dB of the Rayleigh envelope, the fading is correlated within a time span of roughly 2 ms. On the right, the time span for an autocorrelation value of 0.5 appears to be nearly equal to 2.2 ms. This matches well the value of 2.16 ms obtained from the coherence time formula given in (2.28). This good agreement shows once more the validity of our approach for simulating time-variant Rayleigh multi-path channels.

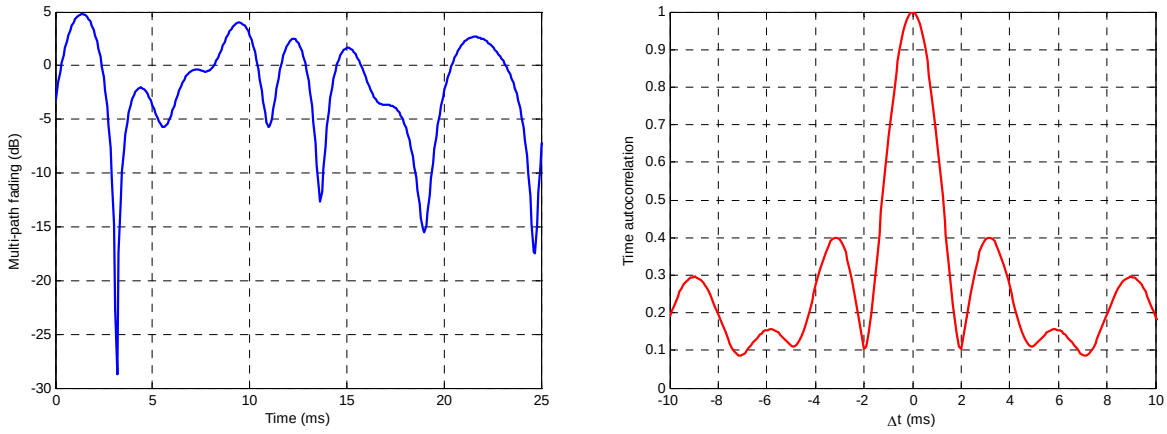

Figure 2-6: Rayleigh envelope in dB (left) and its time autocorrelation (right) for the ETSI BRAN E channel model.

2.4 Conclusions

This chapter presented the conventional model of the mobile radio channel. This model is analytically decomposed into three components. The first component referred to as the path loss is deterministic and is function of the distance between the transmitter and receiver. It expresses the average loss of the received signal power for a given fixed distance between the transmitter and receiver. The second component called as shadowing is of stochastic nature. It reflects the fluctuations observed around the received signal power predicted by path loss and caused by slow variations in the propagation environment. The path loss and shadowing are regrouped into the so-called large-scale fading as their effects occur on a large time scale of

several hundreds of milliseconds. The last component known as multi-path fading is also of stochastic nature. It describes the rapid fluctuations of the signal strength and phase. These fluctuations are caused by changes in the multi-path environment. They are experienced on a small time scale, mostly of few milliseconds or shorter.

The models of all the three components of the mobile radio channel presented in this chapter will be used all along this thesis in order to evaluate the performance of MC-CDMA systems in the downlink of an urban macro-cellular environment.

2.5 References

[1] T. S. Rappaport, "Wireless Communications: Principles and Practice," *Second edition, Prentice Hall,* 2002.

[2] H. Laitinen, "Verification of a stochastic radio channel model using wideband measurement data," *Master thesis, Helsinki University of Technology,* June 1999.

[3] A. Aguiar, J. Gross, "Wireless Channel Models," *Technical Report TKN-03-007, Telecommunication Networks Group, Technical University Berlin,* Apr. 2003.

[4] J. G. Proakis, "Digital Communications," *Mc-Graw Hill,* 1995.

[5] J. K. Cavers, "Mobile Channel Characteristics," *Kluwer Academic Publishers,* 2000.

[6] R. H. Clarke, "A Statistical Theory of Mobile-Radio Reception," *Bell Systems Technical Journal,* vol. 47, pp. 957-1000, 1968.

[7] W. C. Jakes, "Microwave Mobile Communications," *IEEE Press, New Jersey,* 1994.

[8] P. A. Bello, "Characterization of Randomly Time-Variant Linear Channels," *IEEE Transactions on Communications Systems,* vol. 11, pp. 360-393, Dec. 1963.

[9] B. H. Fleury, P. E. Leuthold, "Radiowave Propagation in Mobile Communications: An Overview of European Research," *IEEE Communications Magazine,* Feb. 1996.

[10] P. Guguen, G. El Zein, "Les techniques multi-antennes pour les réseaux sans fil," *Hermes science publications,* 2004.

Chapter 3
Overview of OFDM and CDMA Systems

This chapter presents an overview of OFDM multi-carrier modulation and CDMA multiple access technique. It also briefly discusses the general concepts of the four basic multi-carrier CDMA techniques, namely, MC-CDMA, MC-DS-CDMA, MT-CDMA, and FLASH-OFDM.

3.1 Orthogonal Frequency Division Multiplex (OFDM)

Orthogonal Frequency Division Multiplex (OFDM) [1] is an efficient multi-carrier modulation that is robust to multi-path radio channel impairments. It has been used in various high data-rate wireless multimedia communication standards like the European standards for *Digital Audio Broadcasting* (DAB) [2] and *Terrestrial Digital Video Broadcasting* (DVB-T) [3], the *Wireless Local Area Network* (WLAN) standards such as IEEE802.11a [4] and HIPERLAN/2 [5], and the *Wireless Local Loop* (WLL) standards such as IEEE802.16a [6] and HIPERMAN [7]. Nowadays, OFDM is widely accepted for potential use in future high data-rate broadband wireless communication systems [8][9].

3.1.1 Principle

OFDM multi-carrier modulation aims at transmitting data at high rates while avoiding the *Inter-Symbol Interference* (ISI) caused by multi-path propagation.

To achieve this, OFDM modulation divides the initial serial high-rate data stream of short symbol time T_d into N_c parallel sub-streams of lower rate and, thus, of longer symbol time T_s. The longer symbol time T_s compared to the maximum delay $\tau_{\max}$ of the multi-path channel significantly decreases the ISI. Each parallel sub-stream is modulated on one specific sub-carrier, and adjacent sub-carriers are chosen with the minimum frequency spacing $\Delta f = 1/T_s$ that is necessary to achieve orthogonality between the corresponding signals, presuming a rectangular pulse shaping. The N_c sub-carrier frequencies are given by

$$f_n = n\Delta f = \frac{n}{T_s} \quad ; \quad n = 0 \ldots N_c - 1 \tag{3.1}$$

In order to cancel out the ISI and preserve orthogonality between the sub-carriers, a guard interval of duration $T_g \geq \tau_{\max}$ is inserted in front of the OFDM symbol [1]. This results in an overall OFDM symbol duration $T_s' = T_s + T_g$.

Denoting by $\{s_n[i]\}$ the set of N_c complex-valued data symbols transmitted on the N_c sub-carriers within the i-th OFDM symbol, the complex envelope of the OFDM signal with rectangular pulse shaping can then be written as

$$s(t)=\sum_{i=-\infty}^{+\infty}\sum_{n=0}^{N_c-1}s_n[i]\frac{1}{\sqrt{T_s}}\mathrm{rect}_{T_s'}\left(t-iT_s'\right)\mathrm{e}^{j2\pi\frac{n}{T_s}\left(t-iT_s'-T_g\right)} \tag{3.2}$$

The power density spectrum of the OFDM signal is then obtained as

$$S(f)=\frac{1}{T_s}\sum_{n=0}^{N_c-1}\left|\frac{\sin\left(\pi\left(f-f_n\right)T_s'\right)}{\pi\left(f-f_n\right)}\right|^2 \tag{3.3}$$

Figure 3-1 depicts the normalized power density spectrum for N_c = 64 sub-carriers and T_g = T_s/4 versus the normalized frequency fT_d. In Figure 3-1, the spectra of the first and last sub-carriers are also depicted, and the whole spectrum is shifted to the center frequency.

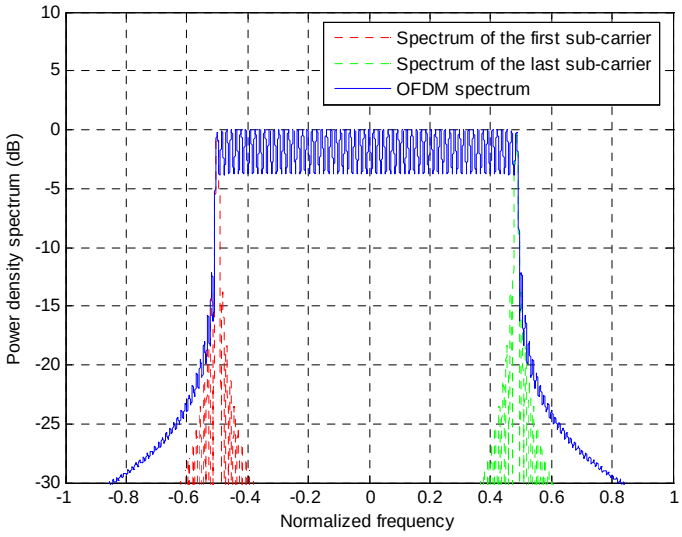

Figure 3-1: OFDM normalized spectrum for N_c = 64 sub-carriers and T_g = T_s/4.

As shown in Figure 3-1, the power density spectrum of the OFDM signal is localized within the normalized frequency range of $-0.5 \le fT_d \le 0.5$. Moreover, sub-carriers that are near the band edges contribute most to the outside lobes. Thus, for a large number of sub-carriers, the power density spectrum of OFDM multi-carrier modulation approaches that of single-carrier modulation with ideal Nyquist filtering. The bandwidth of the OFDM signal confined to the main lobes is found as

$$B_{OFDM} = (N_c - 1)\frac{1}{T_s} + \frac{2}{T_s'} \approx \frac{N_c}{T_s} = \frac{1}{T_d} \tag{3.4}$$

In multi-path propagation, the received signal $r(t)$ is obtained through the convolution of the transmitted signal $s(t)$ with the multi-path channel impulse response $h(t,\tau)$ and addition of the AWGN signal $\nu(t)$:

$$r(t) = \int_0^{\tau_{\max}} s(t-\tau)h(t,\tau)d\tau + \nu(t) \tag{3.5}$$

The i-th received data symbol on the n-th sub-carrier is determined as

$$r_n[i] = \frac{1}{\sqrt{T_s}} \int_{iT_s'+T_g}^{(i+1)T_s'} r(t)\mathrm{e}^{-j2\pi\frac{n}{T_s}\left(t-iT_s'-T_g\right)} dt \tag{3.6}$$

By assuming that the guard interval duration T_g is greater than the maximum delay $\tau_{\max}$ of the multi-path channel so that the guard interval completely absorbs the ISI, and that the channel response $h(t,\tau)$ is time invariant during the ISI-free time interval $[iT_s'+T_g,(i+1)T_s'[$, the received symbol $r_n[i]$ in (3.6) reduces then to

$$r_n[i] = h_n[i]s_n[i] + \nu_n[i] \tag{3.7}$$

where $h_n[i]$ stands for the channel frequency response at the n-th sub-carrier frequency f_n during the time interval $[iT_s'+T_g,(i+1)T_s'[$, and $\nu_n[i]$ represents the AWGN contribution.

Thus, from (3.7), OFDM multi-carrier transmission can simply be viewed as a discrete time and frequency transmission with N_c parallel Gaussian channels of different complex-valued attenuations $\{h_n[i]\}$. This simplified model is illustrated in Figure 3-2.

3.1.2 Implementation Using DFT Operation

A major advantage of OFDM is that it can be implemented in the discrete domain by using the *Discrete Fourier Transform* (DFT) operation. This was first found by Weinstein & al. in 1971 [10]. When sampling the complex envelope $s(t)$ in (3.2) at rate $1/T_d$, the following samples are obtained

$$s\left(iT_s' + kT_d\right) = \frac{1}{\sqrt{T_s}} \sum_{n=0}^{N_c-1} s_n[i]\mathrm{e}^{j2\pi\frac{n}{N_c}\left(k-N_g\right)} \quad ; \quad k = 0 \ldots N_c + N_g - 1 \tag{3.8}$$

where $N_g = T_g/T_d$ stands for the number of samples within the guard interval. The N_c+N_g samples in (3.8) can simply be obtained by performing the IDFT operation over the set of data symbols $\{s_n[i]\}$. Indeed, the IDFT provides the N_c samples

$$x_m[i] = \sum_{n=0}^{N_c-1} s_n[i] e^{j2\pi \frac{nm}{N_c}} \quad ; \quad m = 0 \ldots N_c - 1 \tag{3.9}$$

Except for the constant term, the N_c samples $\{s(iT_s'+kT_d)$ for $k = N_g, \ldots, N_g+N_c-1\}$ in (3.8) are exactly the same as the samples $\{x_m[i]\}$ in (3.9). Furthermore, the first N_g remaining samples $\{s(iT_s'+kT_d)$ for $k = 0, \ldots, N_g-1\}$ corresponding to the guard interval are the same as the N_g tail samples $\{x_m[i]$ for $m = N_c-N_g, \ldots, N_c-1\}$. That is why the guard interval is referred to as the *cyclic prefix*. Thus, in order to get the N_c+N_g samples of an OFDM symbol, the transmitter needs first to perform the IDFT operation over the set of data symbols $\{s_n[i]\}$ and then to insert the cyclic prefix guard interval. The N_c+N_g resulting samples are then passed through a digital-to-analog converter providing the transmitted signal $s(t)$

$$s(t) = \sum_{i=-\infty}^{+\infty} \sum_{k=0}^{N_c+N_g-1} s(iT_s' + kT_d) \mathrm{rect}_{T_d}(t - iT_s' - kT_d) \tag{3.10}$$

Here, we consider a rectangular pulse shaping for the sake of simplicity. The analog signal $s(t)$ is then transposed to the carrier frequency f_c and sent through the radio channel.

At the receiver side, after down conversion to baseband, the received signal $r(t)$ in (3.5) is sampled at the same rate $1/T_d$, which results in the N_c+N_g received samples

$$r(iT_s' + kT_d) = \int_0^{\tau_{\max}} s(iT_s' + kT_d - \tau) h(iT_s' + kT_d, \tau) d\tau + \nu(iT_s' + kT_d) \tag{3.11}$$

The first N_g samples $\{r(iT_s'+kT_d)$ for $k = 0, \ldots, N_g-1\}$ are removed since they contain the ISI. By assuming that the channel impulse response $h(t,\tau)$ is time invariant over the N_c ISI-free samples $\{r(iT_s'+kT_d)$ for $k = N_g, \ldots, N_g+N_c-1\}$, these samples can then be written as

$$r(iT_s' + kT_d) = \frac{T_d}{\sqrt{T_s}} \sum_{n=0}^{N_c-1} h_n[i] s_n[i] e^{j2\pi \frac{n}{N_c}(k-N_g)} + \nu(iT_s' + kT_d) \tag{3.12}$$

The received symbols on the N_c sub-carriers are then determined by performing the DFT operation over the N_c ISI-free samples in (3.12) as

$$r_n[i] = \frac{1}{\sqrt{T_s}} \sum_{k=N_g}^{N_g+N_c-1} r\left(iT_s' + kT_d\right) e^{j2\pi \frac{n}{N_c}(k-N_g)} = h_n[i]s_n[i] + v_n[i] \tag{3.13}$$

Note that (3.7) and (3.13) are exactly the same. They express the simplified discrete time-frequency model of OFDM multi-carrier transmission illustrated in Figure 3-2 below.

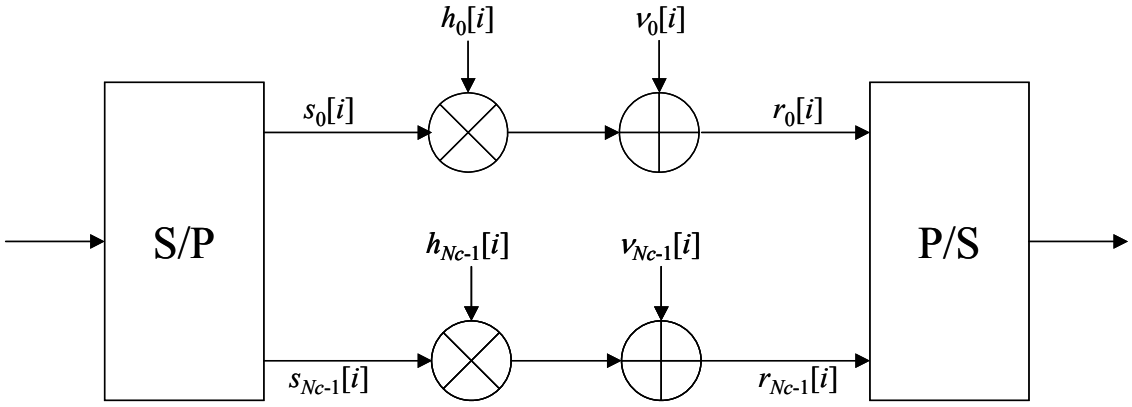

Figure 3-2: Simplified model for OFDM multi-carrier transmission.

3.1.3 Advantages and Drawbacks

The advantages and drawbacks of OFDM modulation are summed up hereafter [11]:

Advantages

- High spectral efficiency thanks to the overlapping spectra of the orthogonal sub-carriers and the nearly rectangular OFDM spectrum for high numbers of sub-carriers.
- Simple implementation using the IDFT and DFT operations respectively at the transmitter and receiver sides.
- Low-complexity channel equalization in the frequency domain thanks to the mitigation of ISI and ICI.
- Flexibility in the sub-carrier management, e.g., water filling, thanks to the independent parallel transmissions over the sub-carriers.

Disadvantages

- High *Peak-to-Average Power Ratio* (PAPR) for high numbers of sub-carriers, which increases the complexity of the analog-to-digital and digital-to-analog converters and reduces the efficiency of the RF power amplifier.

- Sensitivity to the loss of orthogonality between sub-carriers due to Doppler shifts, frequency errors, or non-linear amplification.
- Sensitivity to the time and frequency synchronization errors and to the phase noise caused by the imperfections of the transmitter and receiver oscillators.

3.2 Code Division Multiple Access (CDMA)

The development of an appropriate multiple access protocol to serve several users simultaneously is a major challenge in wireless communications. *Code Division Multiple Access* (CDMA) is an efficient multiple access protocol that was first used in the popular 2G IS-95 cellular system also known as *cdmaOne*. CDMA has then gained much more popularity after being adopted in 3G cellular systems, namely in W-CDMA system also known as UMTS [8] and cdma2000 system [12]. The success of CDMA in 3G cellular systems has given incitement to develop CDMA-based systems for potential use in future beyond 3G cellular systems [8][9][14][15].

3.2.1 General Concept

In wireless communications, multiple users share a common communication channel. In order to avoid conflicts between simultaneously transmitting users, there must be some rules on how to allocate the common channel to the different users. These rules constitute the *multiple access protocol*.

The multiple access protocols are generally classified into three groups: *contentionless protocols*, *contention protocols*, and *CDMA protocols* [16]. The contentionless protocols avoid the simultaneous access to the channel by separating the transmissions of the different users in time and/or frequency. With the contention protocols however, there is no scheduling of the users' transmissions. This means that a user getting ready to transmit does not have exact knowledge of at which time and on which frequency it can transmit without interfering with the other users. Even if the user may know of any ongoing transmissions by sensing the channel, it still has no exact knowledge about other ready users. This makes the occurrence of a successful transmission a more or less random process and, thus, the contention protocols also referred to as *random access* protocols should resolve the contention that occurs when several users transmit simultaneously.

The CDMA protocols do not solve the multiple access problem by a division of the transmissions of different users in either time or frequency, but instead make a division by

assigning each user a different "signature wave form" or "code". Codes are chosen with small cross-correlations in order to keep the *Multiple Access Interference* (MAI) low and, thus, enable the receivers to extract their desired signals even in the presence of interfering signals. As long as the MAI is not too large, the desired signal can be extracted without error. Thus, in this case, the protocol behaves as a contentionless protocol. However, if the number of simultaneously transmitting users rises above a certain limit, the MAI becomes too large for the desired signal to be extracted correctly and contention occurs, thus making the system interference limited. The CDMA protocols are therefore basically contentionless unless too many users access the channel at the same time. This is why the CDMA protocols are rightly placed between the contentionless and contention protocols [16].

The CDMA protocols are also known as *Spread Spectrum Multiple Access* (SSMA) protocols. This is because in these protocols the information signal power is spread over a much wider bandwidth than that required to transmit the information signal. This spreading is achieved by encoding the information signal with the code signal, which is independent of the information signal and has a much larger spectral width than the information signal. The ratio of code signal bandwidth B_c to information signal bandwidth B_i is called the *processing gain* P_G of the spread spectrum system [16]:

$$P_G = \frac{B_c}{B_i} \tag{3.14}$$

The higher the processing gain is, the lower the power spectral density one needs to transmit the information with and, thus, the more noise-like the transmitted signal appears. The receiver, knowing the code signal, correlates the received signal with a synchronously generated replica of the code signal in order to recover the original information signal.

3.2.2 Key Strengths

There are number of properties that are behind the development of CDMA for both military and civilian applications. Some of these properties are briefly discussed below.

- **Multiple access capability:** Thanks to the low cross-correlations between the users' codes, the receivers will be able to distinguish between the users even if their signals overlap in both time and frequency. After correlating the received signal with the user-specific code, the interfering signals will still be spread over the large bandwidth, while the desired signal will be despread. Thus, within the information bandwidth, the power of

the desired signal will be much larger than the interfering power provided there are not too many interferers, and the desired signal can therefore be extracted without error.

- **Inherent frequency diversity:** Thanks to the broad bandwidth of the spread spectrum signal compared to the coherence bandwidth of the multi-path channel, independent fading will affect different parts of the broad bandwidth, each part having approximately the width of the channel coherence bandwidth. Thus, unlike narrowband transmissions, broadband transmissions benefit from an inherent frequency diversity that significantly reduces the risk of destructive flat fading over the whole transmission bandwidth.
- **Interference rejection and anti-jamming capability:** Since cross-correlating the code signal with a narrowband signal will spread the power of the narrowband signal over the broad transmission bandwidth, the power of the narrowband signal will then be highly reduced within the information bandwidth. This provides CDMA with an anti-jamming capability, where jamming refers to the particular case when the narrowband interferer is voluntarily disturbing the system.
- **Low probability of interception:** Because of its low power spectral density and noise-like codes, the spread spectrum signal is difficult to detect and intercept by a third party. It is this property together with the previous one that make spread spectrum techniques attractive for military applications [16].
- **Universal frequency reuse:** In multi-cellular systems, the interference from neighboring cells called *inter-cell interference* significantly degrades the quality of transmissions. In *Time* (TDMA) and *Frequency* (FDMA) *Division Multiple Access* systems, the inter-cell interference is mitigated by dividing the total available spectrum into a number of frequency bands that are allocated and reallocated properly to the different cells in the system. Such division of the total spectrum lowers the overall system spectral efficiency and adds complexity to frequency planning and system deployment. In CDMA systems, however, since the multiple access is done in the code domain, all cells can use the total spectrum at the same time and, thus, a universal frequency reuse is possible. This highly increases the spectral efficiency and considerably simplifies frequency planning and system deployment. This is this property that gives incitement to the development of CDMA for mobile radio communication systems [17].

3.2.3 Basic Techniques

CDMA techniques are classified into two groups: *averaging techniques* and *avoidance techniques* [16]. The averaging techniques cope with the MAI by averaging it over a wide time interval, whereas the avoidance techniques cope with the MAI by avoiding it for a large part of the time. The typical averaging and avoidance techniques are respectively *Direct Sequence* (DS-CDMA) and *Frequency Hopping* (FH-CDMA). The general concepts of these techniques are briefly described in the following.

3.2.3.1 Direct Sequence (DS) - CDMA

The principle of DS-CDMA is to spread the information signal by multiplying it directly with a code signal that has the form

$$c^{(k)}(t) = \sum_{\ell=0}^{L-1} c_\ell^{(k)} \operatorname{rect}_{T_c}\left(t - \ell T_c\right) \tag{3.15}$$

where $c_\ell^{(k)}$ is the ℓ-th chip of the spreading code assigned to user k, T_c is the chip duration, and L is the length of the spreading code also called here the *spreading factor*.

DS-CDMA is an averaging multiple access technique since it allows all users to access simultaneously the whole spectrum. The major advantages of DS-CDMA are the easiness of the spreading process since it is done by a simple multiplication, and the possibility to apply coherent demodulation at the receiver. However, its main disadvantages are its restrictive synchronization since it has to be carried out within a fraction of the chip duration and its sensitivity to the *near-far effect* [16]. The near-far effect refers to the high interference level inflicted by the transmissions of users that are close to the base station on the transmissions of users that are far away from the base station.

3.2.3.2 Frequency Hopping (FH) - CDMA

In FH-CDMA, instead of spreading the information signal over the whole available bandwidth, the bandwidth of the information signal is unchanged but the carrier frequency is changed periodically after each time period T_h, which is called the *hop time* [16]. The carrier frequency is pseudo-randomly chosen in the set of available frequencies according to the user-specific *Pseudo-Noise* (PN) code. It is the function of the PN code to ensure that all frequencies in the total available bandwidth are optimally used. The PN code specific to user k has the form

$$c^{(k)}(t) = \sum_{\ell=0}^{L-1} \exp\left(j2\pi f_\ell^{(k)} t\right) \mathrm{rect}_{T_h}\left(t - \ell T_h\right) \tag{3.16}$$

where $f_\ell^{(k)}$ denotes the ℓ-th frequency selected by the PN code assigned to user k, and L is the number of frequencies available in the total bandwidth.

Two kinds of frequency hopping are identified depending on whether the hopping rate is greater or smaller than the data rate. When the hopping rate is greater than the data rate, the frequency hopping is said to be *fast* as there are many frequency hops per transmitted data symbol, whereas otherwise, the frequency hopping is said to be *slow* as many data symbols are transmitted per frequency hop [16].

Compared to DS-CDMA, FH-CDMA has the main advantages of being much easier to synchronize and less sensitive to the near-far effect. Indeed, in FH-CDMA, synchronization has to take place within a fraction of the hop time, which is much longer than the chip time of a DS-CDMA system. Besides, because FH-CDMA is an avoidance multiple access technique, the probability of users close to the base station transmitting simultaneously in the same frequency band than users far away from the base station is small. This makes FH-CDMA much less sensitive to the near-far effect than DS-CDMA. Despite these advantages, FH-CDMA has the disadvantages of being very difficult to implement since it requires a highly sophisticated frequency synthesizer at both sides and since coherent demodulation is difficult to apply at the receiver side because of the problems of maintaining the phase relationships during hopping [16].

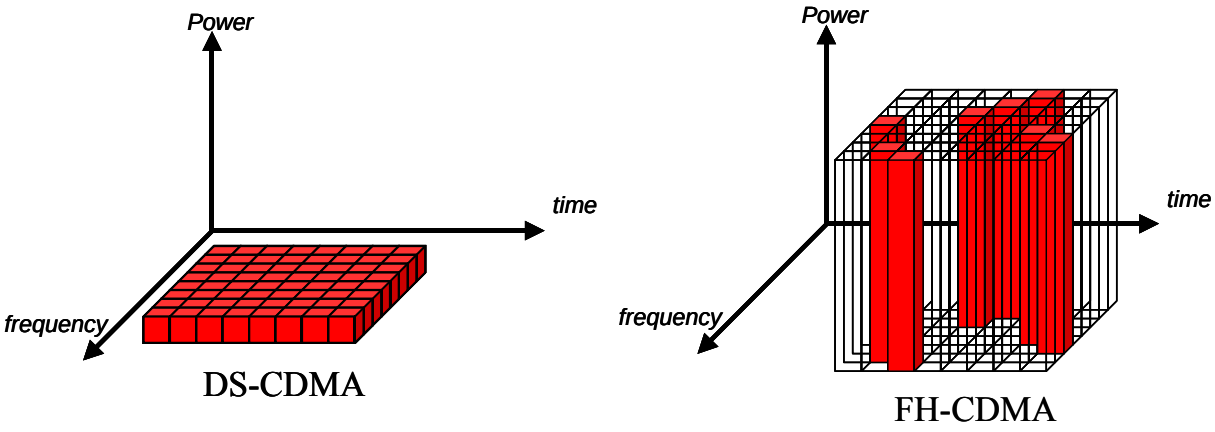

Figure 3-3: Time-frequency-power usage for DS-CDMA and FH-CDMA signals.

Figure 3-3 compares the time-frequency occupancy and transmission power of DS-CDMA and FH-CDMA signals. As shown in Figure 3-3, the DS-CDMA signal occupies the total

bandwidth during all time periods and, thus, it spreads the signal power over the total bandwidth. However, the FH-CDMA signal occupies one part of the total bandwidth during each time period. Thus, the power of the FH-CDMA signal in this band part is much higher than that of the DS-CDMA signal. However, on average, the same power density spectrum is obtained and, thus, both systems transmit the same average power in the total bandwidth.

3.3 Multi-Carrier CDMA Techniques

The combination of multi-carrier modulation with CDMA appeared for the first time in 1993. Three combinations were mainly proposed, namely, MC-CDMA proposed by Yee & al. [18], Fazel [19], and Chouly & al. [20], MC-DS-CDMA proposed by DaSilva & al. [21], and multi-tone (MT-) CDMA proposed by Vandendorpe [22]. All these three combinations are averaging CDMA techniques in the sense that the signals of the different users occupy the total bandwidth simultaneously. Few years later, a multi-carrier avoidance CDMA technique called FLASH-OFDM was also proposed and developed by Flarion [23]. FLASH-OFDM uses OFDM with fast frequency hopping for the wireless multiple access protocol. The main motivation for applying multi-carrier modulation in all these techniques is to enable high-rate data transmissions while mitigating the ISI caused by multi-path propagation. The general concepts of all these basic multi-carrier CDMA techniques are presented hereafter.

3.3.1 MC-CDMA

Originally, the principle of MC-CDMA was to perform *spreading in the frequency domain* [18][19][20]. Here, each data symbol of a user is multiplied by the chips of the user-specific spreading code, and the resulting chips are then transmitted on different sub-carriers within the same OFDM symbol. More recently, spreading in MC-CDMA has been extended to cover both the time and frequency domains. In two-dimensional (2D) spreading, each chip of a data symbol is transmitted by one specific sub-carrier within one specific OFDM symbol [24][25]. An example of MC-CDMA 2D time-frequency domain spreading is illustrated in Figure 3-4.

MC-CDMA inherits the advantages and drawbacks of OFDM and CDMA. The high spectral efficiency and low-complexity receiver of OFDM combined to the flexibility and multiple access capability of CDMA make the MC-CDMA technique a suitable candidate for the downlink air interfaces of future radio communication systems [13][14][26]. The MC-CDMA air interface in the downlink of a cellular system is described in details in Chapter 4.

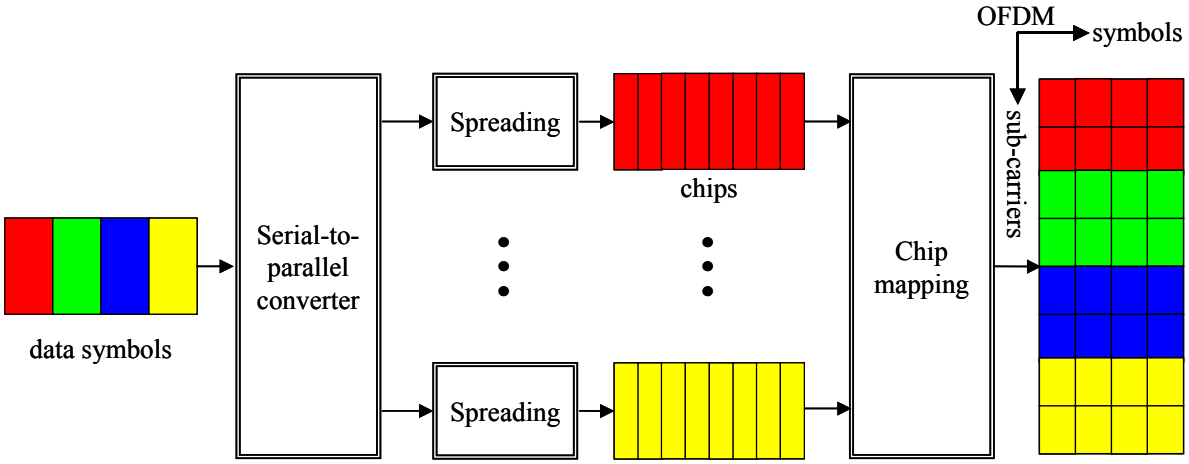

Figure 3-4: Example of MC-CDMA 2D time-frequency domain spreading.

3.3.2 MC-DS-CDMA

MC-DS-CDMA was first proposed for simplifying the difficult synchronization in high-rate single carrier DS-CDMA [21]. The principle of MC-DS-CDMA is to create multiple parallel DS-CDMA streams of long chip duration and, thus, of moderate bandwidth. Thus, similarly to DS-CDMA, MC-DS-CDMA performs *spreading along the time domain* on each individual stream. The parallel streams are transmitted on orthogonal sub-carriers, where orthogonality is achieved after spreading in order to avoid the ICI. The spacing between adjacent sub-carrier frequencies has the general form [26]

$$\Delta f = \frac{(1+\alpha)}{T_c} \tag{3.17}$$

where α is the roll-off factor of the Nyquist filter, $0 \le \alpha \le 1$, and T_c is the chip duration. Typically, a square-root Nyquist filter of $\alpha > 0$ is considered for the chip form, which results in spectrally non-overlapping sub-carriers [26].

In MC-DS-CDMA, for a given transmission bandwidth, small numbers of sub-carriers can generally be considered since the sub-carriers are disjoint and individually spread. This results in a lower PAPR than in MC-CDMA for the same transmission bandwidth because of the smaller number of sub-carriers. The low PAPR property and the capability to handle asynchronous transmissions make MC-DS-CDMA suitable for the asynchronous uplink of mobile radio communication systems [26]. The principle of MC-DS-CDMA time domain spreading is illustrated in Figure 3-5.

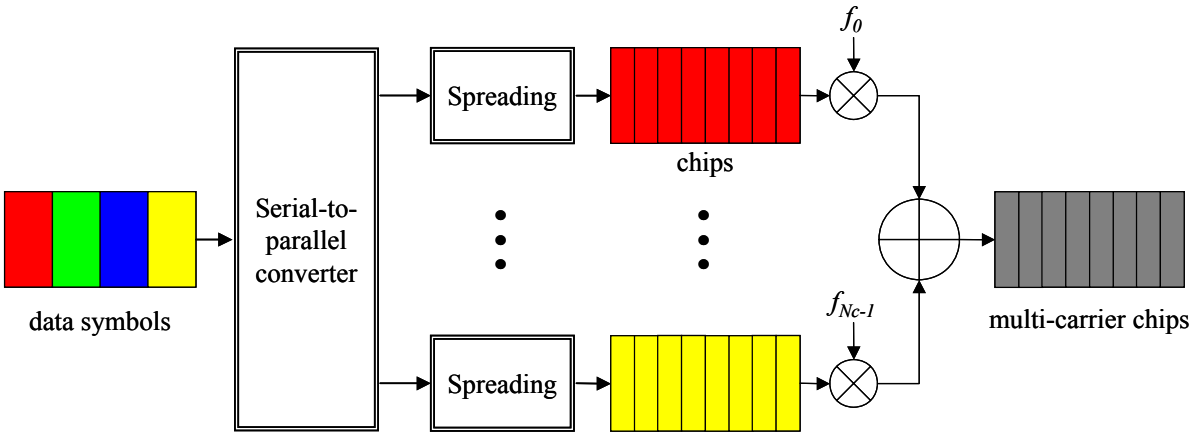

Figure 3-5: Principle of MC-DS-CDMA time domain spreading.

3.3.3 MT- CDMA

The MT-CDMA system aims at combating the effects of multi-path propagation thanks to the longer symbol duration of multi-carrier modulation and the capability of DS-CDMA to reduce the multi-path interference [22][27]. MT-CDMA follows the same spreading approach as in MC-DS-CDMA so that *spreading is done along the time domain* (cf. Figure 3-5). Compared to MC-DS-CDMA, the difference is that MT-CDMA chooses the sub-carriers orthogonal on the symbol duration T of the parallel streams with the minimum frequency spacing $1/T = 1/LT_c$, where L is the length of the spreading code. As each sub-carrier occupies a bandwidth close to $1/T_c$, the spectra of the different sub-carriers are therefore strongly overlapping, which introduces ISI and ICI in multi-path propagation [27]. The ISI and ICI effects have severe impact on the system performance, and high-complexity receivers are required to cancel them out. On the other hand, the tight sub-carrier spacing allows the use of more sub-carriers than in MC-DS-CDMA, which helps reduce the MAI and, thus, allows to accommodate more users in the system [27][28].

3.3.4 FLASH-OFDM

FLASH-OFDM is an avoidance multi-carrier CDMA technique that was proposed and developed by Flarion [23]. It uses a fast frequency hopping with a hop time T_h equal to the OFDM symbol time T_s. Thus, as illustrated in Figure 3-6, each data symbol of a user is transmitted here within one OFDM symbol and on one specific OFDM sub-carrier, the latter being determined by the user-specific PN code.

The PN codes of the users within the same cell are chosen orthogonal so that the users do not interfere. Thus, unlike averaging CDMA techniques, FLASH-OFDM benefits from zero intra-cell interference. In a cellular deployment, FLASH-OFDM also benefits from the CDMA advantage of universal frequency reuse since all base stations use the entire available bandwidth [23]. The inter-cell interference in FLASH-OFDM has an impulsive nature, i.e., it occurs on the symbol level and, thus, once the interference is present the data symbol is lost. However, in averaging multi-carrier CDMA systems, the inter-cell interference has an average nature, i.e., the interference occurs on the chip level and, thus, if some chips are interfered, the data symbol may still be recovered from other non interfered chips.

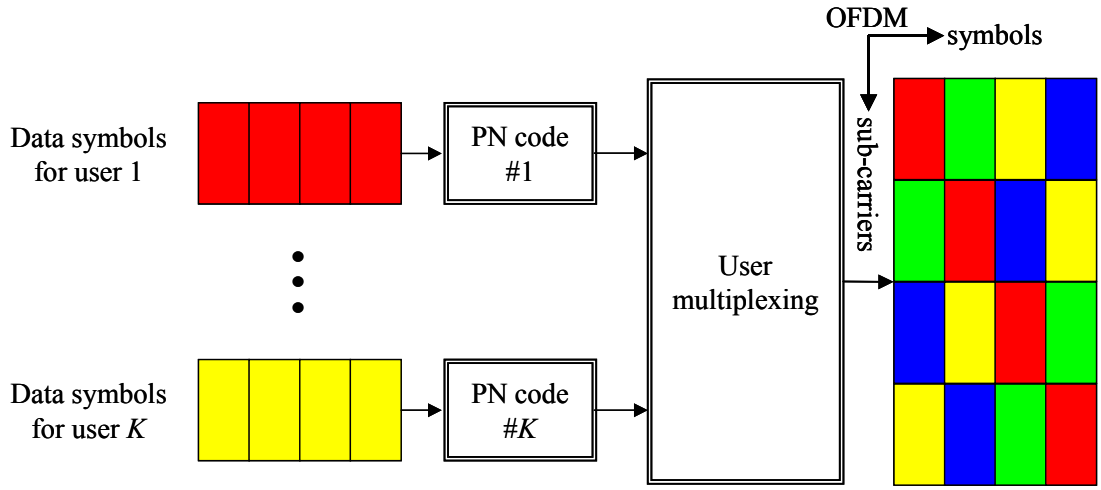

Figure 3-6: Principle of FLASH-OFDM technique.

3.4 Conclusions

In this chapter, we presented the principles and major characteristics of OFDM multi-carrier modulation and CDMA multiple access technique. In addition to its relatively low-complexity receivers, OFDM allows high-rate data transmissions without ISI and neither ICI. On the other hand, CDMA is an efficient and flexible multiple access technique that allows a universal frequency reuse in a cellular system.

This chapter also introduced the general concepts of the four basic multi-carrier CDMA techniques, namely, MC-CDMA, MC-DS-CDMA, MT-CDMA, and FLASH-OFDM. While MC-CDMA, MC-DS-CDMA, and MT-CDMA are averaging CDMA techniques, FLASH-OFDM on the other hand is an avoidance technique that uses fast frequency hopping for the multiple access. The use of MC-CDMA technique for the downlink air interfaces of future radio communication systems is the main concern of this thesis. The MC-CDMA technique

will be detailed in the next chapter in the downlink of a multi-cellular environment, which is the context of interest in this thesis.

3.5 References

[1] M. Alard, R. Lassalle, "Principles of modulation and channel coding for digital broadcasting for mobile receivers," *EBU Review*, no. 224, Aug. 1987.

[2] ETSI, "Radio Broadcasting systems; Digital Audio Broadcasting (DAB) to mobile, portable, and fixed receivers," *ETS 300-401, second edition*, May 1997.

[3] ETSI, "Digital video broadcasting (DVB); Framing structure, channel coding, and modulation for digital terrestrial television," *EN 300-744 V1.1.2*, Aug. 1997.

[4] IEEE Std. 802.11a-1999, "Part 11: Wireless LAN Medium Access Control and Physical Layer specifications; High speed Physical Layer in the 5 GHz Band," 1999.

[5] ETSI, "Broadband Radio Access Networks (BRAN); HIPERLAN Type 2; Physical (PHY) Layer," *TS 101 475-2 V1.3.1*, Oct. 2001.

[6] IEEE Std. 802.16a-2003, "Air Interface for Fixed Broadband Wireless Access Systems – Amendment 2: Medium Access Control Modifications and Additional Physical Layer Specifications for 2-11 GHz," Apr. 2003.

[7] ETSI, "High Performance metropolitan local area networks (HIPERMAN), Part 1: Physical layer," *TS 102 177*, Feb. 2003.

[8] Third Generation Partnership Project (3GPP), "Wideband CDMA standards," *website: www.3gpp.org*.

[9] Wireless World Research Forum (WWRF), *website: www.wireless-world-research.org*.

[10] S. B. Weinstein, P. M. Ebert, "Data Transmission by Frequency-Division Multiplexing using the Discrete Fourier Transform," *IEEE Transactions on Communications Technology*, vol. 19, no. 5, pp. 628-634, Oct. 1971.

[11] R. van Nee, R. Prasad, "OFDM for wireless multimedia communications," *Artech House Publishers*, 2000.

[12] Third Generation Partnership Project 2 (3GPP2), "Cdma2000 standards," *website: www.3gpp2.org*.

[13] IST European project MATRICE, "MC-CDMA Transmission Techniques for Integrated Broadband Cellular Systems," *website: www.ist-matrice.org*.

[14] IST European project 4MORE, "4G MC-CDMA multiple antenna system On chip for Radio Enhancements," *website: www.ist-4more.org*.

[15] IST European project WINNER, "Wireless World Initiative New Radio," *website: www.ist-winner.org*.

[16] R. Prasad, "CDMA for Wireless Personal Communications," *Artech House Publishers*, 1996.

[17] A. J. Viterbi, "CDMA: Principles of Spread Spectrum Communication," *Addison-Wesley Publishing Company*, 1995.

[18] N. Yee, J. P. Linnartz, G. Fettweis, "Multi-Carrier CDMA in an Indoor Wireless Radio Channel," *Proc. IEEE International Symposium on Personal, Indoor and Mobile Radio Communications (PIMRC'93)*, vol. 1, pp. 109-113, Sep. 1993.

[19] K. Fazel, "Performance of CDMA/OFDM for mobile communication systems," *Proc. IEEE International Conference on Universal Personal Communications (ICUPC'93)*, pp. 975-979, Oct. 1993.

[20] A. Chouly, A. Brajal, S. Jourdan, "Orthogonal Multi-carrier Techniques Applied to Direct Sequence Spread Spectrum CDMA Systems," *Proc. IEEE Global Telecommunications Conference (GLOBECOM'93)*, pp. 1723-1728, Nov. 1993.

[21] V. DaSilva, E. Sousa, "Performance of Orthogonal CDMA Codes for Quasi-Synchronous Communication Systems," *Proc. IEEE International Conference on Universal Personal Communications (ICUPC'93)*, vol. 2, pp. 995-999, Oct. 1993.

[22] L. Vandendorpe, "Multi-tone Spread Spectrum Communications System in an Indoor Wireless Channel," *Proc. of First IEEE Symposium on Communications and Vehicular Technology in the Benelux*, pp. 4.1-1/4.1-8, Oct. 1993.

[23] Flarion Technologies, "FLASH-OFDM solutions," *website: www.flarion.com*.

[24] H. Atarashi, N. Maeda, S. Abeta, M. Sawahashi, "Broadband Packet Wireless Access based on VSF-OFCDM and MC/DS-CDMA," *Proc. IEEE International Symposium on Personal, Indoor and Mobile Radio Communications (PIMRC'02)*, pp. 992-997, Sep. 2002.

[25] A. Persson, T. Ottosson, E. Ström, "Time-frequency localized CDMA for downlink multi-carrier systems," *Proc. IEEE International Symposium on Spread Spectrum Techniques and Applications (ISSSTA 2002)*, vol. 1, pp. 118-122, Sep. 2002.

[26] K. Fazel, S. Kaiser, "Multi-Carrier and Spread Spectrum Systems," *John Wiley & Sons Ltd.*, 2003.

[27] L. Vandendorpe, "Multi-tone Spread Spectrum Multiple Access Communications System in a Multipath Rician Fading Channel," *IEEE Transactions on Vehicular Technology*, vol. 44, no. 2, pp. 327-337, May 1995.

[28] S. Hara, R. Prasad, "Overview of Multi-Carrier CDMA," *IEEE Communications Magazine*, vol. 35, no. 12, pp. 126-133, Dec. 1997.

[29] V. DaSilva, E. Sousa, "Multi-Carrier Orthogonal CDMA Signals for Quasi-Synchronous Communication Systems," *IEEE Journal on Selected Areas in Communications (JSAC)*, vol. 12, no. 5, June 1994.

[30] Third Generation Partnership Project (3GPP), "Feasibility Study for OFDM for UTRAN enhancement," *TSGRAN TR 25.892 V2.0.0*, June 2004.

Chapter 4

MC-CDMA in the Downlink of a Cellular System

This chapter presents the MC-CDMA technique in the downlink of a multi-cellular system, which is the context of interest of this thesis. It describes in details the main transmission and reception modules that are of interest within the framework of the thesis.

4.1 Transmitter structure

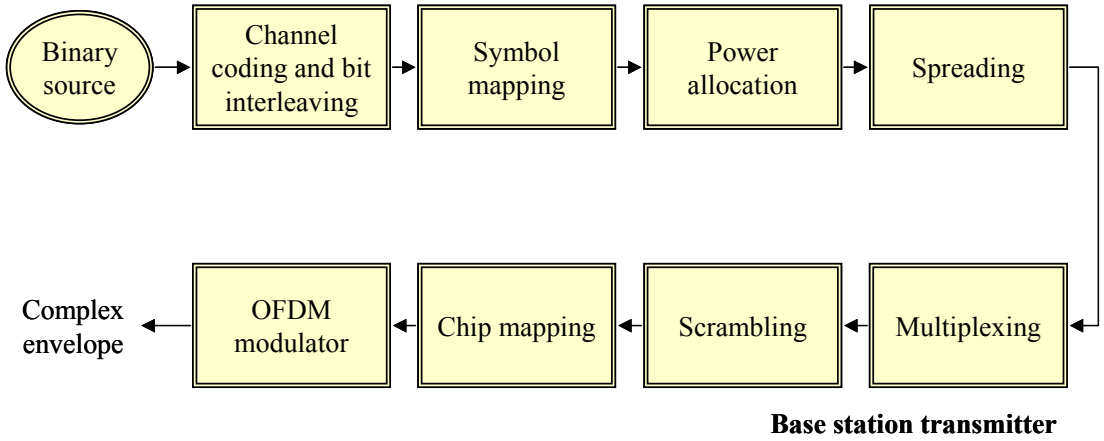

Figure 4-1: Structure of the MC-CDMA base station transmitter.

Figure 4-1 depicts a block diagram of the baseband MC-CDMA base station (BS) transmitter. The number of active users that are served simultaneously by BS_q is denoted by K_q. The binary information streams of the K_q users are first individually encoded and interleaved. The resulting bits are then mapped to data symbols according to the symbol mapping rule. Each data symbol of a user is then multiplied by the square root of the power allocated by the BS to the user. After power allocation, the data symbols of a user are spread with the user-specific spreading code. Next, the resulting chips of the K_q users are chip-wise added together and then chip-wise multiplied by the BS-specific scrambling code. The chips are then mapped to OFDM time and frequency positions according to the chip mapping strategy. After chip mapping, the chips are sent to the OFDM modulator, which performs the IDFT operation and then inserts the guard interval. At last, the complex envelope signal is RF modulated and then sent through the multi-path channels of the K_q users.

4.1.1 Channel Coding and Bit Interleaving

The role of channel coding is to protect the binary information from noise and interference encountered in the transmission of the signal through the communication channel. Channel coding is mostly accomplished by introducing in a controlled manner some redundancy in the binary information stream, which can be used at the receiver in order to detect and correct the bit errors that may occur in the transmission. The encoding process generally takes a block of k information bits and maps it into a block of n coded bits, called a *codeword*. The amount of redundancy introduced by the channel encoder is measured by the ratio $R_c = k/n$, which is referred to as the *code rate*.

There are two main classes of channel codes, namely, *block codes* and *convolutional codes* [1]. Block codes map a block of k information bits into a block of n coded bits by performing some arithmetic operations on the finite algebraic field. The basic theory of block codes was developed by Golay [2] and Hamming [3] with the introduction of the binary multiple-error correcting Golay code and the single-error correcting Hamming codes. Other commonly used block codes are BCH codes [4] and the famous Reed Solomon codes [5]. Soft input and soft output decoding of block codes has been made possible thanks to Chase algorithm [6]. This has given rise to many concatenated block codes, the most famous ones are block turbo codes introduced by Pyndiah & al. in 1994 [7].

Convolutional codes are the other major class of channel codes. They were first introduced by Elias in 1955 [8]. These codes convert the entire binary information stream into one single codeword. The encoded bits depend not only on the current k input bits but also on past input bits. The existence of a maximum-likelihood decoding procedure that can be implemented with reasonable complexity is the reason for their widespread use. Such an algorithm was invented by Viterbi [9]. Another important fact is that soft input can be used and soft output can be created when decoding convolutional codes by using either BCJR algorithm [10] or SOVA algorithm [11]. Thanks to the possibility of a soft-input soft-output decoding, convolutional codes can be used to construct many different concatenated codes. The most famous class of such concatenated codes is *turbo-codes*, which were introduced by Berrou & al. in 1993 [12]. A turbo-code as in [12] is a concatenation of two parallel convolutional codes separated by a random interleaver. Such turbo-code mimics a complex random code that can however be decoded by a relatively simple iterative scheme, called turbo decoder, where each iteration consists of elementary soft input soft output decoders that decode the component codes and exchange decoding information between each other. Turbo-codes are the most

powerful codes with reasonable complexity that have emerged in the last decade especially as they enable to approach the Shannon limit capacity. The other powerful codes that have emerged in the last decade are *Low-Density Parity-Check* (LDPC) codes [13], which are serious competitors of turbo-codes.

In multi-path propagation, where fading often causes the signal to fall below the noise level over a large number of consecutive bits, bit errors occur in bursts. Most of the practical channel codes are effective when the errors caused by the channel are statistically independent and, hence, these codes cannot cope with such bursty error distribution. A pragmatic method for dealing with burst errors is to interleave the coded bits in such a way that the bursty channel is transformed into a channel having independent errors [1]. At the transmitter, the interleaver reorders the encoded data for transmission over the channel. The deinterleaver at the receiver side puts back the bits in proper order and passes them to the decoder. As a result of interleaving and deinterleaving, the correlation between fading affecting consecutive bits is destroyed and, thus, errors within a codeword appear to be independent.

In this thesis, we consider convolutional codes and turbo-codes as in [12] followed by bit interleaving. The binary information stream transmitted for a user is considered of size B_{info}. The size of the coded bit stream is $B_{code} = B_{info}/R_c$, where R_c is the channel code rate.

4.1.2 Symbol Mapping

The symbol mapping function transforms the coded bits into complex-valued data symbols taking values in a discrete alphabet of finite size M. A constellation diagram is often conveniently used for representing the alphabet in the complex plane, as illustrated in Figure 4-2. The x and y coordinates of a data symbol correspond to its real and imaginary parts, respectively. There exist different kinds of alphabets, the most common ones are *Amplitude Shift Keying* (ASK), *Phase Shift Keying* (PSK), and *Quadrature Amplitude Modulation* (QAM) [1]. There is no universal alphabet, but depending on the channel characteristics, implementation constraints, and required level of performance, some alphabets will prove a better fit than others.

The mapping operation is done by selecting for each block of $k = \log_2(M)$ coded bits the corresponding complex-valued data symbol from $M = 2^k$ constellation symbols available for transmission over the channel. The mapping of k bits to one of the M available data symbols may be done in several ways. The preferred way called *Gray mapping* is one in which neighboring points in the constellation only differ by one single bit [1].

Here, within this thesis, the performances of MC-CDMA systems are evaluated using *Quadrature* PSK (QPSK) and 16QAM constellations with Gray mapping. As depicted in Figure 4-2, the QPSK and 16QAM constellations are normalized such that the average energy spent for the transmission of a data symbol equals 1. By taking into account the code rate, the average energy spent for the transmission of an information bit is therefore given by

$$E_b = \frac{1}{R_c \log_2(M)} \tag{4.1}$$

Since $\log_2(M)$ coded bits are mapped onto one data symbol, the size of the data symbol stream is therefore equal to $B_{data} = B_{code}/\log_2(M)$.

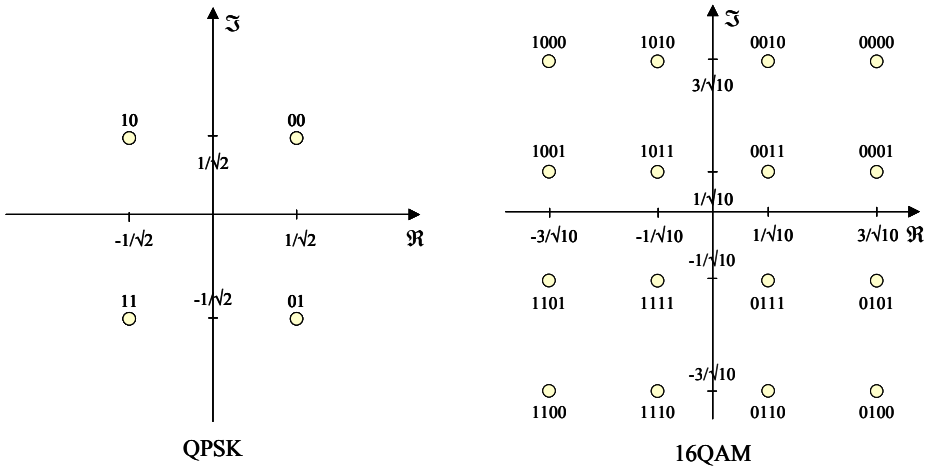

Figure 4-2: QPSK and 16QAM normalized constellations with Gray mapping.

4.1.3 Spreading and Multiplexing

The spreading module multiplies each data symbol of a user by the user-specific spreading code. If we let $\mathbf{c}^{(qk)}$ be the spreading code assigned by BS_q to user k and $d^{(qk)}$ a data symbol of user k, spreading $d^{(qk)}$ consists in multiplying it by all the L chips of $\mathbf{c}^{(qk)}$, which results in the spread sequence $\mathbf{s}^{(qk)}$ of length L

$$\mathbf{s}^{(qk)} = \left[s_0^{(qk)},\ldots,s_{L-1}^{(qk)}\right]^T = d^{(qk)}\left[c_0^{(qk)},\ldots,c_{L-1}^{(qk)}\right]^T = d^{(qk)}\mathbf{c}^{(qk)} \tag{4.2}$$

where $(.)^T$ denotes the vector transposition. Note that in (4.2), for the sake of simplicity, we don't consider the power allocated by BS_q to user k. When considering this power, the data symbol $d^{(qk)}$ in (4.2) should be replaced by the product $A^{(qk)}d^{(qk)}$, where $A^{(qk)}$ stands for the square root of the power $P^{(qk)}$ allocated by BS_q to user k.

Various families of spreading codes exist. These families are generally distinguished with respect to their orthogonality properties, their implementation complexity, and their impact on

both the PAPR and the *signal dynamic range* [14]. In the downlink, where the users' signals are transmitted synchronously, orthogonal spreading codes are preferred to non-orthogonal codes since they better mitigate the MAI. Examples of such orthogonal codes are Walsh-Hadamard codes, Fourier codes, and Golay codes [15]. In the asynchronous uplink, however, the orthogonality between the spreading codes cannot be guaranteed due to asynchronism and different users' channels and, thus, spreading codes are chosen here more with respect to their impact on the PAPR and signal dynamic range than to their orthogonality properties. The commonly used codes in the asynchronous uplink are Gold codes and Zadoff-Chu codes [14].

Walsh-Hadamard codes are the most common orthogonal codes for the downlink since they can simply be generated by using the recursive procedure

$$\mathbf{C}_L = \begin{bmatrix} \mathbf{C}_{L/2} & \mathbf{C}_{L/2} \\ \mathbf{C}_{L/2} & -\mathbf{C}_{L/2} \end{bmatrix} \quad ; \quad \forall L = 2^m, \quad m \geq 1, \quad \mathbf{C}_1 = 1 \tag{4.3}$$

The maximum number of available orthogonal codes is L and, thus, the maximum number of simultaneously active users is L. Walsh-Hadamard codes can easily be implemented using the *Fast Hadamard Transform* (FHT) operation [16]. In this thesis, we mostly employ Walsh-Hadamard spreading codes of fixed length L.

Thus, spreading transforms the data symbol stream with size B_{data} of each user into a chip stream of size $B_{chip} = B_{data} \times L$. The multiplexing module takes then the K_q chip streams of the K_q users and performs over them a chip-wise summation. Considering the K_q chip sequences $\mathbf{s}^{(qk)}$, their chip-wise summation results in the multi-user chip sequence

$$\mathbf{s}^{(q)} = \sum_{k=0}^{K_q-1} \mathbf{s}^{(qk)} = \left[s_0^{(q)}, \ldots, s_{L-1}^{(q)} \right]^T = \mathbf{C}^{(q)} \mathbf{d}^{(q)} \tag{4.4}$$

where $\mathbf{C}^{(q)} = [\mathbf{c}^{(q0)}, \ldots, \mathbf{c}^{(q(Kq-1))}]$ is the matrix of the K_q spreading codes and $\mathbf{d}^{(q)}$ is the vector of K_q transmitted data symbols $\{d^{(qk)}\}$

$$\mathbf{d}^{(q)} = \left[d^{(q0)}, \ldots, d^{\left(q\left(K_q-1\right)\right)} \right]^T \tag{4.5}$$

The multi-user chip stream at the output of the multiplexing module has therefore the same size B_{chip} as the single user chip stream at the output of the spreading module.

4.1.4 Scrambling

Scrambling in the downlink of CDMA cellular systems aims at separating the base stations while allowing them to use the same spreading codes for their users and to manage their codes

independently. Similarly to the spreading codes, the scrambling codes are chosen with respect to their correlation properties, implementation complexity, and impact on the PAPR. In synchronous systems, where all base stations use a common time reference, different shifts of a common PN maximum-length sequence also known as *m*-sequence are generally used for the scrambling codes. This is because the correlation between different shifts of an *m*-sequence is almost zero and generating an *m*-sequence can simply be done using a linear feedback shift register [17]. In asynchronous systems, however, Gold and Kasami sequences are generally used instead of *m*-sequences because of their much lower cross-correlations when compared to *m*-sequences [17].

In this thesis, we consider the case of a synchronous system and, thus, we use a common *m*-sequence with different offsets for the scrambling codes. The *m*-sequence denoted here by **w** is considered of length P, which is assumed to be very large compared to the spreading code length L. Scrambling consists in a chip-wise multiplication between the multi-user chip sequence **s** and a subset of L chips of the BS-specific scrambling code. Considering the input multi-user chip sequence $\mathbf{s}^{(q)}$ in (4.4), its corresponding output after scrambling is given by

$$\mathbf{x}^{(q)} = \left[x_0^{(q)}, \ldots, x_{L-1}^{(q)}\right]^T = \mathbf{W}^{(q)}\mathbf{s}^{(q)} \tag{4.6}$$

where $\mathbf{W}^{(q)}$ denotes a diagonal matrix of the subset of L chips of **w** that are involved in the scrambling operation of the sequence $\mathbf{s}^{(q)}$:

$$\mathbf{W}^{(q)} = \mathrm{diag}\left(w_0^{(q)}, \ldots, w_{L-1}^{(q)}\right) \tag{4.7}$$

It is of interest to note here that the values of P and L are prime in order to randomize the subset of scrambling chips $\{w_\ell^{(q)}\}$ over the consecutive data symbols.

4.1.5 Chip Mapping

The role of chip mapping is to allocate the multi-user chips to OFDM time and frequency positions. There are two main chip mapping strategies. The first strategy aims at exploiting the overall time and frequency diversity offered by the channel, while the second strategy aims at preserving orthogonality between the users' signals at the receiver side.

The first strategy consists in allocating the chips of the spread sequence **x** in (4.6) to as distant time-frequency positions as possible so that all chips of **x** are faded independently as far as possible. This can efficiently be realized by using a sufficiently long spreading code and properly interleaving the chips in time and frequency. Thanks to independent fading over the

chips of a data symbol, a diversity gain is available here that may be exploited by an adequate receiver, but at the expense of a high MAI level since orthogonality between the users' signals is destroyed due to independent chip fading. A typical scheme applying this strategy is one dimensional *Interleaved Frequency domain Mapping* (IFM) [18][19]. The main reason behind not performing interleaving in the time domain is that time interleaving may cause an important latency in the transmission since the receiver has to wait for a large number of consecutive OFDM symbols in order to perform despreading, all the more as the availability of time diversity will strongly depend on the user mobility.

Unlike the first strategy, the second strategy allocates the chips to as close time-frequency positions as possible in order to get all the chips of **x** similarly faded and, thus, preserve orthogonality between the users' signals as far as possible [20][21]. Due to the similarly faded chips, this strategy does not achieve any diversity gain, which relies on powerful channel coding and bit interleaving. A typical scheme here is one dimensional *Adjacent Frequency domain Mapping* (AFM). Other schemes applying adjacent mapping in the time domain are also of interest here since the channel coherence time typically spans a time period of several consecutive OFDM symbols.

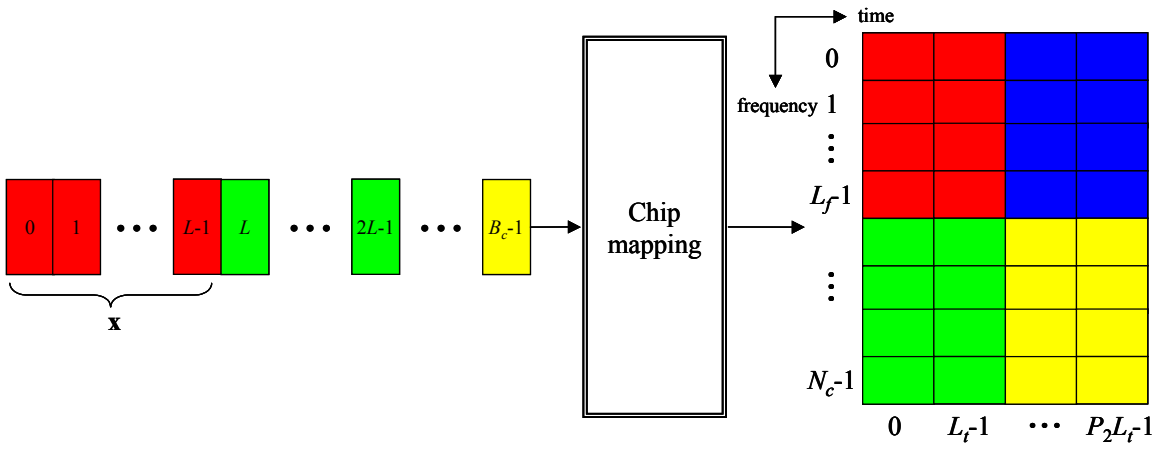

Figure 4-3: Example of adjacent time-frequency chip mapping.

Having in mind that the size of the multi-user chip stream is B_{chip} and denoting by N_c the number of OFDM sub-carriers available for data, the number of OFDM sub-carriers L_f and the number of OFDM symbols L_t used to transmit the chips of a data symbol should therefore fulfill the following conditions

$$L = L_f L_t \quad ; \quad \frac{N_c}{L_f} = P_1 \quad ; \quad \frac{B_{chip}}{N_c L_t} = P_2 \tag{4.8}$$

where P_1 and P_2 are integers.

Figure 4-3 illustrates an example of adjacent time-frequency mapping with the following parameters B_{chip} = 32, N_c = 8, L = 8, L_f = 4, and L_t = 2. In this example, there are 4 data symbols depicted with 4 different colors. The 8 chips of each spread data symbol are mapped onto 4 adjacent sub-carriers and 2 consecutive OFDM symbols.

4.2 Receiver structure and Detection Techniques

Figure 4-4 depicts a block diagram of the baseband MC-CDMA mobile station receiver.

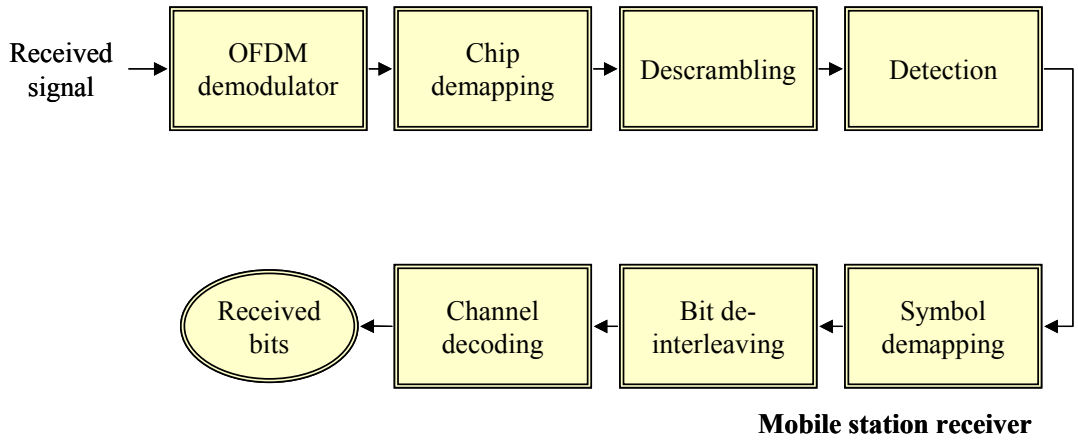

Figure 4-4: Structure of the MC-CDMA mobile station receiver.

At the receiver, the received signal is first sampled and OFDM demodulated by removing the guard interval and performing the DFT operation. The resulting chips are then demapped according to the chip mapping strategy employed by the transmitter. After descrambling with a locally generated synchronous replica of the BS-specific scrambling code, detection including despreading and equalization is performed in order to obtain the decision variable stream of the desired user. The decision variables are then symbol demapped providing either hard or soft values of the received bits, which in turn are then de-interleaved and decoded in order to recover the transmitted binary information.

4.2.1 Received Signal

In addition to thermal noise, the signal received by the desired user k connected to BS_q is the superposition of all the multi-user signals coming from all the base stations in the system. Denoting by $s^{(m)}(t)$ the transmission signal of BS_m and by $h^{(mk)}(t,\tau)$ the impulse channel response between BS_m and user k, the signal received by user k has the form

$$r^{(qk)}(t)=\sum_{m=0}^{Q-1}\int_{0}^{\tau_{\max}} s^{(m)}(t-\tau)h^{(mk)}(t,\tau)d\tau+\nu(t) \tag{4.9}$$

where Q stands for the number of base stations, τ_{max} denotes the maximum delay of all the multi-path channels $\{h^{(mk)}(t,\tau)\}$ including also synchronization errors and propagation time between the BS, and $\nu(t)$ is the thermal noise signal.

By assuming that the guard interval is longer than the maximum delay τ_{max} and that the channels $\{h^{(mk)}(t,\tau)\}$ are time invariant during the ISI-free time period T_s, the transmitted sequence $\mathbf{x}^{(q)}$ received by user k can then be obtained from (3.7) as

$$\mathbf{y}^{(qk)}=\left[y_0^{(qk)},\ldots,y_{L-1}^{(qk)}\right]^T=\mathbf{H}^{(qk)}\mathbf{x}^{(q)}+\sum_{m=0,m\neq q}^{Q-1}\mathbf{H}^{(mk)}\mathbf{x}^{(m)}+\mathbf{v} \tag{4.10}$$

where $\mathbf{H}^{(mk)}$ is a diagonal matrix representing the channel fading between user k and BS$_m$:

$$\mathbf{H}^{(mk)}=\mathrm{diag}\left(h_0^{(mk)},\ldots,h_{L-1}^{(mk)}\right) \tag{4.11}$$

The variable $h_\ell^{(mk)}$ in (4.11) is the complex-valued fading coefficient multiplying the ℓ-th chip of the transmitted sequence $\mathbf{x}^{(m)}$. In (4.10), we assume that the BS are all synchronized at the data symbol level, and they use the same family of spreading codes and the same chip mapping strategy.

The received sequence $\mathbf{y}^{(qk)}$ in (4.10) appears therefore as the summation of three terms, which are the respective contributions of the desired BS$_q$, the interfering BS, and the thermal noise. The sequence $\mathbf{y}^{(qk)}$ after descrambling results then in the sequence

$$\mathbf{r}^{(qk)}=\left[r_0^{(qk)},\ldots,r_{L-1}^{(qk)}\right]^T=\mathbf{W}^{(q)}\mathbf{y}^{(qk)} \tag{4.12}$$

Making use of (4.4), (4.6), (4.10), and (4.12), the sequence $\mathbf{r}^{(qk)}$ can be written as

$$\mathbf{r}^{(qk)}=\mathbf{H}^{(qk)}\mathbf{C}^{(q)}\mathbf{d}^{(q)}+\sum_{m=0,m\neq q}^{Q-1}\mathbf{H}^{(mk)}\mathbf{W}^{(q)}\mathbf{W}^{(m)}\mathbf{C}^{(m)}\mathbf{d}^{(m)}+\mathbf{W}^{(q)}\mathbf{v} \tag{4.13}$$

The ℓ-th chip of the sequence $\mathbf{r}^{(qk)}$ in (4.13) is given by

$$r_\ell^{(qk)}=\underbrace{h_\ell^{(qk)}c_\ell^{(qk)}d^{(qk)}}_{\text{Desired term}}+\underbrace{h_\ell^{(qk)}\sum_{j=0,j\neq k}^{K_q-1}c_\ell^{(qj)}d^{(qj)}}_{\text{Intra-cell interference}}+\underbrace{\sum_{m=0,m\neq q}^{Q-1}h_\ell^{(mk)}w_\ell^{(q)}w_\ell^{(m)}\sum_{j=0}^{K_m-1}c_\ell^{(mj)}d^{(mj)}}_{\text{Inter-cell interference}}+\underbrace{w_\ell^{(q)}\nu_\ell}_{\text{Noise term}} \tag{4.14}$$

Thus, as shown in (4.14), the ℓ-th chip $r_\ell^{(qk)}$ is the summation of four terms, which are the desired symbol, intra-cell interference, inter-cell interference, and thermal noise. The desired symbol contains the data symbol $d^{(qk)}$ transmitted to the desired user k, while the intra-cell interference sums the interference coming from all other users that are connected to the same BS_q as the desired user. The inter-cell interference sums the interference coming from all users that are connected to all base stations other than BS_q.

4.2.2 Detection Techniques

The goal of detection techniques is to recover the transmitted data symbols. Various detection strategies exist, and they are classified as either *Single-User Detection* (SUD) or *Multi-User Detection* (MUD).

4.2.2.1 Single-User Detection

SUD techniques detect only the data symbols of the desired user and do not take into account any *a priori* information about the structure of MAI. SUD consists of a chip-per-chip equalization followed by a despreading. Figure 4-5 depicts a block diagram of SUD at the receiver of the desired user k.

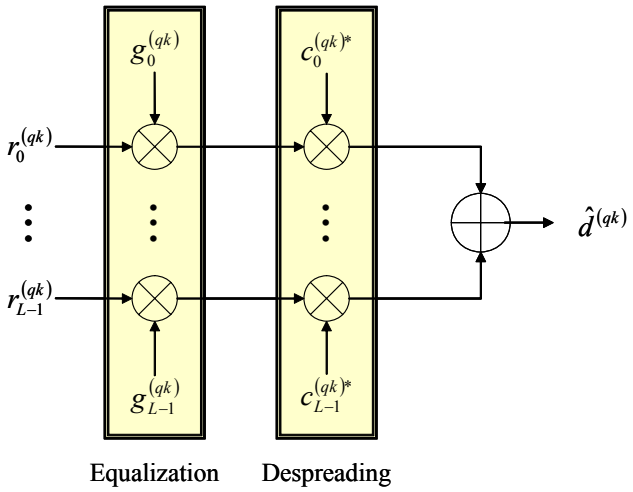

Figure 4-5: Single-user detection.

The equalization aims at compensating for the distortion due to channel fading on each received chip of a data symbol. It consists simply in one complex-valued multiplication per received chip. The sequence at the output of the equalizer has the general form

$$\mathbf{u}^{(qk)} = \left[u_0^{(qk)}, \ldots, u_{L-1}^{(qk)}\right]^T = \mathbf{G}^{(qk)}\mathbf{r}^{(qk)} \tag{4.15}$$

where $\mathbf{r}^{(qk)}$ is the sequence given in (4.13) and $\mathbf{G}^{(qk)}$ is a diagonal matrix of the L complex-valued equalization coefficients:

$$\mathbf{G}^{(qk)} = \mathrm{diag}\left(g_0^{(qk)},\ldots,g_{L-1}^{(qk)}\right) \tag{4.16}$$

After equalization, the output sequence $\mathbf{u}^{(qk)}$ is despread by multiplying it with $\mathbf{c}^{(qk)H}$, which is the transpose complex conjugate of the spreading code $\mathbf{c}^{(qk)}$. The decision variable obtained after despreading is therefore obtained as

$$\hat{d}^{(qk)} = \mathbf{c}^{(qk)H}\mathbf{u}^{(qk)} \tag{4.17}$$

From (4.14), (4.15), and (4.16), the decision variable in (4.17) can be rewritten as

$$\hat{d}^{(qk)} = I_{qk}^{(qk)} + I_{\text{intra}}^{(qk)} + I_{\text{inter}}^{(qk)} + N^{(qk)} \tag{4.18}$$

where $I_{qk}^{(qk)}$, $I_{\text{intra}}^{(qk)}$, $I_{\text{inter}}^{(qk)}$, and $N^{(qk)}$ stand respectively for the useful term, intra-cell interference, inter-cell interference, and thermal noise, which are given in Table 4-1 below.

Useful term	$I_{qk}^{(qk)} = \left(\sum_{\ell=0}^{L-1} g_\ell^{(qk)} h_\ell^{(qk)} \left\lvert c_\ell^{(qk)}\right\rvert^2\right) d^{(qk)}$
Intra-cell interference	$I_{\text{intra}}^{(qk)} = \sum_{j=0, j\neq k}^{K_q-1} I_{qj}^{(qk)} \quad I_{qj}^{(qk)} = \left(\sum_{\ell=0}^{L-1} g_\ell^{(qk)} h_\ell^{(qk)} c_\ell^{(qk)*} c_\ell^{(qj)}\right) d^{(qj)}$
Inter-cell interference	$I_{\text{inter}}^{(qk)} = \sum_{m=0, m\neq q}^{Q-1} \sum_{j=0}^{K_m-1} I_{mj}^{(qk)} \quad I_{mj}^{(qk)} = \left(\sum_{\ell=0}^{L-1} g_\ell^{(qk)} h_\ell^{(mk)} w_\ell^{(q)} w_\ell^{(m)} c_\ell^{(qk)*} c_\ell^{(mj)}\right) d^{(mj)}$
Thermal noise	$N^{(qk)} = \sum_{\ell=0}^{L-1} g_\ell^{(qk)} c_\ell^{(qk)*} w_\ell^{(q)} v_\ell$

Table 4-1: Expressions of the different terms in the MC-CDMA decision variable.

Various SUD methods exist, each having its advantages and disadvantages. The principles of the most common methods are presented in the following [19].

Maximum Ratio Combining

Maximum Ratio Combining (MRC) simply weights each received chip with the complex conjugate of the corresponding channel coefficient. The equalization coefficient multiplying the ℓ-th chip is therefore given by

$$g_\ell^{(qk)} = h_\ell^{(qk)*} \tag{4.19}$$

MRC maximizes the *Signal to Noise Ratio* (SNR) and, thus, it is optimum in the single user case when there is no intra-cell interference. However, with multiple users, MRC has the disastrous effect of amplifying the intra-cell interference because of squaring the channel coefficients after equalization.

Equal Gain Combining

Equal Gain Combining (EGC) compensates only for the phases of the channel coefficients and ensures an identical amplitude equal to 1 for all the equalization coefficients. The ℓ-th equalization coefficient is given by

$$g_{\ell}^{(qk)} = \frac{h_{\ell}^{(qk)*}}{\left|h_{\ell}^{(qk)}\right|} \tag{4.20}$$

EGC is often used as the reference SUD method thanks to its acceptable performance and its simplicity since it only needs information about the phases of the channel coefficients.

Orthogonality Restoring Combining

Orthogonality Restoring Combining (ORC) also known as *Zero Forcing* (ZF) restores completely the orthogonality between the signals of the intra-cell interfering users. It performs channel inversion with an equalization coefficient

$$g_{\ell}^{(qk)} = \frac{h_{\ell}^{(qk)*}}{\left|h_{\ell}^{(qk)}\right|^2} \tag{4.21}$$

Thus, ORC forces the intra-cell interference to zero, but in return, it enhances the thermal noise power coming from chips in deep fading.

Minimum Mean Square Error Combining

Minimum Mean Square Error Combining (MMSEC) applies the equalization coefficients that minimize the mean square value of the error between the transmitted data symbol and decision variable. The equalization coefficients are found according to

$$\mathbf{G}_{\min}^{(qk)} = \arg\min_{\mathbf{G}^{(qk)}}\left(E\left\{\left|d^{(qk)} - \hat{d}^{(qk)}\right|^2\right\}\right) = \arg\min_{\mathbf{G}^{(qk)}}\left(E\left\{\left|d^{(qk)} - \mathbf{c}^{(qk)H}\mathbf{G}^{(qk)}\mathbf{r}^{(qk)}\right|^2\right\}\right) \tag{4.22}$$

where $E\{.\}$ denotes the expectation value. It is taken here with respect to all possible data symbols and with respect to thermal noise. The solution of (4.22) is given by

$$\mathbf{c}^{(qk)H}\mathbf{G}_{\min}^{(qk)} = E\left\{d^{(qk)}\mathbf{r}^{(qk)}\right\}E\left\{\mathbf{r}^{(qk)}\mathbf{r}^{(qk)H}\right\}^{-1} \tag{4.23}$$

By assuming independent channel coefficients on the L received chips, the MMSEC equalization coefficient can then be found as [19]

$$g_{\ell}^{(qk)} = \frac{h_{\ell}^{(qk)*}}{\frac{K_q}{L}\left|h_{\ell}^{(qk)}\right|^2 + \sigma^2} \tag{4.24}$$

where σ^2 denotes here the variance of the inter-cell interference plus noise. In (4.24), we assume that the spreading codes are normalized by $1/\sqrt{L}$ so that their energy is equal to 1.

MMSEC provides a good trade-off between MRC and ORC. Indeed, in the case of large variance σ^2, MMSEC tends towards MRC, however, in the inverse case when σ^2 is negligible, MMSEC tends towards ORC. Performance comparison shows that MMSEC gives the best performance when compared to all other SUD methods [22][23], but this is at the expense of higher complexity since it requires knowledge of the cell load K_q and variance σ^2. It is important to point out that the performance evaluation here is done at the link level using the traditional curves that relate the average BER and FER to the E_b/N_0 ratio per transmitted information bit.

4.2.2.2 Multi-User Detection

Unlike SUD techniques, MUD techniques use knowledge about the structure of the intra-cell interference and detect simultaneously the data symbols of all users that are connected to the base station under consideration. MUD techniques outperform SUD techniques but at the expense of much higher complexity. This penalizes MUD for the downlink, where the mobile station receiver is subject to tight constraints with respect to power consumption and implementation complexity. However, MUD techniques can be advantageously applied in the uplink since higher complexity can generally be tolerated at the base station, and because the data from all users are required.

MUD techniques are classified into two categories: *Joint Detection* (JD) and *Interference Cancellation* (IC) [24]. JD techniques detect at once the vector $\mathbf{d}^{(q)}$ of transmitted data symbols for all the K_q users that are connected to BS_q. A well-known and optimum JD technique is achieved with the maximum likelihood criterion.

Maximum Likelihood

Maximum Likelihood (ML) minimizes the joint symbol error probability for all the data symbols in vector $\mathbf{d}^{(q)}$ by maximizing the conditional probability $\Pr\{\mathbf{d}^{(q)}|\mathbf{r}^{(qk)}\}$ that $\mathbf{d}^{(q)}$ was transmitted given the received sequence $\mathbf{r}^{(qk)}$ [24]:

$$\hat{\mathbf{d}}^{(q)} = \arg\max_{\mathbf{d}^{(q)}} \Pr\left\{\mathbf{d}^{(q)} \middle| \mathbf{r}^{(qk)}\right\} \tag{4.25}$$

The received sequence $\mathbf{r}^{(qk)}$ given in (4.13) has the following vector form

$$\mathbf{r}^{(qk)} = \mathbf{A}^{(qk)}\mathbf{d}^{(q)} + \mathbf{b}^{(qk)} \tag{4.26}$$

where $\mathbf{A}^{(qk)}$ is the intra-cell interference matrix, and $\mathbf{b}^{(qk)}$ gathers the inter-cell interference plus thermal noise terms. Thus, in the case of white Gaussian vector $\mathbf{b}^{(qk)}$, ML detection consists in finding among all possible transmitted sequences the sequence whose squared Euclidean distance from the received sequence $\mathbf{r}^{(qk)}$ is minimum. This can be written as

$$\hat{\mathbf{d}}^{(q)} = \arg\min_{\mathbf{d}^{(q)}} \left\| \mathbf{r}^{(qk)} - \mathbf{A}^{(qk)}\mathbf{d}^{(q)} \right\|^2 \tag{4.27}$$

For an alphabet of size M, ML detection requires the evaluation of M^{Kq} squared Euclidean distances for optimal estimation of the data symbol vector $\mathbf{d}^{(q)}$. Thus, the complexity of ML technique increases exponentially with respect to the number of users K_q. Sphere decoding [25] and other similar tree search based algorithms [26] provide a simplification of ML detection with a complexity that is polynomial in K_q [27].

Compared to ML technique, less-complex but sub-optimum JD techniques exist, namely, *Zero Forcing* (ZF)-MUD and *Minimum Mean Square Error* (MMSE)-MUD [24].

Zero Forcing Multi-User Detection

The ZF-MUD technique is the multi-user extension of ORC-SUD technique. Here, the intra-cell interference is cancelled by multiplying the received vector $\mathbf{r}^{(qk)}$ by the pseudo-inverse of the intra-cell interference matrix $\mathbf{A}^{(qk)}$:

$$\hat{\mathbf{d}}^{(q)} = \left(\mathbf{A}^{(qk)H}\mathbf{A}^{(qk)}\right)^{-1}\mathbf{A}^{(qk)H}\mathbf{r}^{(qk)} \tag{4.28}$$

Thus, similarly to ORC-SUD, ZF-MUD also suffers from noise enhancement due to channel inversion.

Minimum Mean Square Error Multi-User Detection

The MMSE-MUD technique multiplies the received vector $\mathbf{r}^{(qk)}$ by the matrix $\mathbf{G}^{(qk)}$ that minimizes the mean square error between the detected and transmitted data vectors [24]:

$$\mathbf{G}^{(qk)} = \left(\mathbf{A}^{(qk)H}\mathbf{A}^{(qk)} + \sigma^2\mathbf{I}\right)^{-1}\mathbf{A}^{(qk)H} \tag{4.29}$$

where σ^2 denotes the variance of the inter-cell interference plus noise. MMSE-MUD realizes a trade-off between intra-cell interference suppression and noise enhancement, which maximizes the *Signal to Interference plus Noise Ratio* (SINR).

Interference Cancellation

The principle of IC techniques is to estimate the intra-cell interference and to subtract it from the received signal for better detection of the data symbols. There are mainly two IC techniques, namely, *Successive Interference Cancellation* (SIC) and *Parallel Interference Cancellation* (PIC) [24][28][29].

In SIC technique [24], the users are ordered according to their signal strength, and the user with highest signal strength is first detected using SUD technique, and his interference contribution is then reconstructed and subtracted from the received signal. The second user is then detected similarly using the signal resulting from the previous stage, which benefits from a lower intra-cell interference than the original received signal. The other remaining users are then detected successively by following the same procedure as for the first and second users. SIC technique is particularly advantageous when the users' signals are received with different strengths. Figure 4-6 shows the principle of SIC technique.

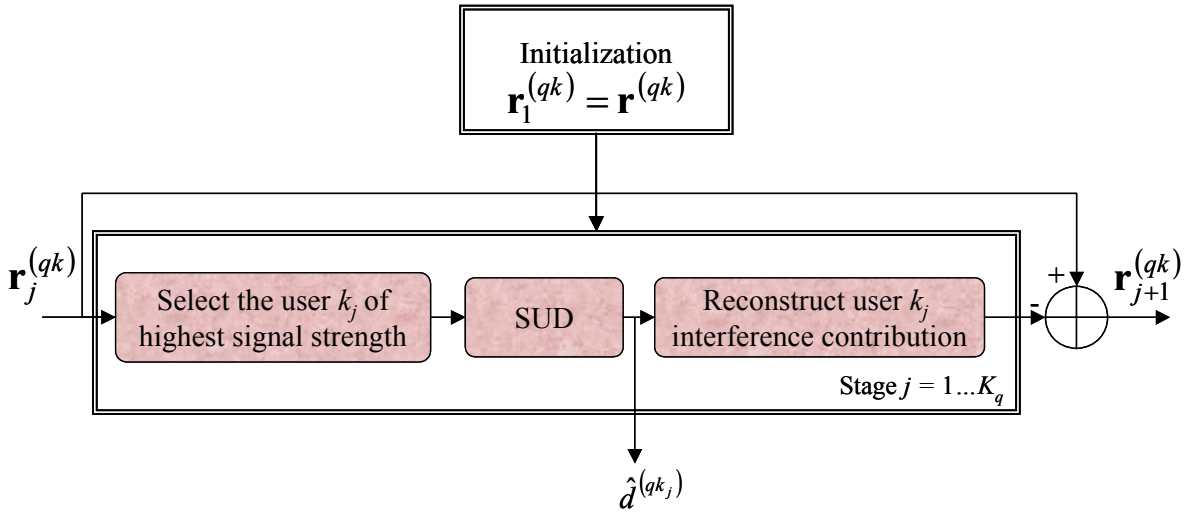

Figure 4-6: Principle of successive interference cancellation.

In PIC technique [24][29], all users are detected in parallel with SUD or JD-MUD technique, and the intra-cell interference is then reconstructed and subtracted from the received signal. In the initial stage, the received signal is used to detect the users' symbols, while in each subsequent stage, the users' symbols are detected using the signals resulting from the previous stage. The intra-cell interference reduction is mainly achieved within the first stages. PIC technique is suitable for systems where the users' signals are received with similar powers. Figure 4-7 depicts the principle of PIC technique with two stages.

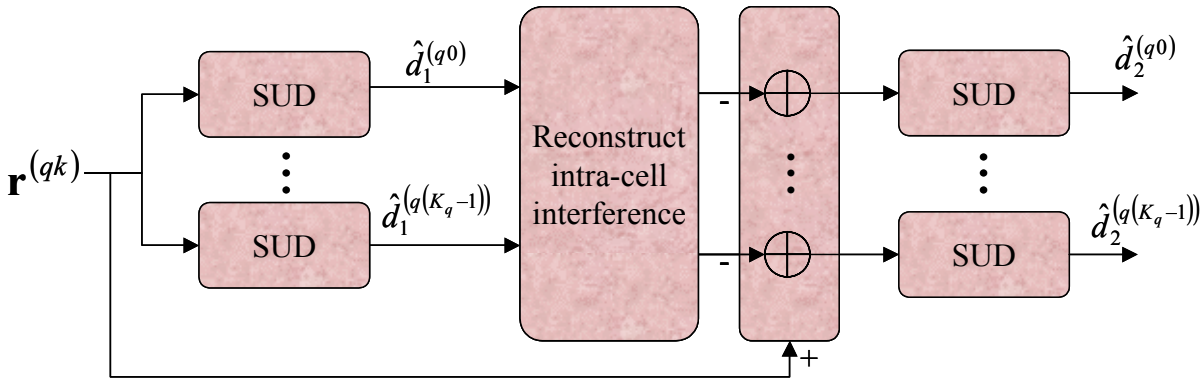

Figure 4-7: Example of parallel interference cancellation with two stages.

4.3 Conclusions

In this chapter, we presented the main baseband transmission and reception modules of MC-CDMA scheme in the downlink of a multi-cellular system.

At the base station transmitter, we described in particular the operations of spreading, scrambling, and chip mapping. While spreading aims at separating the transmissions of the different users connected to the same base station, scrambling aims at separating the transmissions of the different base stations in the system. The chip mapping maps the chips of a spread data symbol onto the OFDM time and frequency positions. It affects simultaneously the MAI and diversity and, thus, it can be optimized for a given environment in order to ensure the best trade-off between MAI and diversity.

At the mobile station receiver, we first derived the received signal before detection and then discussed the different detection techniques. These techniques are classified as either single-user detection (SUD) or multi-user detection (MUD). While SUD techniques detect only the data symbols of the desired user without using any a priori information about the structure of MAI, MUD techniques use knowledge about the structure of MAI and detect simultaneously the data symbols of all users connected to the base station under

consideration. Obviously, MUD techniques outperform SUD techniques but at the expense of much higher complexity. Since the constraints in terms of cost, size, and power consumption are very tight for mobile stations, we consider in the sequel of the thesis a low-complexity mobile station receiver with low-complexity SUD techniques.

4.4 References

[1] J. G. Proakis, "Digital Communications," *Mc-Graw Hill*, 1995.

[2] M. J. E. Golay, "Notes on Digital Coding," *Proc. IEEE*, vol. 37, p. 657, 1949.

[3] R. W. Hamming, "Error Detecting and Error Correcting Codes," *Bell System Technical Journal*, vol. 29, pp. 147-160, Apr. 1950.

[4] R. C. Bose, D. K. Ray-Chaudhuri, "On a Class of Error Correcting Binary Group Codes," *Information and Control*, vol. 3, pp. 68-79, Mar. 1960.

[5] I. S. Reed, G. Solomon, "Polynomial Codes Over Certain Finite Fields," *SIAM Journal on Applied Mathematics*, vol. 8, pp. 300-304, June 1960.

[6] D. Chase, "A Class of Algorithms for Decoding Block Codes with Channel Measurement Information," *IEEE Transactions on Information Theory*, vol. 18, pp. 170-182, Jan. 1972.

[7] R. Pyndiah, A. Glavieux, A. Picart, S. Jacq, “Near optimum decoding of product codes” *Proc. IEEE Global Telecommunications Conference (GLOBECOM'94)*, Nov. 1994.

[8] P. Elias, "Coding for Noisy Channels," *IRE Convention Record*, vol. 4, pp. 37-47, 1955.

[9] A. J. Viterbi, "Error Bounds for Convolutional Codes and an Asymptotically Optimum Decoding Algorithm," *IEEE Transactions on Information Technology*, vol. IT-13, pp. 260-269, Apr. 1967.

[10] L. R. Bahl, K. Cocke, F. Jelinek, J. Raviv, "Optimal Decoding of Linear Codes for Minimizing Symbol Error Rate," *IEEE Transactions on Information Theory*, pp. 284-287, Mar. 1974.

[11] J. Hagenauer, P. Hoeher, "A Viterbi algorithm with soft-decision outputs and its applications," *Proc. IEEE Global Telecommunications Conference (GLOBECOM'89)*, pp. 2505-2509, Nov. 1989.

[12] C. Berrou, A. Glavieux, P. Thitimajshima, "Near Shannon limit error-correcting coding and decoding: Turbo Codes," *Proc. IEEE International Conference on Communications (ICC'93)*, pp. 1064-1070, May 1993.

[13] D. J. C. MacKay, R. M. Neal, "Near Shannon Limit Performance of Low-Density Parity-Check Codes," *Electronics Letters*, vol. 32, no. 18, pp. 1645-1646, Aug. 1996.

[14] B. M. Popovic, "Spreading Sequences for Multi-Carrier CDMA Systems," *IEEE Transactions on Communications*, vol. 47, no. 6, June 1999.

[15] K. Fazel, S. Kaiser, "Multi-Carrier and Spread Spectrum Systems," *John Wiley & Sons Ltd.*, 2003.

[16] R. D. Brown, "A recursive Algorithm for Sequency-Ordered Fast Walsh Transforms," *IEEE Transactions on Computers*, vol. 26, no. 8, pp. 819-822, 1977.

[17] E. H. Dinan, B. Jabbari, "Spreading Codes for Direct Sequence CDMA and Wideband CDMA Cellular Networks," *IEEE Communications Magazine*, vol. 26, pp. 48-54, Sep. 1998.

[18] A. Chouly, A. Brajal, S. Jourdan, "Orthogonal Multi-carrier Techniques Applied to Direct Sequence Spread Spectrum CDMA Systems," *Proc. IEEE Global Telecommunications Conference (GLOBECOM'93)*, pp. 1723-1728, Nov. 1993.

[19] S. Hara, R. Prasad, "Overview of Multi-Carrier CDMA," *IEEE Communications Magazine*, vol. 35, no. 12, pp. 126-133, Dec. 1997.

[20] H. Atarashi, N. Maeda, S. Abeta, M. Sawahashi, "Broadband Packet Wireless Access based on VSF-OFCDM and MC/DS-CDMA," *Proc. IEEE International Symposium on Personal, Indoor and Mobile Radio Communications (PIMRC'02)*, pp. 992-997, Sep. 2002.

[21] A. Persson, T. Ottosson, E. Ström, "Time-frequency localized CDMA for downlink multi-carrier systems," *Proc. IEEE International Symposium on Spread Spectrum Techniques and Applications (ISSSTA 2002)*, vol. 1, pp. 118-122, Sep. 2002.

[22] S. Hara, R. Prasad, "Design and Performance of Multi-Carrier CDMA System in Frequency-Selective Rayleigh Fading Channels," *IEEE Transactions on Vehicular Technology*, vol. 48, no. 5, Sep. 1999.

[23] Z. Li, M. Latva-aho, "Performance Comparison of Frequency Domain Equalizers for MC-CDMA Systems," *Proc. IEEE Conference on Mobile and Wireless Networks (MWCN'01)*, pp. 85-89, Aug. 2001.

[24] S. Verdu, "Multi-User Detection," *Cambridge University Press*, 1998.

[25] L. Brunel, J. J. Boutros, "Lattice Decoding for Joint Detection in Direct-Sequence CDMA Systems," *IEEE Transactions on Information Theory*, vol. 49, no. 4, pp. 1030-1037, Apr. 2003.

[26] M. Pohst, H. Zassenhaus, "Algorithmic Algebraic Number Theory," *Cambridge University Press*, 1989.

[27] B. Hassibi, H. Vikalo, "On the Sphere Decoding Algorithm I. Expected Complexity," *IEEE Transactions on Signal Processing*, vol. 53, no. 8, pp. 2806-2818, Aug. 2005.

[28] J.Y. Baudais, J. F. Helard, J. Citerne, "An improved Linear MMSE Detection Technique for Multi-Carrier CDMA Systems: Comparison and Combination with Interference Cancellation Schemes," *European Transactions on Telecommunications*, vol. 11, no. 6, Nov. 2000.

[29] M. K. Varanasi, B. Aazhang, "Multistage detection in asynchronous cod-division multiple access communications," *IEEE Transactions on Communications*, vol. 38, no. 4, pp. 509-519, Apr. 1990.

[30] S. Abeta, H. Atarashi, M. Sawahashi, F. Adachi, "Performance of Coherent Multi-Carrier/DS-CDMA and MC-CDMA for Broadband Packet Wireless Access," *IEICE Transactions on Communications*, vol. E84-B, no. 4, Mar. 2001.

[31] K. Fazel, "Performance of CDMA/OFDM for mobile communication systems," *Proc. IEEE International Conference on Universal Personal Communications (ICUPC'93)*, pp. 975-979, Oct. 1993.

[32] IST European project MATRICE, "MC-CDMA Transmission Techniques for Integrated Broadband Cellular Systems," *website: www.ist-matrice.org*.

[33] IST European project 4MORE, "4G MC-CDMA multiple antenna system On chip for Radio Enhancements," *website: www.ist-4more.org*.

[34] IST European project WINNER, "Wireless World Initiative New Radio," *website: www.ist-winner.org*.

[35] S. Kaiser, "Multi-Carrier CDMA Mobile Radio Systems – Analysis and Optimization of Detection, Decoding and Channel Estimation," *Ph.D. thesis, VDI Fortschrittberichte*, Reihe 10, no. 531, 1998.

[36] D.N. Kalofonos, J. G. Proakis, "Performance of the multi-stage detector for a MC-CDMA system in a Rayleigh fading channel," *Proc. IEEE Global Telecommunications Conference (GLOBECOM'96)*, vol. 3, pp. 1784-1788, Nov. 1996.

[37] T. Sälzer, "Transmission Strategies Employing Multiple Antennas for the Downlink of Multi-Carrier CDMA Systems," *Ph.D. thesis, INSA-Rennes,* May 2004.

[38] Third Generation Partnership Project (3GPP) for Wideband CDMA standards, *website: www.3gpp.org*.

[39] Third Generation Partnership Project (3GPP), "Feasibility Study for OFDM for UTRAN enhancement," *TSGRAN TR 25.892 V2.0.0*, June 2004.

[40] Wireless World Research Forum (WWRF), *website: www.wireless-world-research.org*.

[41] N. Yee, J. P. Linnartz, G. Fettweis, "Multi-Carrier CDMA in an Indoor Wireless Radio Channel," *Proc. IEEE International Symposium on Personal, Indoor and Mobile Radio Communications (PIMRC'93)*, vol. 1, pp. 109-113, Sep. 1993.

Chapter 5
Multi-Frame Oriented Link to System Interface

As discussed in Chapter 1, an adequate interface between link and system level simulations is needed in order to allow the system level simulators to predict easily and accurately the transmission quality of the different links in the system. The interface is usually done by using a set of look-up tables mapping the BER and FER to an adequate SINR-based measure that can easily be calculated at the system level. This chapter presents an appropriate multi-frame oriented link to system interface for MC-CDMA cellular systems in the downlink. The multi-frame oriented interface aims at defining an easy-to-calculate SINR-based measure that maps directly to the average BER and FER, where the average is taken here over a large number of frames experiencing independent fading realizations. This interface will be particularly used in Chapter 6 for evaluating the cellular capacity for different MC-CDMA physical layer configurations through static system level simulations.

5.1 Problem Statement

The static system level simulator considers only the reference scenario of real time circuit switched services. These services are characterized by a constant information bit rate and a real time connection much longer than the fast fading coherence time. The quality of service of a radio link is evaluated in term of the FER averaged over the whole period of connection. In order to satisfy the quality of service of the radio links connected to the central base station (BS_0), the system level simulator distributes the total transmission power $P^{(0)}$ of BS_0 amongst its K_0 connected links such that all their average FER requirements are fulfilled. Let $\mathbf{p}_0$ denote the column vector of the powers allocated by BS_0 to its K_0 radio links. In order to calculate the vector $\mathbf{p}_0$, the system simulator needs to relate $\mathbf{p}_0$ to the average FER requirements and to the measured propagation and interference conditions for all the K_0 links. This can be formulated for link k as

$$FER^{(0k)} = f_{0k}\left(P^{(00)},\ldots,P^{(0k)},\ldots,P^{(0(K_0-1))}\right) = f_{0k}\left(\mathbf{p}_0\right) \tag{5.1}$$

The subscript $0k$ of function f_{0k} reflects its specificity to the propagation and interference conditions experienced by the k-th link connected to BS_0.

Without loss of generality, the function f_{0k} can be exactly expressed as the combination of a mapping function h with a compression function g_{0k}:

$$f_{0k}(\mathbf{p}_0) = h \circ g_{0k}(\mathbf{p}_0) = h\left(LQM^{(0k)}\right) \quad ; \quad LQM^{(0k)} = g_{0k}(\mathbf{p}_0) \tag{5.2}$$

The mapping function h maps the average FER to an adequate *Link Quality Measure* (LQM) that has to be defined. The function h is obtained through link level simulations and it is specific to the physical layer configuration and multi-path channel model. Ideally, h should be invariant with respect to the large-scale propagation and interference conditions experienced at the system level. The function g_{0k} is called the *compression function* since it compresses the vector $\mathbf{p}_0$ of K_0 elements into one scalar $LQM^{(0k)}$. This function should ideally summarize all the effects of large-scale propagation and interference conditions experienced by link k at the system level. Thus, under different system level propagation and interference conditions with the same value of $LQM^{(0k)}$, the link level simulation should ideally always yield the same value $h(LQM^{(0k)})$ of the average FER for a given scenario that specifies the physical layer configuration and multi-path channel model.

By writing (5.2), we have simply turned the problem in (5.1) into determining at first an appropriate LQM and then providing the mappings between the defined LQM and average FER through link level simulations. In order to determine an appropriate LQM, we follow an approach that consists of the two steps below:

- **Step 1:** Analysis and modeling of the intra-cell and inter-cell interference at the link level.
- **Step 2:** Theoretical analysis of the bit error probability followed by link level simulations. This step makes use of the interference models elaborated in Step 1.

The two aforementioned steps are basically based on an analysis of the MC-CDMA signal at the output of the SUD module, which is the position that incorporates all the specificities of the MC-CDMA technique and that allows a relatively easy theoretical analysis.

As already shown in (4.18), the received signal at the output of the SUD module is the summation of four terms: useful signal, intra-cell interference, inter-cell interference, and thermal noise. Let us consider the k-th link L_{0k} connected to BS_0. From (4.18) and by taking into account the powers and large-scale propagation losses, the decision variable associated with the transmitted data symbol $d^{(0k)}$ is obtained as

$$\hat{d}^{(0k)} = \sqrt{G^{(0k)}P^{(0k)}}\, I_{0k}^{(0k)} + \sqrt{G^{(0k)}} \sum_{j=0, j\neq k}^{K_0-1} \sqrt{P^{(0j)}}\, I_{0j}^{(0k)} + \sum_{m=1}^{Q-1} \sqrt{G^{(mk)}} \sum_{j=0}^{K_m-1} \sqrt{P^{(mj)}}\, I_{mj}^{(0k)} + N^{(0k)} \tag{5.3}$$

where $P^{(mj)}$ denotes the power allocated by BS_m to its j-th link L_{mj} and $G^{(mk)}$ denotes the path loss between BS_m and the user associated with the link L_{0k}. The interference term $I_{mj}^{(0k)}$ and thermal noise term $N^{(0k)}$ are given in Table 4-1.

In the sequel, we make the following assumptions:

- The length of the spreading codes L is sufficiently large ($L \geq 10$) and the period P of the scrambling codes is very large compared to the spreading code length L.
- The subset of L scrambling chips $\{w_\ell^{(m)}\}$ involved in the descrambling operation starts at index i_m in the common m-sequence $\mathbf{w}$. The indexes $\{i_m\}$ are independent and uniformly distributed over the period P.
- The data symbols $\{d^{(mj)}\}$ as well as the spreading codes $\{\mathbf{c}^{(mj)}\}$ are normalized so that the energy of each is equal to 1.
- The channel coefficients $\{h_\ell^{(mk)}\}$ are wide sense stationary before and after equalization. Furthermore, the channel coefficients $\{h_\ell^{(mk)}\}$ and $\{h_\ell^{(qk)}\}$ are mutually independent for $q \neq m$, and the equalization coefficients $\{g_\ell^{(0k)}\}$ are derived with perfect channel estimation.
- The macroscopic observation time period spans a large number of frames experiencing independent fading realizations. The cell loads $\{K_m\}$, the allocated powers $\{P^{(mj)}\}$, and the large-scale propagation losses $\{G^{(mk)}\}$ are fixed during the macroscopic time period. Thus, when averaging over the macroscopic time period, the statistics of only the data symbols, small-scale fading channel coefficients, and scrambling codes are concerned.

5.2 Interference Analysis and Modeling

In this section, we analyze the statistical properties and present statistical models for both the intra-cell and inter-cell interference. As mentioned previously, only the statistics of data symbols, small-scale fading channel coefficients, and scrambling codes are of interest.

5.2.1 Intra-Cell Interference

The contribution of the j-th link L_{0j} to the intra-cell interference experienced by the k-th link L_{0k} is given in Table 4-1 by

$$I_{0j}^{(0k)} = \left(\sum_{\ell=0}^{L-1} g_\ell^{(0k)} h_\ell^{(0k)} c_\ell^{(0k)*} c_\ell^{(0j)} \right) d^{(0j)} = \left(\sum_{\ell=0}^{L-1} \rho_\ell^{(0k)} c_\ell^{(0k)*} c_\ell^{(0j)} \right) d^{(0j)} \tag{5.4}$$

The coefficients $\{\rho_\ell^{(0k)}\}$ replace the products $\{g_\ell^{(0k)}h_\ell^{(0k)}\}$ and, thus, they gather all the terms in (5.4) that are functions of the small-scale fading.

5.2.1.1 First and Second Order Statistical Moments

As for data symbol $d^{(0j)}$, the mean of the mutual intra-cell interference term $I_{0j}^{(0k)}$ is equal to zero. On the other hand, its variance is obtained from (5.4) as

$$\alpha_{0j}^{(0k)} = \mathrm{ACF}_{kj}[0]\Gamma_\rho[0] + 2\Re\left(\sum_{\ell=1}^{L-1}\mathrm{ACF}_{kj}[\ell]\Gamma_\rho[\ell]\right) \tag{5.5}$$

where $\Gamma_\rho[\ell]$ denotes the chip autocorrelation function of the equalized channel coefficients $\{\rho_\ell^{(0k)}\}$ and it is defined as

$$\Gamma_\rho[\ell] = E\left\{\rho_n^{(0k)}\rho_{n-\ell}^{(0k)}\right\} \tag{5.6}$$

$\mathrm{ACF}_{kj}[\ell]$ is the aperiodic correlation function of the chip-wise product between the spreading codes $\mathbf{c}^{(0j)}$ and $\mathbf{c}^{(0k)*}$ and it is defined as

$$\mathrm{ACF}_{kj}[\ell] = \sum_{n=0}^{L-\ell-1} c_n^{(0k)*}c_n^{(0j)}c_{n+\ell}^{(0k)}c_{n+\ell}^{(0j)*} \tag{5.7}$$

In the particular case of the useful term $I_{0k}^{(0k)}$, equation (5.7) simplifies to

$$\mathrm{ACF}_{kk}[\ell] = \frac{1}{L}\left(1-\frac{\ell}{L}\right) \tag{5.8}$$

The variance of the useful signal $I_{0k}^{(0k)}$ is therefore obtained from (5.5) as

$$\alpha_{0k}^{(0k)} = \frac{1}{L}\Gamma_\rho[0] + \frac{2}{L}\sum_{\ell=1}^{L-1}\left(1-\frac{\ell}{L}\right)\Gamma_\rho[\ell] \tag{5.9}$$

The second summation term in (5.5) represents the influence of interfering spreading codes $\mathbf{c}^{(0j)}$ and $\mathbf{c}^{(0k)}$ on their mutual interference power $\alpha_{0j}^{(0k)}$ due to the correlation between the equalized channel coefficients $\{\rho_\ell^{(0k)}\}$. In particular, in the extreme case of flat fading over the L chips of the spread data symbol, the coefficients $\{\rho_\ell^{(0k)}\}$ will be highly correlated and as a result the mutual interference power $\alpha_{0j}^{(0k)}$ for $j \neq k$ will then converge to zero. This reflects the fact that flat fading preserves the orthogonality between the spreading codes. In the other extreme case of uncorrelated coefficients $\{\rho_\ell^{(0k)}\}$, the mutual interference power $\alpha_{0j}^{(0k)}$ for $j \neq k$ is significantly enhanced and converges to

$$\alpha_{0j}^{(0k)} \approx \frac{1}{L}\sigma_{\rho}^{2} \tag{5.10}$$

where σ_{ρ}^{2} denotes the variance of the coefficient $\rho_{\ell}^{(0k)}$. In this uncorrelated case as well, the mutual interference power $\alpha_{0j}^{(0k)}$ remains therefore invariant with respect to the couple $(\mathbf{c}^{(0j)},\mathbf{c}^{(0k)})$ of interfering codes. Thus, whenever we approach these two extreme cases of uncorrelated and highly correlated channel coefficients, the mutual interference power tends to be invariant with respect to the interfering spreading codes. However, between these two extreme cases, this is not necessarily true and the mutual interference power may vary with respect to the interfering spreading codes. The variation is as large as the dependency of the aperiodic correlation function ACF_{kj} on the couple $(\mathbf{c}^{(0j)},\mathbf{c}^{(0k)})$ is high. For Walsh-Hadamard and Fourier orthogonal codes, ACF_{kj} varies drastically with respect to the couple $(\mathbf{c}^{(0j)},\mathbf{c}^{(0k)})$, whereas for PN maximum length codes, the variation is much lower.

Figure 5-1 illustrates the mutual interference power $\alpha_{0j}^{(0k)}$ in dB versus the index i_{kj} of the couple $(\mathbf{c}^{(0j)},\mathbf{c}^{(0k)})$ of interfering codes for Hadamard (L = 32), Fourier (L = 32), and PN codes (L = 31) and in both cases of uncorrelated and correlated channel coefficients. The index i_{kj} represents the index of the couple $(\mathbf{c}^{(0j)},\mathbf{c}^{(0k)})$ after sorting $\alpha_{0j}^{(0k)}$ in an ascending order from its lowest to its highest values. For instance, the index i_{kj} of the couple $(\mathbf{c}^{(0j)},\mathbf{c}^{(0k)})$ that yields the highest $\alpha_{0j}^{(0k)}$ is equal to L, and that of the couple yielding the lowest $\alpha_{0j}^{(0k)}$ is equal to 1. As shown in Figure 5-1, in the uncorrelated case, the mutual interference power exhibits slight variation with respect to the interfering spreading codes. This is true independently of the family of spreading codes. In the correlated case however, a large variation can be observed for Hadamard and Fourier orthogonal codes, whereas PN codes still exhibit slight variation. This means that the aperiodic correlation function ACF_{kj} is highly dependent on the couple $(\mathbf{c}^{(0j)},\mathbf{c}^{(0k)})$ for Hadamard and Fourier codes. However, this is not the case for PN codes.

Thus, whenever the mutual interference power varies significantly with respect to the interfering spreading codes, selecting the subset of the less mutually interfering codes for a given cell load $K_0 < L$ can significantly improve the MC-CDMA system performance. This problem of optimal selection of the spreading codes for a non-fully loaded cell ($K_0 < L$) has been mainly investigated by [1] and [2]. In [2], we propose a recursive algorithm that at a given recursion selects the code which has the lowest mutual interference powers with the set of already selected codes. This algorithm is shown to provide significant gains of up to 3.5 dB

in term of minimum achieved SINR when compared to bad code selection. For more details of the proposed algorithm, the reader is referred to [2].

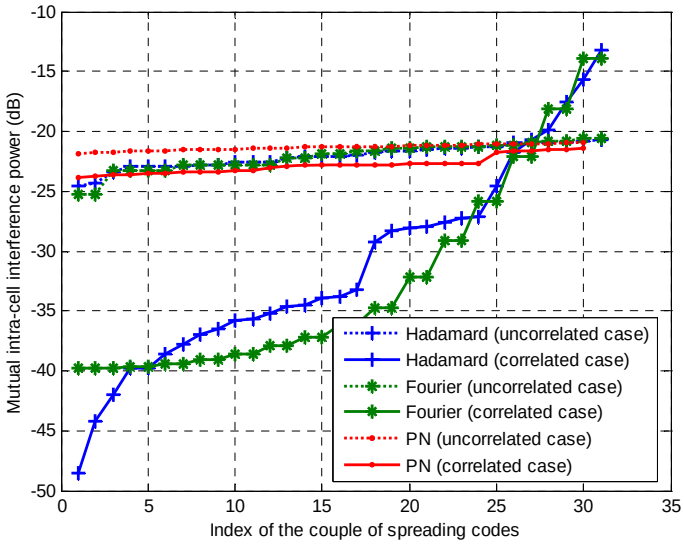

Figure 5-1: Influence of the spreading codes on their mutual intra-cell interference power.

5.2.1.2 Probability Density Function

Considering the *Probability Density Function* (PDF), it is straightforward to see from (5.4) that in case of uncorrelated coefficients $\{\rho_\ell^{(0k)}\}$, the *Central Limit Theorem* (CLT) applies to the mutual interference $I_{0j}^{(0k)}$ for a sufficiently large value of the spreading code length L, which justifies a Gaussian distribution. Moreover, all mutual interferences $\{I_{0j}^{(0k)}\}$ have zero mean and almost the same variance as shown in (5.10). Thus, in such particular case, the total intra-cell interference $I_{intra}^{(0k)}$ experienced by the link L_{0k} will also follow a zero mean Gaussian distribution with variance

$$\alpha_0^{(0k)} = G^{(0k)} \sum_{j=0, j\neq k}^{K_0-1} P^{(0j)} \alpha_{0j}^{(0k)} \approx G^{(0k)} \left(P^{(0)} - P^{(0k)}\right) \frac{\sigma_\rho^2}{L} \tag{5.11}$$

However, in the general case of correlated channel coefficients, the CLT does not apply to the mutual interference $I_{0j}^{(0k)}$ and therefore its Gaussian distribution is no longer justified. In this case, higher order statistical moments are generally required to characterize the intra-cell interference distribution. For instance, by extending to the fourth order statistical moment also referred to as the *kurtosis*, we show through simulations that the PDF model below approximates well the intra-cell interference distribution:

$$p_X(x) = a\, \mathrm{e}^{-b|x|^\eta} \tag{5.12}$$

where X denotes either the real or imaginary part of the intra-cell interference $I_{intra}^{(0k)}$. The parameters a, b, and η are derived from the variance σ_X^2 and kurtosis κ_X as

$$\kappa_X = \frac{\Gamma\left(5/\eta\right)\Gamma\left(1/\eta\right)}{\Gamma\left(3/\eta\right)^2} \quad ; \quad b = \left(\frac{\Gamma\left(3/\eta\right)}{\sigma_X^2 \Gamma\left(1/\eta\right)} \right)^{\eta/2} \quad ; \quad a = \frac{\eta b^{1/\eta}}{2\Gamma\left(1/\eta\right)} \tag{5.13}$$

The function Γ in (5.13) refers to the commonly known *Gamma function* defined as [3]

$$\Gamma(p) = \int_0^{+\infty} x^{p-1}\, \mathrm{e}^{-x}\, dx, \quad p > 0 \tag{5.14}$$

It is of interest to note here that the PDF model given in (5.12) incorporates both Gaussian ($\eta = 2$) and non Gaussian distributions. However, this PDF model is not easy to implement in practice since it requires knowledge of the fourth statistical moment, which unfortunately turns to be quite difficult to compute analytically.

In order to provide an easier and practical modeling of the intra-cell interference, we propose the so-called *Orthogonal Gaussian Noise* (OGN) model [4]. This model is justified by observing that for a large cell load K_0, the CLT applies to the intra-cell multiple access signal at the transmitter side. The ℓ-th chip of the intra-cell multiple access signal can therefore be modeled by a zero mean complex-valued Gaussian random variable $\zeta_\ell^{(0k)}$ as

$$\sum_{j=0, j\neq k}^{K_0-1} \sqrt{P^{(0j)}}\, d^{(0j)} c_\ell^{(0j)} \longleftrightarrow \zeta_\ell^{(0k)} \tag{5.15}$$

The variance σ_ζ^2 of $\zeta_\ell^{(0k)}$ is given by

$$\sigma_\zeta^2 = \frac{1}{L} \sum_{j=0, j\neq k}^{K_0-1} P^{(0j)} = \frac{1}{L}\left(P^{(0)} - P^{(0k)}\right) \tag{5.16}$$

The variables $\{\zeta_\ell^{(0k)}\}$ are chosen such that the orthogonality between the intra-cell multiple access signal and desired signal is preserved at the transmitter side. That is why this model is referred to as orthogonal Gaussian noise. The OGN variables $\{\zeta_\ell^{(0k)}\}$ are obtained as

$$\zeta_\ell^{(0k)} = B_\ell - c_\ell^{(0k)} \sum_{n=0}^{L-1} B_n c_n^{(0k)*} \tag{5.17}$$

where $\{B_\ell\}$ are L independent and identically distributed complex-valued Gaussian random variables with zero mean and variance σ_B^2. The correlation between the variables $\{\zeta_\ell^{(0k)}\}$ is found from (5.17) as

$$\Gamma_\zeta[\ell] = E\left\{\zeta_n^{(0k)}\zeta_{n-\ell}^{(0k)*}\right\} = \sigma_B^2\left(\delta_{0\ell} - c_n^{(0k)}c_{n-\ell}^{(0k)*}\right) \tag{5.18}$$

By replacing the intra-cell multiple access by the OGN variables $\{\zeta_\ell^{(0k)}\}$, the intra-cell interference experienced by L_{0k} at the output of the SUD module takes the form

$$I_{\mathrm{OGN}}^{(0k)} = \sqrt{G^{(0k)}}\left(\sum_{\ell=0}^{L-1}\zeta_\ell^{(0k)}\rho_\ell^{(0k)}c_\ell^{(0k)*}\right) \tag{5.19}$$

The variance of $I_{\mathrm{OGN}}^{(0k)}$ simplifies then to

$$\mathrm{var}\left\{I_{\mathrm{OGN}}^{(0k)}\right\} = G^{(0k)}\sigma_B^2\theta^{(0k)} \quad ; \quad \theta^{(0k)} = \left(\Gamma_\rho[0] - \alpha_{0k}^{(0k)}\right) \tag{5.20}$$

In order to check the validity of the different PDF models, Figure 5-2 illustrates the PDF of the real part of the actual intra-cell interference $\Re(I_{intra}^{(0k)})$ measured by simulation and its corresponding PDF for each of the Gaussian model, Kurtosis-based model, and OGN model. The general case of correlated channel coefficients is considered using MRC equalization. Moreover, we consider two cell loads $K_0 = 8$ (on the left) and $K_0 = 24$ (on the right) in order to highlight the validity with respect to different values of the cell load. The Gaussian model has its variance set equal to the variance of $\Re(I_{intra}^{(0k)})$ obtained from simulation. The Kurtosis-based model also uses the variance and kurtosis of $\Re(I_{intra}^{(0k)})$ measured by simulation, and the variance σ_ζ^2 of the OGN model is set equal to the transmitted intra-cell multiple access power as given in (5.16).

From Figure 5-2, we can immediately conclude that the Gaussian model is not valid. The Kurtosis-based model seems to be more appropriate than the Gaussian one and gets better as the cell load K_0 is increased. The OGN model turns out to be the most appropriate model and its performances improve as the cell load K_0 increases. Furthermore, the OGN model has the major advantage of being easy to implement since it simply requires the generation of L independent Gaussian variables $\{B_\ell\}$ followed by an orthogonal projection as given in (5.17). The OGN model is fully characterized by the variance σ_ζ^2, which is related to the intra-cell multiple access power through (5.16). This leads us to select the OGN model for modeling the intra-cell interference at the link level.

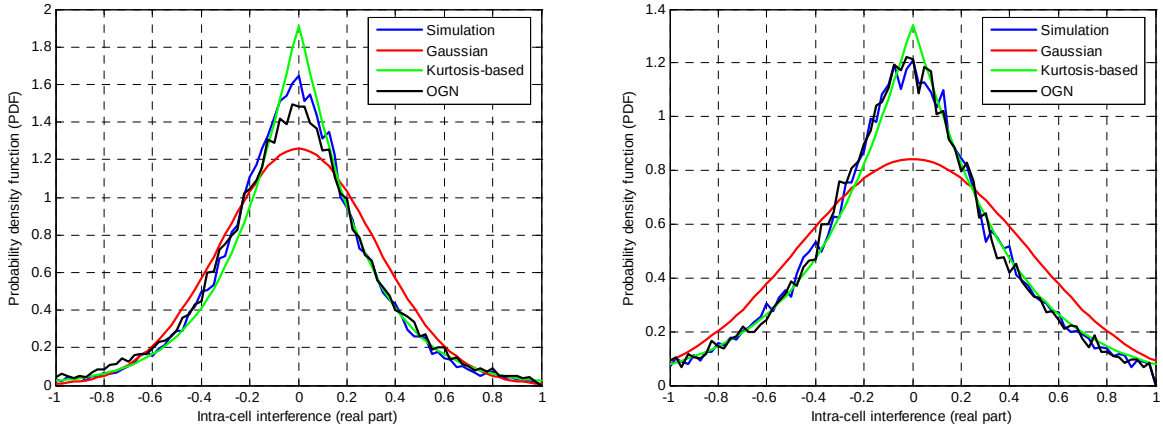

Figure 5-2: Intra-cell interference probability density functions for two different cell loads of 8 (left) and 24 (right) codes in the general case of correlated channel coefficients.

5.2.2 Inter-Cell Interference

Considering the inter-cell interference, the contribution of the link L_{mj} of BS_m to the inter-cell interference experienced by the link L_{0k} of BS_0 is given by (see Table 4-1)

$$I_{mj}^{(0k)} = \left(\sum_{\ell=0}^{L-1} g_{\ell}^{(0k)} h_{\ell}^{(mk)} w_{\ell}^{(0)} w_{\ell}^{(m)} c_{\ell}^{(0k)*} c_{\ell}^{(mj)} \right) d^{(mj)} \tag{5.21}$$

5.2.2.1 First and Second Order Statistical Moments

The mutual inter-cell interference term $I_{mj}^{(0k)}$ for $m \neq 0$ has obviously its mean equal to zero. Its variance is found from (5.21) as

$$\alpha_{mj}^{(0k)} \approx \frac{1}{L} \beta^{(0k)} \quad ; \quad \beta^{(0k)} = E\left\{ \left| g_{\ell}^{(0k)} \right|^2 \right\} \tag{5.22}$$

Equation (5.22) is obtained by using the two following properties of PN *m*-sequences [5][6], which yield the scrambling chips' correlation given in (5.23):

1) The summation of all chips in the whole period of a PN *m*-sequence is equal to –1.

2) The chip-wise product of two different PN *m*-sequences yields a PN *m*-sequence different from both initial sequences.

$$E\left\{ w_{\ell}^{(0)} w_{\ell}^{(m)} w_{\ell+n}^{(0)} w_{\ell+n}^{(m)} \right\} = \left(1 + \frac{1}{P} \right) \delta_{0n} - \frac{1}{P} \tag{5.23}$$

Equation (5.22) also makes use of the independence between the equalization coefficients $\{g_{\ell}^{(0k)}\}$ and channel coefficients $\{h_{\ell}^{(mk)}\}$ for $m \neq 0$, and of the fact that the channel coefficients

$\{h_\ell^{(mk)}\}$ are normalized such that their energy is equal to 1. Thus, as shown in (5.22), the mutual inter-cell interference power $\alpha_{mj}^{(0k)}$ is invariant with respect to the link L_{mj} and it is inversely proportional to the spreading code length L.

5.2.2.2 Probability Density Function

For a large number of interfering cells and as the channel coefficients $\{h_\ell^{(km)}\}$ and $\{h_\ell^{(kq)}\}$ are independent for $m \neq q$, the CLT applies to the total inter-cell interference after OFDM demodulation. The ℓ-th chip of the inter-cell interference can therefore be modeled by a zero mean complex-valued Gaussian random variable $\xi_\ell^{(0k)}$ as

$$\sum_{m=1}^{Q-1} \sqrt{G^{(0k)}}\, w_\ell^{(m)} h_\ell^{(mk)} \sum_{j=0}^{K_m-1} \sqrt{P^{(mj)}}\, c_\ell^{(mj)} d^{(mj)} \longleftrightarrow \xi_\ell^{(0k)} \tag{5.24}$$

The random variables $\{\xi_\ell^{(k0)}\}$ are independent and as for the thermal noise, the inter-cell interference can then be modeled by an *Additive White Gaussian Noise* (AWGN) at the input of the receiver. Thus, the inter-cell interference plus noise can simply be modeled at the link level by using an AWGN at the input of the receiver.

5.3 Analysis of the Bit Error Probability

By replacing the intra-cell multiple access at the transmitter and inter-cell interference at the input of the receiver by their OGN and AWGN models respectively, the decision variable at the output of the SUD module becomes then equal to

$$\hat{d}^{(0k)} = \sqrt{P_u}\, I_{0k}^{(0k)} + \sum_{\ell=0}^{L-1} \zeta_\ell^{(0k)} \rho_\ell^{(0k)} c_\ell^{(0k)*} + \sum_{\ell=0}^{L-1} \left(\xi_\ell^{(0k)} + v_\ell^{(0k)}\right) w_\ell^{(0)} g_\ell^{(0k)} c_\ell^{(0k)*} \tag{5.25}$$

Note that in (5.25), we change the notation of the transmission power $P^{(0k)}$ into P_u, and we omit the large-scale propagation loss $G^{(0k)}$ since the analysis is done at the link level where only the small-scale fading aspects are considered. Moreover, without loss of generality, we assume QPSK symbol mapping in the following analysis.

5.3.1 Case with no Channel Coding

With no channel coding, the decision variables are processed by a threshold detector in order to recover the transmitted data symbols. The uncoded bit error probability P_b is given by

$$P_b = \Pr\left(\Re\left(\hat{d}^{(0k)}\right) > 0 \middle| \Re\left(d^{(0k)}\right) = \frac{-1}{\sqrt{2}} \right) = \Pr\left(Z^{(0k)} > 0\right) \tag{5.26}$$

Thus, P_b is directly related to the distribution of the random variable $Z^{(0k)}$. In the context of low channel coefficients correlation, the CLT applies to both the intra-cell and inter-cell interference plus noise (cf. (5.25)) and justifies their Gaussian distributions. By applying the *Law of Large Numbers* (LLN) to the useful term $I_{0k}^{(0k)}$, P_b can then simply be written as

$$P_b = \mathrm{Q}\left(\sqrt{SINR^{(0k)}}\right) \tag{5.27}$$

where $SINR^{(0k)}$ stands for the *local mean SINR* at the output of the SUD module, i.e., the ratio between the average useful signal power and average total interference plus noise power. It has the form

$$SINR^{(0k)} = \frac{P_u \alpha_{0k}^{(0k)}}{\theta^{(0k)} \sigma_B^2 + \beta^{(0k)} \sigma_{\xi+\nu}^2} \tag{5.28}$$

where $\sigma_{\xi+\nu}^2$ denotes the inter-cell interference plus noise variance at the link level and $\theta^{(0k)}$ denotes the OGN intra-cell interference factor given in (5.20). Thus, in this context of low channel coefficients correlation, the local mean SINR is an appropriate link quality measure since it directly maps to the bit error probability through the complementary error function Q. Here, the total interference plus noise received power ($\theta^{(0k)}\sigma_B^2+\beta^{(0k)}\sigma_{\xi+\nu}^2$), which is the denominator of $SINR^{(0k)}$, fully characterizes the influence of the total interference plus noise on the uncoded bit error probability P_b.

In the context of significant channel coefficients correlation, neither the CLT nor the LLN applies, and therefore the distribution of $Z^{(0k)}$ becomes specific to the scenario characterized by the channel coefficients correlation, equalization technique, and couple ($P_u,\sigma_B^2,\sigma_{\xi+\nu}^2$). Here, the couple of variances ($\sigma_B^2,\sigma_{\xi+\nu}^2$) characterizes the influence of the intra-cell and inter-cell interference plus noise on the uncoded bit error probability. Thus, for a given scenario characterized by the channel coefficients correlation and equalization technique, different mappings between the local mean SINR and bit error probability may exist for different settings of the couple ($P_u,\sigma_B^2,\sigma_{\xi+\nu}^2$), and the larger the difference between these mappings is, the less appropriate the local mean SINR measure becomes.

5.3.2 Case with Channel Coding

Since generally there is no close form expression for the bit error probability after channel decoding, we assume that an adequate LQM that maps well to the pair-wise error probability will also map well to the average bit and frame error probabilities. This analysis especially

holds for convolutional codes but it can be extended to other types of linear codes with some adaptations. Let $P_2(C,\hat{C})$ denote the pair-wise error probability between the transmitted codeword C and estimated codeword $\hat{C}$ at Hamming distance δ from C. For a given fast fading realization **H**, the conditional pair-wise error probability in the case of QPSK symbol mapping is found as (cf. Section 7.3)

$$P_2\left(C,\hat{C}\middle|\mathbf{H}\right)=\mathrm{Q}\left(\sqrt{\sum_{n=1}^{\delta} SINR_n^{(0k)}}\right) \quad ; \quad SINR_n^{(0k)}=\frac{P_u R_n^{(0k)2}}{S_n^{(0k)}\sigma_B^2+T_n^{(0k)}\sigma_{\xi+\nu}^2} \tag{5.29}$$

where the index n runs over the set of δ differing bits. The quantities $R_n^{(0k)}$, $S_n^{(0k)}$, and $T_n^{(0k)}$ are characterized by the following

$$R_n^{(0k)} \propto \frac{1}{L}\sum_{\ell=0}^{L-1}\rho_\ell^{(0k)} \quad ; \quad S_n^{(0k)} \propto \frac{1}{L}\sum_{\ell=0}^{L-1}\rho_\ell^{(0k)2}-\left(\frac{1}{L}\sum_{\ell=0}^{L-1}\rho_\ell^{(0k)}\right)^2 \quad ; \quad T_n^{(0k)} \propto \frac{1}{L}\sum_{\ell=0}^{L-1}\left|g_\ell^{(0k)}\right|^2 \tag{5.30}$$

In the context of low channel coefficients correlation, the LLN applies to the variables $R_n^{(0k)}$, $S_n^{(0k)}$, and $T_n^{(0k)}$, and therefore $SINR_n^{(0k)}$ becomes almost invariant with respect to the fading realization **H** and nearly equal to the local mean SINR given in (5.28):

$$SINR_n^{(0k)} \approx \frac{P_u E_{\mathbf{H}}\left\{R_n^{(0k)2}\right\}}{E_{\mathbf{H}}\left\{S_n^{(0k)}\right\}\sigma_B^2+E_{\mathbf{H}}\left\{T_n^{(0k)}\right\}\sigma_{\xi+\nu}^2}=\frac{P_u\alpha_{0k}^{(0k)}}{\theta^{(0k)}\sigma_B^2+\beta^{(0k)}\sigma_{\xi+\nu}^2}=SINR^{(0k)} \tag{5.31}$$

The pair-wise error probability averaged over the fading realizations reduces then to

$$P_2\left(C,\hat{C}\right)=E_{\mathbf{H}}\left\{P_2\left(C,\hat{C}\middle|\mathbf{H}\right)\right\}=\mathrm{Q}\left(\sqrt{\delta\, SINR^{(0k)}}\right) \tag{5.32}$$

Thus, in this context of low channel coefficients correlation with channel coding, the local mean SINR at the output of the SUD detector is justified analytically as an appropriate LQM that directly maps to the bit error probability after channel decoding. However, in the context of significant correlation, the LLN does not apply to the variables $R_n^{(0k)}$, $S_n^{(0k)}$, and $T_n^{(0k)}$, and the local mean SINR cannot therefore be justified analytically as an adequate LQM.

From the above theoretical analysis of the bit error probability with and without channel coding, we conclude that in the particular context of low channel coefficients correlation, the local mean SINR at the output of the SUD module is an appropriate LQM that maps directly to the bit error probability. However, in the more general context of correlated channel coefficients, the local mean SINR cannot be justified analytically to map directly to the bit error probability. A deeper analysis of the mapping between local mean SINR and bit error

probability through link level simulations is therefore required in order to allow drawing clear conclusions about the validity and suitability of the local mean SINR measure.

5.4 Link to System Interface Simulations

5.4.1 Simulation Approach

Figure 5-3 depicts a block diagram of the link to system interface simulator used to provide the mappings between the local mean SINR and average FER.

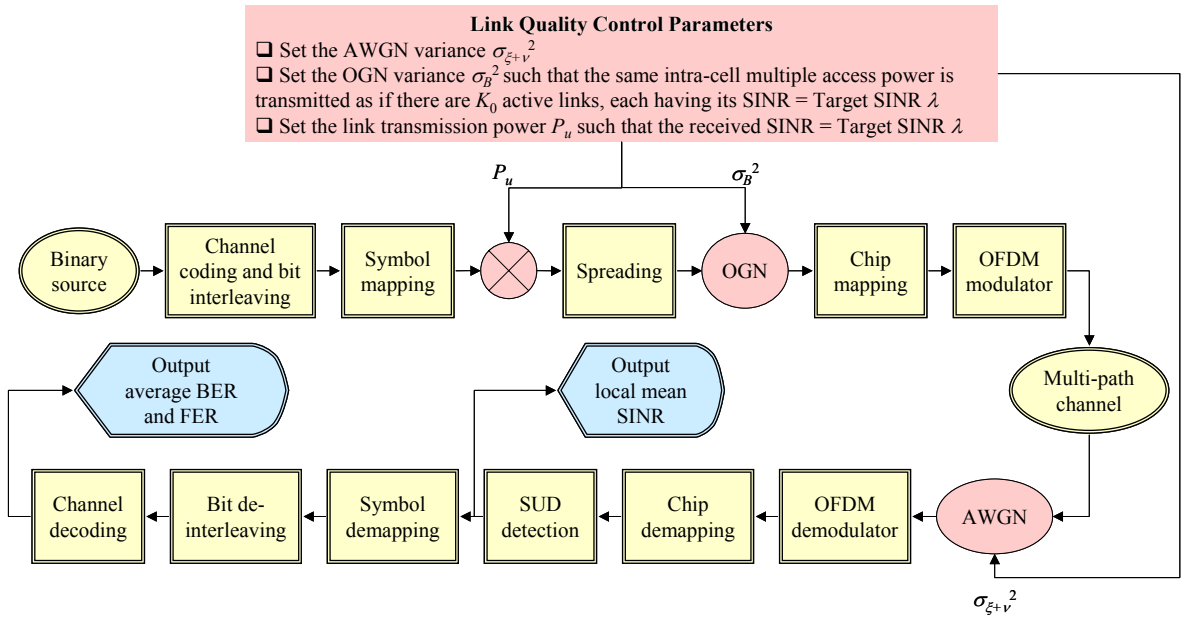

Figure 5-3: Block diagram of the downlink MC-CDMA link to system interface simulator.

As shown in Figure 5-3, the interface simulator includes all the MC-CDMA physical layer algorithms that are necessary for the transmission of the binary information of only one single link between a transmitter and a receiver through a multi-path channel. The data symbols are transmitted with power P_u, i.e., each symbol is multiplied by the square root of P_u. Moreover, the intra-cell multiple access is modeled by an OGN with variance σ_B^2, which is added after spreading the data symbols. The inter-cell interference plus noise is modeled by an AWGN with variance $\sigma_{\xi+\nu}^2$, which is added at the input of the receiver. In addition to the physical layer configuration and channel model, the simulator requires knowledge of the target local mean SINR λ, cell load K_0, and AWGN variance $\sigma_{\xi+\nu}^2$. The cell load K_0 and AWGN variance $\sigma_{\xi+\nu}^2$ characterize respectively the intra-cell interference and inter-cell interference plus noise.

The OGN variance σ_B^2 is first set such that the intra-cell multiple access power equals that of K_0 active links, each having its local mean SINR equal to the target SINR λ. From (5.16) and (5.18), the variance σ_B^2 is obtained as

$$\sigma_B^2 = \frac{1}{L-1} \sum_{j=0, j\neq k}^{K_0-1} P^{(0j)} \tag{5.33}$$

where the powers $\{P^{(0j)}\}$ are the solutions of the K_0 equations

$$SINR^{(0j)} = \frac{P^{(0j)} \alpha_{0j}^{(0j)}}{\sum_{i=0, j\neq i}^{K_0-1} P^{(0i)} \alpha_{0i}^{(0j)} + \beta^{(0j)} \sigma_{\xi+\nu}^2} = \lambda, \quad \forall j = 0 \ldots K_0 - 1 \tag{5.34}$$

The powers $\{P^{(0j)}\}$ in (5.34) are intermediate values that are used only to determine σ_B^2. On the other hand, the transmission power P_u used in the interface simulator is determined such that the received local mean SINR is equal to the target SINR λ. This can be written as

$$SINR^{(0k)} = \frac{P_u \alpha_{0k}^{(0k)}}{\theta^{(0k)} \sigma_B^2 + \beta^{(0k)} \sigma_{\xi+\nu}^2} = \lambda \tag{5.35}$$

After setting the transmission power P_u, OGN variance σ_B^2, and AWGN variance $\sigma_{\xi+\nu}^2$, the simulator transmits hundreds of frames that experience independent fading realizations. At the end of the simulation, the simulator outputs the received local mean SINR measured at the output of the SUD module. The measured SINR should satisfy the input target SINR λ. The average FER is measured by taking the ratio of total erroneous received frames to total transmitted frames. The output average FER is then associated with the measured local mean SINR and with the input scenario, which includes the couple $(K_0, \sigma_{\xi+\nu}^2)$, the physical layer configuration, and the channel model. Thus, for a given physical layer configuration and channel model, the less variation of the SINR-FER mapping there is with respect to the couple $(K_0, \sigma_{\xi+\nu}^2)$, the more relevant the local mean SINR measure becomes.

5.4.2 Numerical Results

In this section, we illustrate the influence of the couple $(K_0, \sigma_{\xi+\nu}^2)$ on the SINR-FER mapping in both cases of uncorrelated and correlated channel coefficients. The key simulation parameters are summarized in Table 5-1 [7]. Two frequency domain chip mappings are considered, namely, *Interleaved Frequency Mapping* (IFM) and *Adjacent Frequency*

Mapping (AFM). For the urban ETSI BRAN E channel model, IFM chip mapping yields a low channel coefficients correlation, while AFM mapping yields a significant correlation.

Channel coding	UMTS convolutional code (R_c = ½)
Symbol mapping	QPSK-Gray mapping
Spreading codes	Walsh-Hadamard (L = 32)
Chip mapping	¤ Interleaved Frequency Mapping (IFM) ¤ Adjacent Frequency Mapping (AFM)
OFDM modulation	¤ FFT size = 1024 samples ¤ Guard interval = 216 samples ¤ Number of available sub-carriers = 736 ¤ Sampling frequency = 57.6 MHz
Receiver type	SUD-MMSEC
Channel model	Urban ETSI BRAN E
Other parameters	¤ Frame size = 736 information bits ¤ Number of simulated frames = 1500

Table 5-1: Simulation parameters.

Figure 5-4 depicts the SINR-FER mappings obtained for both IFM (on the left) and AFM (on the right) contexts and for three values of the AWGN variance $\sigma_{\xi+\nu}^2$ = -3 dB, -7 dB, and -10 dB. The cell load K_0 is fixed to 24 codes.

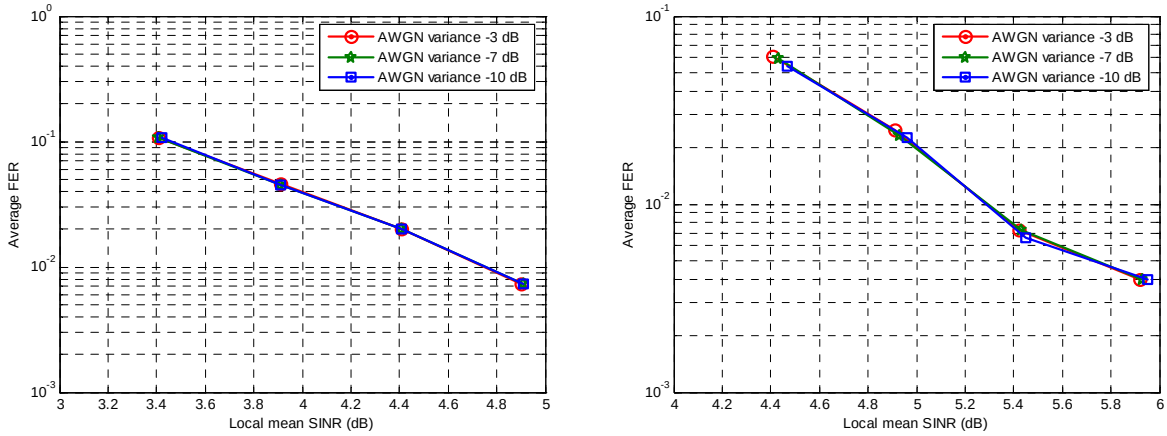

Figure 5-4: Influence of the AWGN variance on the SINR-FER mapping for low (left) and high (right) channel coefficients correlations.

As shown in Figure 5-4, the AWGN variance $\sigma_{\xi+\nu}^2$ does not influence the SINR-FER mappings in both contexts of low and significant channel coefficients correlations.

Figure 5-5 depicts the SINR-FER mappings obtained in both IFM and AFM contexts and for four values of the cell load K_0 = 8, 16, 24, and 32 codes. The AWGN variance $\sigma_{\xi+\nu}^2$ is

fixed to -7 dB. In Figure 5-5, on the left, the IFM context of low correlation is depicted, while the AFM context of significant correlation is depicted on the right.

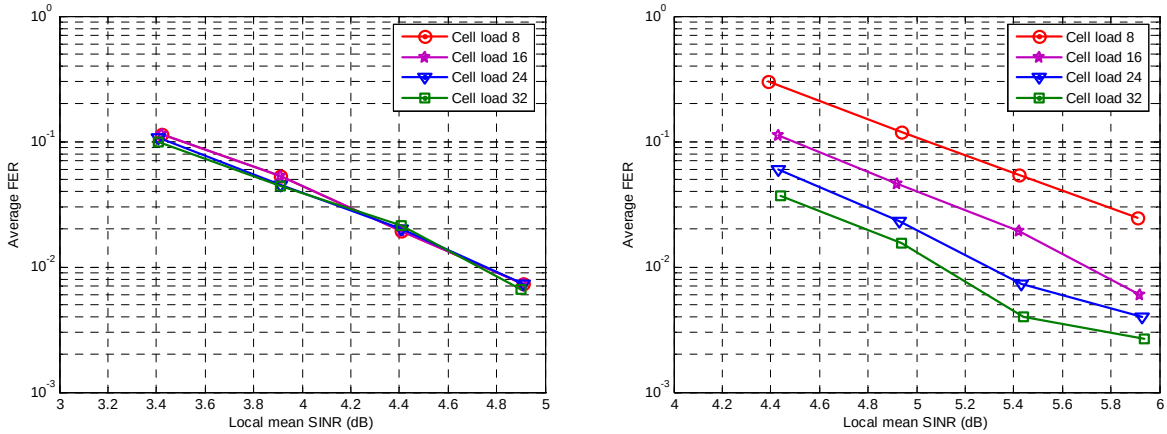

Figure 5-5: Influence of the cell load K_0 on the SINR-FER mapping for low (left) and high (right) channel coefficients correlations.

Figure 5-5 shows that the SINR-FER mapping is almost invariant with respect to the cell load K_0 in the IFM context of low correlation. This result matches well the theoretical analysis presented in Section 5.3. In the AFM context with significant correlation, different SINR-FER mappings are clearly distinguished for the different values of the cell load K_0 as expected. The difference between the mappings obtained for $K_0 = 8$ and $K_0 = 32$ appears here to be more than 1 dB, which is not negligible.

	$K_0 = 8$	$K_0 = 16$	$K_0 = 24$	$K_0 = 32$
IFM - (QPSK, UMTS convolutional code)	4.75 dB	4.75 dB	4.75 dB	4.73 dB
AFM - (QPSK, UMTS convolutional code)	6.36 dB	5.70 dB	5.30 dB	5.10 dB
AFM - (QPSK, UMTS turbo code)	5.38 dB	4.72 dB	4.36 dB	4.08 dB
AFM - (16QAM, UMTS turbo code)	9.80 dB	9.17 dB	8.81 dB	8.65 dB

Table 5-2: Influence of the cell load on the target SINR for 1% target FER.

Table 5-2 provides the target SINR values in dB required to achieve 1% target FER for $K_0 = 8, 16, 24, 32$ in four different scenarios with three different modulation and coding schemes. From Table 5-2, we can observe that for all AFM scenarios, the target SINR decreases with respect to the cell load K_0 and this decrease becomes less significant as K_0 increases. For instance, between $K_0 = 24$ and $K_0 = 32$, the target SINR decrease is only by about 0.2 dB, whereas it is by about 0.6 dB between $K_0 = 8$ and $K_0 = 16$.

The variation of the target SINR with respect to the cell load K_0 is therefore not negligible in the context of significant correlation. This is not in favor of the adequacy of the local mean SINR measure. However, we can simply bypass this problem by using different target SINR values for different values of the cell load K_0 at the system level.

In order to avoid performing several link to system interface simulations to provide all the target SINR values for all the values of K_0, we perform simulations only to determine the exact values corresponding to K_0 = 8, 16, 24 and 32. The other values are then determined by linear interpolation as illustrated in Figure 5-6. The second and third scenarios in Table 5-2 are depicted respectively on the left and right of Figure 5-6.

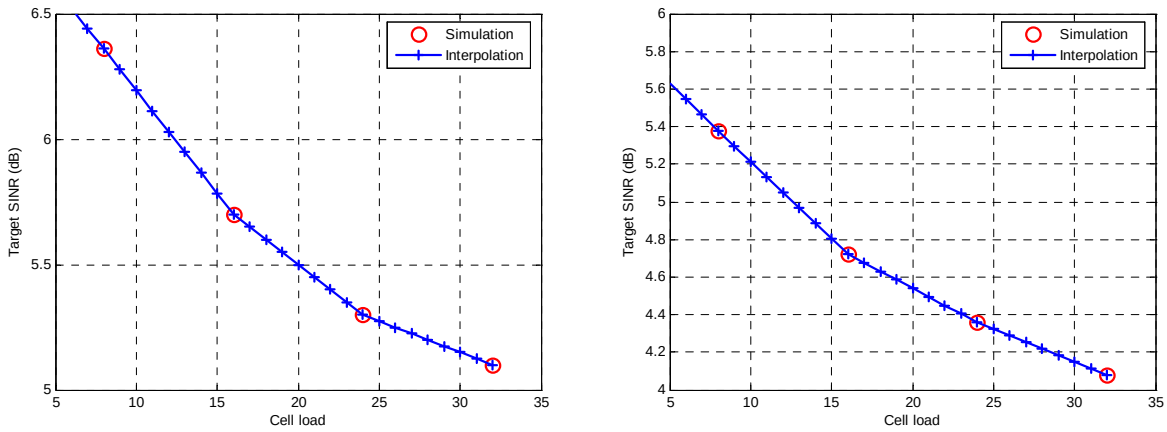

Figure 5-6: Target SINR values obtained with interpolation for AFM-MMSEC scenario with QPSK modulation and UMTS convolutional code (left) and turbo code (right).

5.5 Conclusions

In this chapter, we presented a multi-frame oriented link to system level interface for MC-CDMA cellular systems in the downlink. The aim of this interface is to determine an adequate measure that can easily and accurately be calculated at the system level and that summarizes well the radio link transmission quality. The latter is evaluated in term of the FER averaged over a large number of frames experiencing independent fading realizations.

The local mean SINR at the output of the detection module was shown to be an adequate LQM at the system level that maps directly to the average FER. The mapping between the local mean SINR and average FER is specific to the physical layer configuration and channel model. In the general case of correlated channel coefficients, the SINR-FER mapping was found to be also specific to the cell load. Different target SINR values should therefore be provided for different values of the cell load. Thanks to analytical derivation of the mutual

intra-cell and inter-cell interference powers, the local mean SINR can easily and accurately be calculated at the system level. Furthermore, thanks to intra-cell interference modeling by an OGN at the transmitter and inter-cell interference modeling by an AWGN at the input of the receiver, accurate mappings between the local mean SINR and average FER can be provided through the proposed link to system interface simulator.

The link to system interface presented in this chapter is simple and provides a degree of accuracy that is acceptable for evaluating the cellular capacity for different MC-CDMA physical layer configurations in a given environment. The evaluation of the cellular capacity through a static system level simulator using the multi-frame oriented link to system interface is the aim of the next chapter.

5.6 References

[1] D. Mottier, D. Castelain, "A Spreading Sequence Allocation Procedure for MC-CDMA Transmission Systems," *Proc. IEEE Vehicular Technology Conference (VTCF'00)*, vol.3, pp. 1270-1275, Sep. 2000.

[2] A.-M. Mourad, A. Guéguen, R. Pyndiah, "Impact of the Spreading Sequences on the Performance of Forward Link MC-CDMA Systems," *Proc. IEEE International Symposium on Spread Spectrum Techniques and Applications (ISSSTA 2004)*, pp. 683-687, Aug. 2004.

[3] J. G. Proakis, "Digital Communications," *3rd edition, McGraw-Hill*, 1995.

[4] IST European project MATRICE, "Average Value Interface for MATRICE V0 System Level Simulator," *Information note FTRD/DMR/IN/067/0.1*, Mar. 2003.

[5] P. Fan, M. Darnell, "Sequence Design for Communications Applications," *Research Studies Press Ltd.*, 1996.

[6] M. H. Fong, V. K. Bhargava, Q. Wang, "Concatenated Orthogonal/PN Spreading Sequences and Their Application to Cellular DS-CDMA Systems with Integrated Traffic," *IEEE Journal on Selected Areas in Communications (JSAC)*, vol. 14, no. 3, pp. 547-558, Apr. 1996.

[7] IST European project MATRICE, "MC-CDMA Transmission Techniques for Integrated Broadband Cellular Systems," *website: www.ist-matrice.org*.

[8] J. Gozalvez, J. Dunlop, "Link Level Modeling Techniques for Analyzing the Configuration of Link Adaptation Algorithms in Mobile Radio Networks," *Proc. European Wireless Conference*, Feb. 2004.

[9] H. Holma, "A Study of UMTS Terrestrial Radio Access Performance," *Ph.D. thesis*, *Helsinki University of Technology,* Oct. 2003.

[10] IST European project FITNESS, "System-Level Simulation Methodology Defined," *Deliverable 4.1*, Oct. 2002.

[11] IST European project 4MORE, "4G MC-CDMA multiple antenna system On chip for Radio Enhancements," *website: www.ist-4more.org*.

[12] J. Zander, S. Kim, "Radio Resource Management for Wireless Networks," *Artech House Publishers*, 2001.

Chapter 6
Downlink Cellular Capacity for MC-CDMA Systems

The aim of this chapter is to evaluate the capacity for different MC-CDMA physical layer algorithms and configurations in the downlink of a multi-cellular environment. The capacity is defined as the maximum number of users that can be served simultaneously by the central base station with fulfilled transmission quality requirements. It is evaluated through Monte-Carlo static system level simulator using the multi-frame oriented link to system interface developed previously in Chapter 5.

6.1 System Model

The deployment model is assumed to follow an hexagonal regular macro-cellular layout made up of one central cell surrounded by N_t tiers of neighboring cells. The number of cells in the system Q is related to the number of tiers N_t as

$$Q = 1 + 3N_t\left(N_t + 1\right) \tag{6.1}$$

Each cell has a centrally located BS equipped with a directional or an omni-directional antenna depending on whether sectoring is employed or not. With sectoring, the number of sectors per cell N_s is equal to 3, and the directional antenna pattern in the horizontal plane used has the form [1]

$$A(\theta)[dB] = A_{max}[dB] - \min\left(12\left(\frac{\theta-\theta_m}{\theta_{3\text{dB}}}\right)^2, FBR[dB]\right) \quad ; \quad |\theta| \le 180° \tag{6.2}$$

where A_{max} = 7 dB is the maximum antenna gain, $\theta_{3\text{dB}}$ = 70° is the 3 dB beamwidth, $\theta_m \in$ {0°, 120°, -120°} is the direction of A_{max}, and FBR = 20 dB is the front-to-back ratio. Figure 6-1 shows the radiation patterns of the directional antennas used in sectoring scenario.

Without sectoring, an omni-directional antenna in the horizontal plane is used with a constant gain equal to

$$A = \frac{1}{360}\int_{-180}^{180} A(\theta)d\theta \tag{6.3}$$

where $A(\theta)$ is the directional antenna gain in (6.2) defined in the linear scale.

By writing (6.3), we ensure that both omni-directional and directional antennas have the same overall gain when summing over all directions.

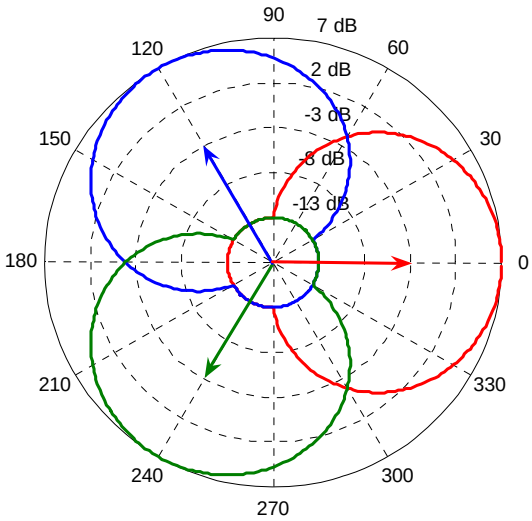

Figure 6-1: Radiation patterns of the antennas used for sectoring.

For each sector, each BS has a maximum number of M spreading codes and a maximum output power P_{max} available for allocation to the traffic channels. For the sake of simplicity and in order to avoid border effects, the results are collected only from one sector of the central BS although the whole system is simulated, while the Q-1 surrounding BS are assumed to transmit at the same fixed power $P_o \leq P_{max}$.

The users are assumed to be uniformly distributed within the disk delimiting the cellular layout as shown in Figure 6-2. A user is connected to only one BS, i.e., macro-diversity handover is not considered. All users use the same physical layer configuration and require the same target transmission quality. The connectivity between users and BS follows the minimum large-scale propagation loss criterion, i.e., a user is connected to the BS to which the large-scale propagation loss is minimum. The large-scale propagation loss includes the power loss due to the BS to user distance and the shadowing loss. It is of the form (cf. (2.8))

$$LM[dB] = C_0[dB] + 10\mu \log_{10}(d) + SH[dB] \tag{6.4}$$

where C_0 is a constant determined from measurements, μ is the path loss exponent, d is the BS to user distance, and SH is the log-normal shadowing variable of standard deviation σ_{SH}. More details on the large-scale propagation loss model are provided in Chapter 2.

In a multi-cellular environment, the shadowing variable SH is generally decomposed into two independent log-normal variables SH_u and SH_l, which are specific respectively to the local environment of the user and to the environment between the user and BS [2]:

$$SH[dB] = \sqrt{\rho} SH_u[dB] + \sqrt{1-\rho} SH_l[dB] \tag{6.5}$$

where ρ is called the shadowing correlation coefficient and it is typically set to 0.5.

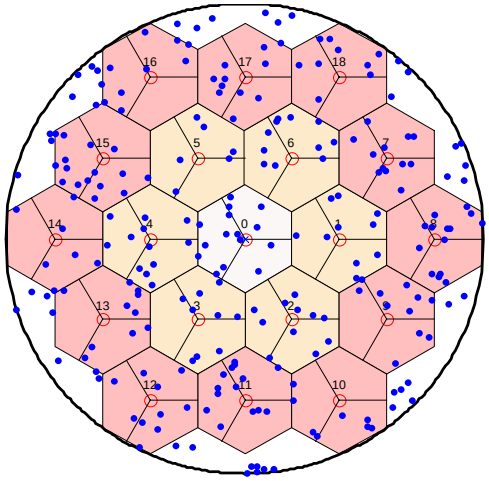

Figure 6-2: Cellular layout with 19 sectored cells and 250 users.

6.2 Analytical Approach for Capacity Evaluation

In this section, we present the analytical approach used for calculating the cellular capacity for a given MC-CDMA physical layer configuration. We consider the problem of satisfying the target FER requirements of the users connected to the central BS (BS_0). The target FER requirements are converted into target SINR requirements through the SINR-FER mappings provided by the multi-frame oriented link to system level interface developed in Chapter 5. The problem of satisfying the target SINR requirements under the constraint of limited BS power can therefore be formulated as

$$\begin{aligned} SINR^{(0k)} &= \lambda_\phi \quad ; \quad \forall k = 0 \ldots K_0 - 1 \le M \\ P^{(0k)} &> 0 \quad ; \quad P^{(0)} = \sum_{k=0}^{K_0-1} P^{(0k)} \le P_{max} \end{aligned} \tag{6.6}$$

where λ_ϕ denotes the target local mean SINR that is specific to the scenario ϕ of physical layer configuration and multi-path channel model, and $SINR^{(0k)}$ is the local mean SINR at the output of the SUD module for the k-th link L_{0k} connected to BS_0.

In the general case of N_s sectors per cell, the number of BS in the system can equivalently be considered equal to N_sQ, where the q-th BS denoted by BS_q refers now to the q-th sector. From (5.34) and by taking into account the large-scale propagation losses and antenna gains, the local mean SINR for link L_{0k} can be expressed as

$$SINR^{(0k)} = \frac{P^{(0k)} A^{(0k)} G^{(0k)} \alpha_{0k}^{(0k)}}{A^{(0k)} G^{(0k)} \sum_{j=0, j\neq k}^{K_0-1} P^{(0j)} \alpha_{0j}^{(0k)} + \beta^{(0k)} \left(\frac{1}{L} \sum_{m=1}^{N_sQ-1} A^{(mk)} G^{(mk)} P_o + P_\nu \right)} \tag{6.7}$$

where $A^{(mk)}$ denotes the antenna gain of BS_m in the direction of user k connected to BS_0, $G^{(mk)}$ is the large-scale propagation loss between BS_m and user k, P_ν is the thermal noise power, $\{\alpha_{0j}^{(0k)}\}$ are the mutual intra-cell interference factors given in (5.5), and $\beta^{(0k)}$ is the inter-cell interference plus noise factor given in (5.22).

Using the SINR expression given in (6.7), the problem of satisfying the SINR requirements formulated in (6.6) can be rewritten as the following power allocation problem for BS_0

$$\begin{aligned} \mathbf{p} &= \lambda_\phi \left(\mathbf{\Lambda p} + \mathbf{f} P_o + \mathbf{b} P_\nu \right) \\ \mathbf{p} &> \mathbf{0} \quad ; \quad P^{(0)} = \mathbf{1}^T \mathbf{p} \le P_{max} \end{aligned} \tag{6.8}$$

where $\mathbf{p}$ denotes the column vector of K_0 powers $\{P^{(0k)}\}$, $\mathbf{\Lambda}$ is a matrix of size $K_0 \times K_0$ representing the intra-cell interference, $\mathbf{f}$ is a column vector of length K_0 representing the inter-cell interference, $\mathbf{b}$ is a column vector of length K_0 representing the thermal noise, and $\mathbf{1}$ is the all one vector. The quantities $\mathbf{\Lambda}$, $\mathbf{f}$, and $\mathbf{b}$ are characterized by

$$\Lambda[k,j] = \frac{\alpha_{0j}^{(0k)}}{\alpha_{0k}^{(0k)}} \left(1 - \delta_{kj}\right) \quad ; \quad f[k] = \frac{1}{L} \frac{\beta^{(0k)}}{\alpha_{0k}^{(0k)}} \sum_{m=1}^{N_sQ-1} \frac{A^{(mk)} G^{(mk)}}{A^{(0k)} G^{(0k)}} \quad ; \quad b[k] = \frac{\beta^{(0k)}}{A^{(0k)} G^{(0k)} \alpha_{0k}^{(0k)}} \tag{6.9}$$

The matrix $\mathbf{\Lambda}$ is not strictly positive since its diagonal is null but it is regular, i.e., its square is strictly positive, and so the Perron-Frobenius theory applies [3][4]. It is well known from Perron-Frobenius theory for non negative matrices that the linear form $\mathbf{p} = \mathbf{Ap} + \mathbf{b}$ has a positive solution $\mathbf{p}^* = (\mathbf{I}\text{-}\mathbf{A})^{-1}\mathbf{b} > \mathbf{0}$ if and only if the maximum eigenvalue of matrix $\mathbf{A}$ is strictly less than 1. Thus, the necessary and sufficient condition to obtain a positive and finite solution to (6.8) is that the maximum eigenvalue μ^* of $\mathbf{\Lambda}$ is less than $1/\lambda_\phi$. This condition is usually referred to as the *pole condition*, and the maximum cell load K_0 satisfying the pole condition is referred to as the *pole capacity* K_{pole} [5][6].

Once the pole condition is satisfied, the positive solution to (6.8) can then be obtained as

$$\mathbf{p}^* = \lambda_\phi \left(\mathbf{x} P_o + \mathbf{y} P_v \right), \quad \mathbf{x} = \left(\mathbf{I} - \lambda_\phi \mathbf{\Lambda} \right)^{-1} \mathbf{f}, \quad \mathbf{y} = \left(\mathbf{I} - \lambda_\phi \mathbf{\Lambda} \right)^{-1} \mathbf{b} \tag{6.10}$$

By taking into account the constraint of limited BS output power, the *constrained capacity* K_{const} is then determined as

$$K_{const} = \arg\max_{K_0} \left\{ \Pr\left(\mu^* > \frac{1}{\lambda_\phi} \bigcup P^{(0)} > P_{\max} \right) \le \varepsilon \right\} \tag{6.11}$$

where ε denotes the maximum tolerated outage threshold and it is typically set to 5%.

The constrained capacity K_{const} also known as the *outage capacity* can straightforwardly be converted into a constrained cellular throughput R_{const} as

$$R_{const} = K_{const} \left(1 - FER_\phi \right) R_\phi \tag{6.12}$$

where R_ϕ denotes the single user information bit rate corresponding to the physical layer configuration considered in the scenario ϕ and FER_ϕ is the residual FER corresponding to the target local mean SINR λ_ϕ.

6.2.1 A Novel Capacity Indicator at the Link Level

Herer, we introduce a novel indicator that enables an analysis at the link level of the capacity performances of MC-CDMA physical layer algorithms and configurations. The general case of different mutual intra-cell interference factors is considered.

In the particular case where the mutual intra-cell interference factors $\{\alpha_{0j}^{(0k)}\}$ are almost the same and equal to α, the output power $P^{(0)} = \mathbf{1}^T \mathbf{p}^*$ required to fulfill the target local mean SINR requirements can be factorized as

$$P^{(0)} = \underbrace{\frac{\lambda_\phi \beta K_0}{1 - \lambda_\phi (K_0 - 1)\alpha}}_{C_\phi^{(0)}} \underbrace{\left(\frac{1}{K_0} \sum_{k=0}^{K_0 - 1} \left(\frac{P_o}{L} \sum_{m=1}^{N_s Q - 1} \frac{A^{(mk)} G^{(mk)}}{A^{(0k)} G^{(0k)}} + \frac{P_v}{A^{(0k)} G^{(0k)}} \right) \right)}_{T^{(0)}} \tag{6.13}$$

where β denotes the inter-cell interference plus noise factor $\beta^{(0k)}$ but without the superscript $0k$ specific to link L_{0k} since all links are assumed to use the same equalization technique.

It is important to point out that the component $T^{(0)}$ in (6.13) is independent of the scenario ϕ of physical layer configuration and multi-path channel model. It summarizes all the system level parameters that affect the transmission power $P^{(0)}$ and it reflects the average level of inter-cell interference plus noise. By applying the *Law of Large Numbers* (LLN), $T^{(0)}$ can then

be considered to be almost independent of the cell load K_0. Only the component $C_\phi^{(0)}$ remains therefore specific to the scenario ϕ and to the cell load K_0. The component $C_\phi^{(0)}$ can simply be evaluated at the link level since it is only function of λ_ϕ, α, and β, which are outputs of the multi-frame oriented link to system level interface. For a given value of $T^{(0)}$ and of cell load K_0, a lower value of $C_\phi^{(0)}$ means that a lower power $P^{(0)}$ is required to fulfill the target SINR requirements. Thus, equivalently for a given value of $T^{(0)}$ and of power $P^{(0)}$, a lower value of $C_\phi^{(0)}$ allows to accommodate a higher cell load K_0. $C_\phi^{(0)}$ can therefore be considered as an indicator of the capacity performances of the physical layer configuration ϕ. Based on $C_\phi^{(0)}$, we can conclude which algorithms and configurations provide the highest cellular capacity without performing system level simulations. However, we cannot know at which level of inter-cell interference plus noise and for which transmission power.

By analogy to (6.13), we extend the expression of the link level capacity indicator $C_\phi^{(0)}$ to the general case of different mutual intra-cell interference factors $\{\alpha_{0j}^{(0k)}\}$ as follows

$$C_\phi^{(0)} = \frac{\lambda_\phi \beta K_0}{1 - \lambda_\phi \mu^*} \tag{6.14}$$

where μ^* is the maximum eigenvalue of the intra-cell interference matrix $\mathbf{\Lambda}$. By using (6.14), we can easily determine the maximum cell load K_{max} that keeps the link level capacity indicator $C_\phi^{(0)}$ below a certain threshold. The pole capacity K_{pole} can simply be determined by setting the threshold equal to infinity, i.e., $C_\phi^{(0)} = +\infty$.

The interest of the novel capacity indicator introduced here is that it allows to compare the cellular capacity performances for the physical layer algorithms and configurations from the only knowledge of the link level quantities λ_ϕ, μ^*, and β, thus without requiring system level simulations. This makes it an efficient tool at the link level for optimizing the physical layer algorithms and identifying the most suitable configurations for a given environment.

6.2.2 Particular Case of MMSEC Equalization

In addition to the channel coefficients $\{h_\ell^{(0k)}\}$, MMSEC equalization coefficients are also functions of the useful and interference received powers. The ℓ-th equalization coefficient for the ℓ-th channel coefficient $h_\ell^{(0k)}$ is obtained from (4.23) as

$$g_\ell^{(0k)} = \sqrt{\frac{P^{(0k)}}{A^{(0k)}G^{(0k)}}}\,\frac{h_\ell^{(0k)*}}{\frac{P^{(0)}}{L}\left|h_\ell^{(0k)}\right|^2 + \underbrace{\left(\frac{P_o}{L}\sum_{m=1}^{N_s Q-1}\frac{A^{(mk)}G^{(mk)}}{A^{(0k)}G^{(0k)}} + \frac{P_\nu}{A^{(0k)}G^{(0k)}}\right)}_{T^{(0k)}}} \tag{6.15}$$

The mutual intra-cell interference factors $\{\alpha_{0j}^{(0k)}\}$ and the inter-cell interference plus noise factors $\{\beta^{(0k)}\}$, which are derived from the correlations of the equalized channel coefficients $\{h_\ell^{(0k)}g_\ell^{(0k)}\}$ and energy of the equalization coefficients $\{g_\ell^{(0k)}\}$ (cf. (5.5) and (5.22)), become therefore functions of the power allocation vector $\mathbf{p}$. The power allocation problem in (6.8) becomes then nonlinear as

$$\mathbf{p} = \lambda_\phi\left(\mathbf{\Lambda}(\mathbf{p})\mathbf{p} + \mathbf{f}(\mathbf{p})P_o + \mathbf{b}(\mathbf{p})P_\nu\right) \tag{6.16}$$

In order to find a solution to (6.16), we consider the following recursive algorithm

$$\mathbf{p}^{(r+1)} = \lambda_\phi\left(\mathbf{x}\left(\mathbf{p}^{(r)}\right)P_o + \mathbf{y}\left(\mathbf{p}^{(r)}\right)P_\nu\right) \quad ; \quad \forall\, r = 0 \ldots N_r - 1 \tag{6.17}$$

where r denotes the r-th recursion and N_r is the maximum number of recursions. When (6.16) has a solution, the algorithm in (6.17) converges to this solution in a few recursions ($N_r \leq 5$) for any positive and non null finite initial vector $\mathbf{p}^{(0)}$.

6.2.2.1 Approximation for Computational Costs Reduction

In order to find the solution $\mathbf{p}^*$ to (6.16), the mutual intra-cell interference factors $\{\alpha_{0j}^{(0k)}\}$ should therefore be evaluated online for each recursion and for each snapshot in the system level simulator. This highly increases the computational costs since the calculation of these factors require the computation of K_0 equalized channel coefficients correlations due to the specificity of these correlations to the links $\{L_{0k}\}$ induced by (6.15). In order to reduce the computational costs, we make the following approximation

$$g_\ell^{(0k)} \approx \sqrt{\frac{P^{(0k)}}{A^{(0k)}G^{(0k)}}}\,v_\ell \quad ; \quad v_\ell = \frac{h_\ell^{(0k)*}}{\frac{P^{(0)}}{L}\left|h_\ell^{(0k)}\right|^2 + T^{(0)}} \tag{6.18}$$

where $T^{(0)}$ replaces the term $T^{(0k)}$ in the denominator in (6.15) by its average value taken over the K_0 links and it has already been used in (6.13). Thus, by using (6.18) instead of (6.15), only one correlation term between the equalized channel coefficients $\{h_\ell^{(0k)}v_\ell\}$ is needed in order to calculate the mutual intra-cell interference factors $\{\alpha_{0j}^{(0k)}\}$.

Figure 6-3 depicts the *Cumulative Distribution Function* (CDF) of BS_0 power $P^{(0)}$ for IFM (on the left) and AFM (on the right) chip mappings. We consider the modulation and coding scheme MCS1 described in Table 6-2. The target SINR values required to achieve 1% target FER are taken from Table 6-3. On the other hand, the cellular layout is considered with 19 sectored cells and a total number of 1368 users, i.e., an average of 24 users per sector. The transmission power P_o of inter-cell interfering BS is taken equal to 5 dBW.

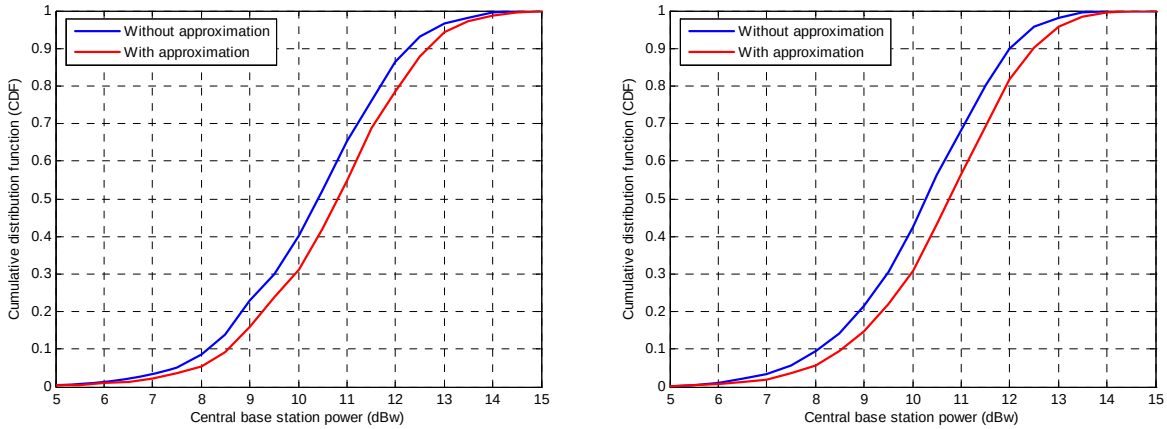

Figure 6-3: Validity of the MMSEC approximation at the system level assuming IFM (left) and AFM (right) chip mappings.

As shown in Figure 5-1, the approximation made in (6.18) increases the power $P^{(0)}$ only by less than 0.5 dB for both IFM and AFM chip mappings. The power increase of 0.5 dB was also found to be still valid for MCS2 and MCS3 given in Table 6-2. Such a small power increase may lead to a small underestimation of the cellular capacity, which can simply be corrected by increasing the maximum transmission power P_{max} by 0.5 dB. The MMSEC approximation in (6.18) can therefore be used to provide accurate results with significant reduction of the computational costs in system level simulations.

6.2.2.2 Evaluating the Capacity Indicator at the Link Level

Since the mutual intra-cell interference factors $\{\alpha_{0j}^{(0k)}\}$ are here specific to each snapshot of the system (cf. (6.18)), the capacity indicator $C_\phi^{(0)}$ in turn becomes then specific to each snapshot. The exact value of $C_\phi^{(0)}$ cannot therefore be evaluated at the link level since μ^* and β in (6.14) require here evaluation at the system level. However, we can still evaluate an approximation of $C_\phi^{(0)}$ at the link level by using the values of μ^* and β obtained from the use of the simple link level MMSEC equalization coefficient given in (4.24). The value of $C_\phi^{(0)}$ obtained at the link level will then be specific to the AWGN variance, which reflects the level

of inter-cell interference plus noise at the link level. To obtain meaningful results of $C_{\phi}^{(0)}$, we should consider here different realistic values of the AWGN variance that correspond to the different levels of inter-cell interference plus noise at the system level. The link level capacity indicator shows here its limits and only system level simulations can provide accurate and conclusive results on the performance of MMSEC-based configurations.

6.3 Monte-Carlo System Level Simulator

System level simulations are classified as dynamic or static depending on whether time-evolution is taken into account or not [7]. Static simulations are commonly used in both capacity analyses and radio planning tools due to their lower complexity and shorter simulation time. In this thesis, a static system simulation methodology is developed for evaluating the cellular capacity. The static simulation methodology is based upon a Monte-Carlo technique, i.e., a statistical technique that considers many independent time instants. For each time instant, one possible realization of the system defined as a *snapshot* is generated. By using a large number of snapshots, statistical results can be provided by the Monte-Carlo system simulator with a high level of accuracy.

Figure 6-4 depicts a sketch diagram of the Monte-Carlo system level simulator and its functioning is described in the following.

Initial Settings

Here, all the parameters that are needed for the whole simulation process are initialized or calculated. Starting by the cellular layout, cell radius, number of tiers, number of sectors, and minimum distance from BS are first initialized. The parameters of BS antenna pattern and large-scale propagation loss are then provided. The thermal noise power density and receiver noise factor are then given and the thermal noise power P_{ν} is then deduced. Next, the MC-CDMA physical layer configuration and multi-path channel model are fixed. At last, we set the simulation control parameters including the required target FER, maximum number of codes M, maximum power P_{max} of the sector under consideration, transmission power P_o of the interfering sectors, outage threshold ε, and maximum number of snapshots.

After initializing the above parameters, the target FER is then converted into a target local mean SINR λ_{ϕ} which is specific to the scenario ϕ of MC-CDMA physical layer configuration and channel model. For EGC and MRC equalizations, the mutual intra-cell interference factors $\{\alpha_{0j}^{(0k)}\}$ and inter-cell interference plus noise factor β are calculated at this point since

they are independent of the system snapshot, whereas for MMSEC equalization, these factors are calculated for each system snapshot within the simulation.

The simulation starts then with a given total number of users in the system.

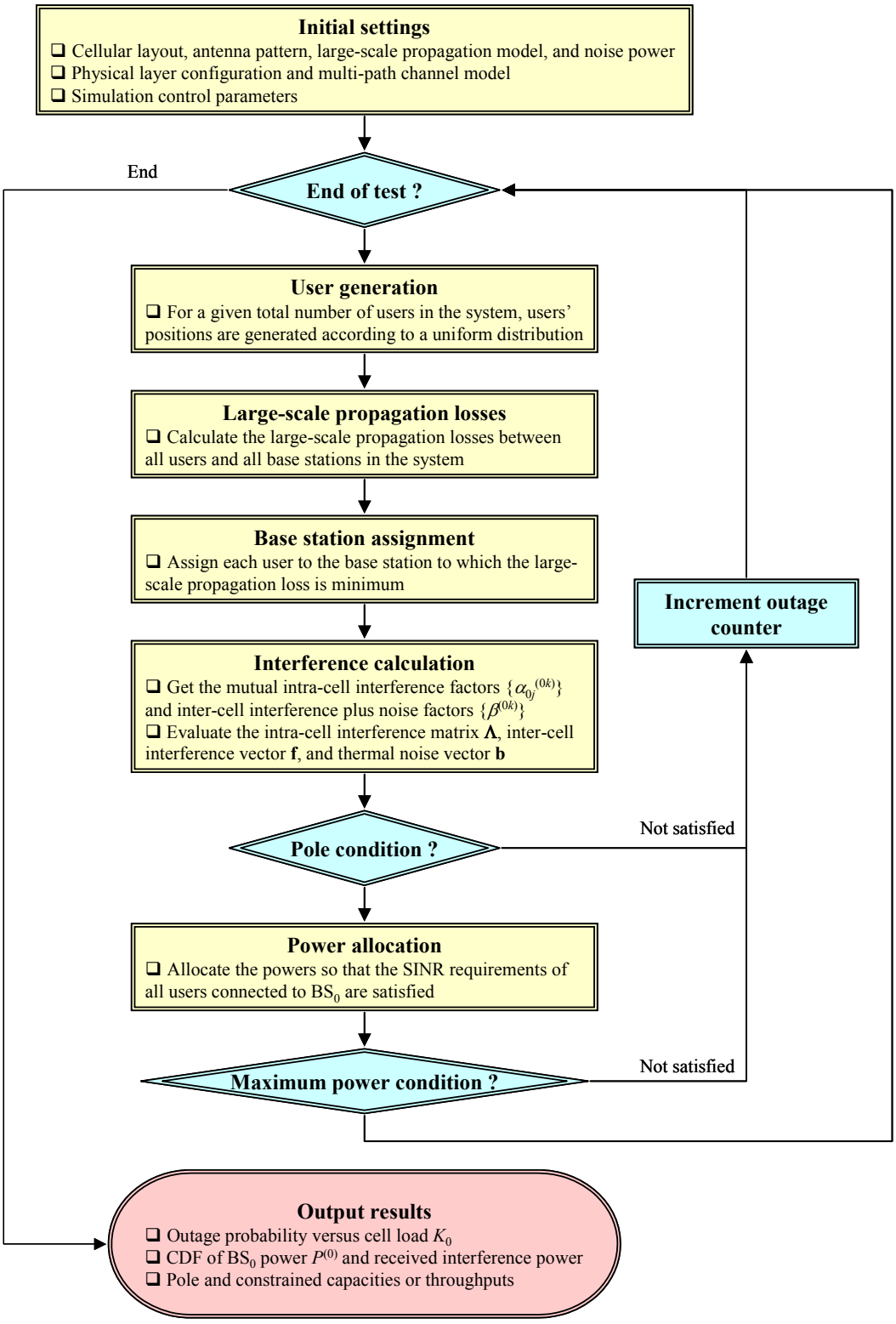

Figure 6-4: Sketch diagram of the Monte-Carlo system level simulator.

User Generation

In this block, the users are randomly positioned in the system according to a uniform distribution in the disk delimiting the hexagonal cellular layout.

Large-Scale Propagation Losses

The large-scale propagation losses including the path and shadowing losses are calculated here for all possible links between all users and base stations.

Base Station Assignment

Each user is assigned to the BS to which it has the minimum large-scale propagation loss. Each user is assigned to only one BS, i.e., macro-diversity handover is not considered.

Interference Calculation and Outage Conditions

Here, in the cases of EGC and MRC equalizations, the intra-cell interference matrix $\mathbf{\Lambda}$ is first formed from the mutual intra-cell interference factors $\{\alpha_{0j}^{(0k)}\}$ (cf. (5.5)) for the cell load K_0 obtained after base station assignment. The inter-cell interference and thermal noise vectors $\mathbf{f}$ and $\mathbf{b}$ are then calculated using the inter-cell interference plus noise factor β (cf. (5.22)). If the maximum eigenvalue μ^* of $\mathbf{\Lambda}$ is less than $1/\lambda_\phi$, the power allocation vector $\mathbf{p}^*$ is then determined from (6.10), otherwise an outage occurs and the counter of outage events referred to as the outage counter is incremented. This is the pole condition test.

In the case of MMSEC equalization, an initial vector $\mathbf{p}^{(0)}$ is fixed and a simulation loop of N_r recursions is started. At recursion $r \geq 1$, the factors $\{\alpha_{0j}^{(0k)}\}$ are first calculated using the approximation made in Section 6.2.2.1 and the intra-cell interference matrix $\mathbf{\Lambda}^{(r\text{-}1)}$ is formed. The inter-cell interference plus noise factors $\{\beta^{(0k)}\}$ are then calculated and vectors $\mathbf{f}^{(r\text{-}1)}$ and $\mathbf{b}^{(r\text{-}1)}$ are deduced. If the pole condition is not satisfied by matrix $\mathbf{\Lambda}^{(r\text{-}1)}$, the simulation loop is then stopped since a positive vector $\mathbf{p}^{(r)}$ cannot be obtained from (6.17), otherwise the power vector $\mathbf{p}^{(r)}$ is calculated from (6.17) and the simulation loop continues with a new recursion. At the end of the simulation loop, if the pole condition was not violated at any recursion, the power vector $\mathbf{p}^*$ is calculated and total power $P^{(0)}$ deduced, otherwise an outage is pointed out and the outage counter is incremented.

When the power vector $\mathbf{p}^*$ exists, the total power $P^{(0)} = \mathbf{1}^{\mathrm{T}}\mathbf{p}^*$ is calculated and compared to the maximum power P_{max}. If $P^{(0)}$ is greater than P_{max}, the constraint of maximum power P_{max} is violated and the outage counter is incremented, otherwise we move to a new snapshot.

End of Simulation

Simulation ends when the maximum number of snapshots is reached and then statistical results are computed. Typical output results are the outage probability versus the cell load K_0, the pole and outage capacities, the cellular throughput, the CDF of the power $P^{(0)}$, the CDF of the inter-cell interference received power, etc. The outage probability is specific to each value of the cell load K_0 and it is calculated as the ratio between the outage counter and the number of snapshots, which both are specific to the cell load K_0. The outage capacity is then obtained as the maximum cell load for which the outage probability is less than the outage threshold ε.

To sum up, the power $P^{(0)}$ is a random variable that varies with respect to the snapshot of the system. In system level simulations, we calculate the CDF of $P^{(0)}$ for all possible values of the cell load K_0 over a large number of snapshots. The cellular capacity is then determined as the maximum value of K_0 for which the CDF at the maximum power P_{max} is less than 1-ε. On the other hand, with the link level capacity indicator introduced in Section 6.2.1, we calculate the capacity indicator for all values of K_0, and then we determine the cellular capacity as the maximum value of K_0 for which the capacity indicator is less than a given threshold. Figure 6-5 illustrates the link (on the left) and system level (on the right) approaches used to determine the cellular capacity.

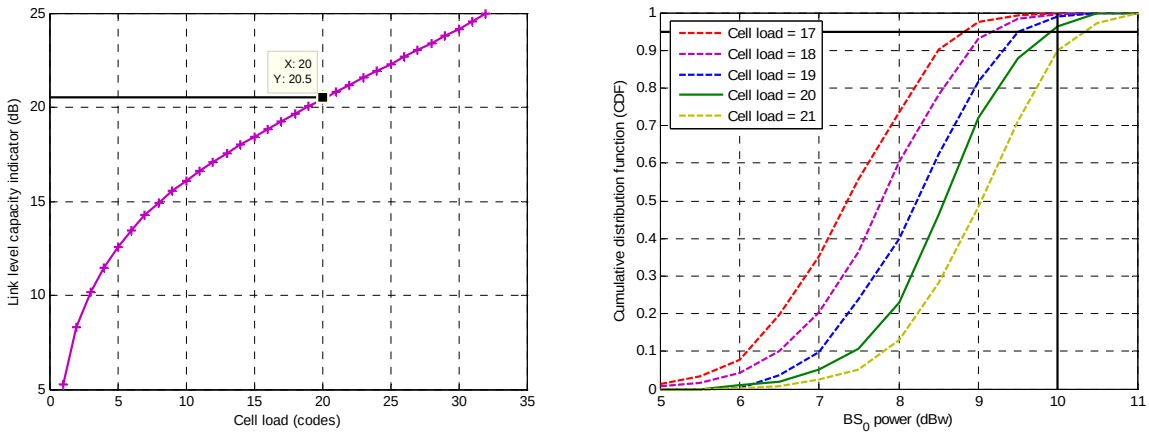

Figure 6-5: Link (left) and system (right) level approaches for capacity evaluation.

6.4 Numerical Results

In this section, we evaluate the downlink cellular capacity for different MC-CDMA physical layer configurations in an urban macro-cellular environment. Here, we put the emphasis on the trade-off between diversity and *Multiple Access Interference* (MAI), which is a major issue in the design of MC-CDMA systems.

6.4.1 MC-CDMA Physical Layer Configurations

The key simulation parameters of MC-CDMA physical layer are given in Table 6-1 [8].

Carrier frequency	5 GHz
OFDM parameters	¤ FFT size = 1024 ¤ Sampling frequency = 57.6 MHz ¤ Number of data sub-carriers = 736 ¤ Occupied bandwidth = 41.44 MHz ¤ OFDM symbol duration = 21.5 µs ¤ Guard interval = 3.75 µs ¤ Guard interval in samples = 216
CDMA parameters	¤ Walsh-Hadamard codes (L = 32) ¤ Spreading in frequency (L_f = 32,L_t = 1) ¤ Natural order codes assignment
Frame structure	¤ Number of OFDM symbols = 32 ¤ Duration = 0.689 ms

Table 6-1: MC-CDMA physical layer simulation parameters.

The *Modulation and Coding Schemes* (MCS) and their corresponding binary information rates are listed in Table 6-2.

	Modulation	Channel coding	Bit rate R_ϕ
MCS1	QPSK	UMTS convolutional (½)	1.07 Mbit/s
MCS2	QPSK	UMTS turbo (½)	1.07 Mbit/s
MCS3	16QAM	UMTS turbo (½)	2.14 Mbit/s

Table 6-2: Modulation and coding schemes.

Two frequency domain chip mappings are considered, namely, *Interleaved Frequency Mapping* (IFM) and *Adjacent Frequency Mapping* (AFM). The system achieves a higher diversity with IFM than with AFM but to the detriment of higher MAI. This is because IFM transmits the chips of a spread data symbol on lowly correlated sub-carriers, whereas AFM transmits the chips on highly correlated sub-carriers.

We also consider the urban ETSI BRAN E channel model (cf. Appendix A.1) and SUD technique with either EGC, MRC, or MMSEC equalization (cf. Section 4.2.2.1).

6.4.2 Capacity Analysis at the Link Level

Here, we use the link level capacity indicator $C_\phi^{(0)}$ (cf. (6.14)) for quantifying the impact of different MC-CDMA physical layer configurations on the cellular capacity.

We first compare six configurations resulting from the combination of either IFM or AFM chip mapping with either EGC, MRC, or MMSEC equalization. All configurations use the

same modulation and coding scheme MCS1 (cf. Table 6-2). Table 6-3 summarizes the target local mean SINR values in dB required to achieve 1% target FER for the four cell loads K_0 = 8, 16, 24, and 32, and for all the six configurations. For each configuration, the four target SINR values given in Table 6-3 are used to determine through linear interpolation the target SINR value corresponding to a cell load K_0 between 8 and 32 codes.

	$K_0 = 8$	$K_0 = 16$	$K_0 = 24$	$K_0 = 32$
IFM-MRC	4.26	4.26	4.26	4.26
IFM-EGC	4.31	4.31	4.31	4.31
IFM-MMSEC	4.75	4.75	4.75	4.75
AFM-MRC	7.81	7.16	6.11	5.51
AFM-EGC	6.52	6.33	5.96	5.70
AFM-MMSEC	6.36	5.70	5.30	5.10

Table 6-3: Target SINR in dB required to achieve 1% target FER for IFM and AFM mappings with EGC, MRC, and MMSEC equalizations.

Figure 6-6 on the left depicts the link level capacity indicator $C_\phi^{(0)}$ versus the cell load K_0 for all the six configurations. On the right, we show the capacity values obtained for the link level capacity indicator thresholds: $C_\phi^{(0)} = \infty$, 24 dB, 22 dB, 20 dB, and 18 dB. Note that $C_\phi^{(0)} = \infty$ gives the pole capacity. For MMSEC equalization, as discussed in Section 6.2.2.2, we use the link level equalization coefficients with an AWGN variance of -7 dB.

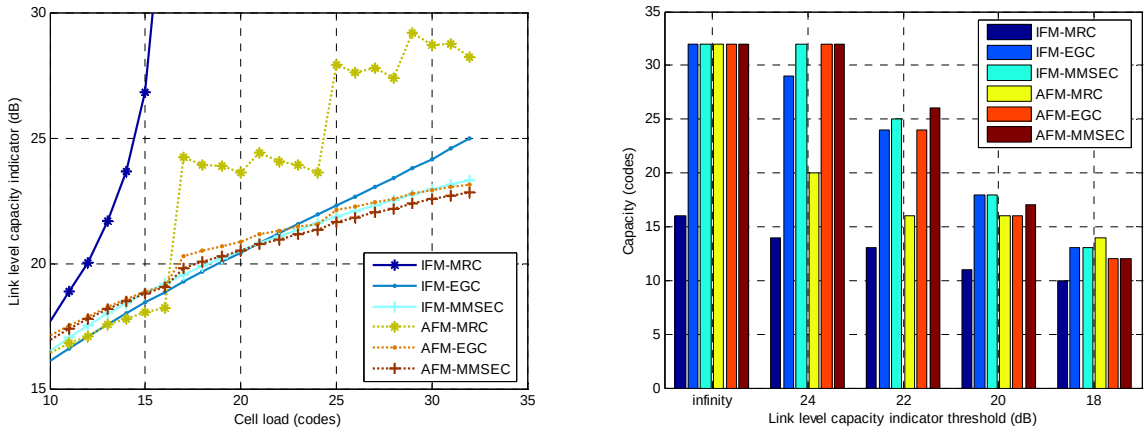

Figure 6-6: Cell load in codes versus the link level capacity indicator in dB for IFM and AFM chip mappings with EGC, MRC, and MMSEC equalizations.

From Figure 6-6, we can first observe that the pole capacity of 32 codes is reached for all the six configurations except for IFM-MRC where it is equal to 16 codes. Moreover, we can see that AFM-MMSEC, IFM-MMSEC, and AFM-EGC have close performances and

outperform all other configurations in the region where the capacity is more than about 20 codes. In this capacity region, AFM-MMSEC benefits from a small advantage of about 2 codes compared to IFM-MMSEC and AFM-EGC. For capacity values lower than 20 codes, all configurations except IFM-MRC have close performances with a small difference of more or less 1 or 2 codes. The worst performances of IFM-MRC are due to its high MAI level.

It is important to point out that for a given transmission power $P^{(0)}$, a high value of the capacity indicator $C_{\phi}^{(0)}$ is equivalent to a low value of $T^{(0)}$, which reflects the level of inter-cell interference plus noise (cf. (6.13)). Equivalently, for a given value of $T^{(0)}$, a high value of the capacity indicator $C_{\phi}^{(0)}$ is equivalent to a high value of the transmission power $P^{(0)}$. Thus, for a given value of $T^{(0)}$, $C_{\phi}^{(0)}$ can be interpreted as a transmission power and therefore, the best physical layer configuration is the one for which the achievable load K_0 is the largest for a given level of $C_{\phi}^{(0)}$. This leads us to conclude that, for a given maximum power P_{max}, in order to achieve high capacity values of more than 60% of the available codes, we should use either AFM-MMSEC, IFM-MMSEC, or AFM-EGC since these configurations provide the largest capacity values for a given level of $C_{\phi}^{(0)}$. The level of inter-cell interference plus noise should also be low enough so as to allow the link level capacity indicator to take values above 21 dB, which is the level corresponding to the desired capacity values. However, for high level of inter-cell interference plus noise, we can still achieve more than 60% capacity values but at the expense of higher maximum power P_{max}.

	$K_0 = 8$	$K_0 = 16$	$K_0 = 24$	$K_0 = 32$
MCS1	6.3	5.70	5.30	5.10
MCS2	5.38	4.72	4.36	4.08
MCS3	9.80	9.17	8.81	8.65

Table 6-4: Target SINR in dB required to achieve 1% target FER for AFM-MMSEC configuration with three different MCS.

Focusing on AFM-MMSEC as being the best configuration, Table 6-4 summarizes the values of the target SINR in dB corresponding to K_0 = 8, 16, 24, and 32 for AFM-MMSEC using the three MCS described in Table 6-2. From Table 6-4, we notice that compared to MCS1, MCS2 achieves a target SINR gain of nearly 1 dB. This gain is the result of the higher diversity recovered by UMTS turbo code compared to convolutional code. Larger gains are expected if larger time and/or frequency diversity is available. Moreover, MCS3 requires higher target SINR values than MCS1 and MCS2 but it has the advantage of a double higher data rate, thanks to 16QAM modulation.

On the left of Figure 6-7, we illustrate the capacity indicator $C_{\phi}^{(0)}$ (dB) versus the cell throughput (cf. (6.12)) for AFM-MMSEC with MCS1, MCS2, and MCS3. On the right, we show the throughput values obtained for $C_{\phi}^{(0)} = \infty$, 26 dB, 24 dB, 22 dB, and 20 dB. As in Figure 6-6, we consider an AWGN variance equal to –7 dB for MMSEC equalization.

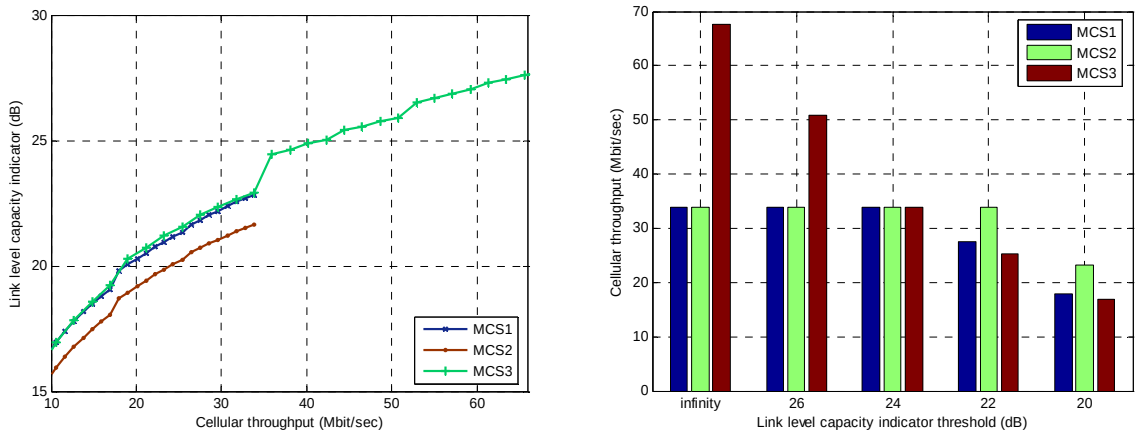

Figure 6-7: Cell throughput in Mbit/sec versus the link level capacity indicator threshold in dB for AFM-MMSEC configuration with three different MCS.

From Figure 6-7, it clearly appears that MCS2 outperforms MCS1. The target SINR gain of 1 dB achieved by MCS2 compared to MCS1 results in about 25% capacity gain. Moreover, MCS3 is shown to provide very close performances to MCS1 when the aggregated cellular throughput is less than 34 Mbit/sec. However, for higher throughputs up to 68 Mbit/sec, only MCS3 can be employed with a high enough transmission power for a given level of inter-cell interference plus noise. Thus, all three MCS compared, we can conclude that MCS2 should be employed for throughputs up to 34 Mbit/sec, while for higher throughputs up to 68 Mbit/sec, MCS3 should be employed with high enough transmission power.

To better understand the conclusions above, it is important to notice that the impact of a physical layer configuration on the capacity is essentially the cumulated effect of two main aspects, namely, diversity and MAI. While channel coding only affects diversity and therefore a gain in target SINR will automatically translate into a capacity gain, this is less obvious for configurations affecting both aspects. This important characteristic of system level evaluation is well captured by the novel capacity indicator presented above. It reflects the trade-off between MAI and diversity. The diversity aspect appears through the target SINR λ_{ϕ}, while the MAI aspect appears through the factors μ^{*} and β (cf. (6.14)).

6.4.3 Capacity Analysis at the System Level

In this chapter, we provide capacity evaluation using the static system level simulator. This is meant to provide more accurate results than with the above link level capacity indicator, and also enables to determine the validity domain of this indicator.

Table 6-5 summarizes the most relevant system level simulation parameters. We use the propagation model of an urban environment operating at 5 GHz carrier frequency [8].

Cellular layout	19 cells with sectoring (N_t = 3, N_s = 3)
Cell radius	300 m
Thermal noise	¤ Density power = -204 dBW/Hz ¤ Receiver noise figure = 5 dB
Propagation model	C_0 = -57.45 dB, μ = 2.8, σ_{SH} = 8 dB, ρ = 0.5
BS characteristics	¤ Maximum number of codes M = 32 ¤ Maximum power P_{max} = 10 dBW ¤ Interfering power $P_o \in \{0, 1, 2, 3, 4, 5\}$ dBW
Simulation control	¤ Maximum number of snapshots = 10000 ¤ Outage percentage threshold ε = 5%

Table 6-5: System level simulation parameters.

For MMSEC equalization, in order to compensate the power increase of about 0.5 dB due to the approximation made in Section 6.2.2.1, we increase the maximum power P_{max} by 0.5 dB with respect to the value of 10 dBW considered in Table 6-5.

Figure 6-8 depicts the pole capacity (P_{max} = +∞ dBW) and the single cell without sectoring constrained capacity (P_o = -∞ dBW, P_{max} = 10 dBW) for all configurations: IFM-MRC, IFM-EGC, IFM-MMSEC, AFM-MRC, AFM-EGC, and AFM-MMSEC. The first modulation and coding scheme MCS1 is assumed (cf. Table 6-2).

From Figure 6-8, we can first observe that all configurations have a full pole capacity of 32 codes except IFM-MRC for which the pole capacity is equal to 16 codes. These results are the same as those obtained previously from the link level capacity indicator (cf. Figure 6-6). In the single cell environment without sectoring, where there is no inter-cell interference, it is shown that IFM-MMSEC, AFM-MMSEC, and AFM-EGC have the highest capacity of 32 codes. IFM-EGC has slightly lower capacity of 30 codes, whereas AFM-MRC and IFM-MRC have much lower capacities of 22 and 13 codes respectively. These results agree with the link level capacity indicator results shown in Figure 6-6. It is of interest to point out here that since there is no inter-cell interference, the maximum power P_{max} = 10 dBW is found sufficient to achieve high capacity values up to 32 codes.

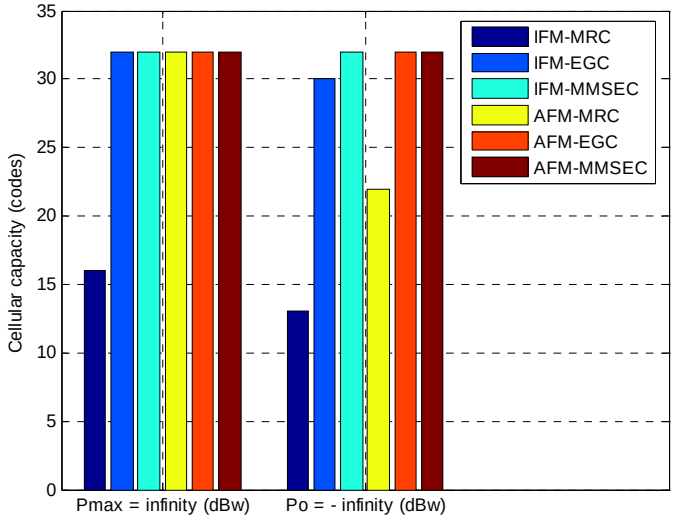

Figure 6-8: Pole and single cell capacities for IFM and AFM chip mappings with EGC, MRC, and MMSEC equalizations.

Now considering the inter-cell interference, Figure 6-9 illustrates the constrained capacity versus the inter-cell interfering BS transmission power P_o (dBW). The cellular layout is made up of 19 cells with sectoring as reported in Table 6-5.

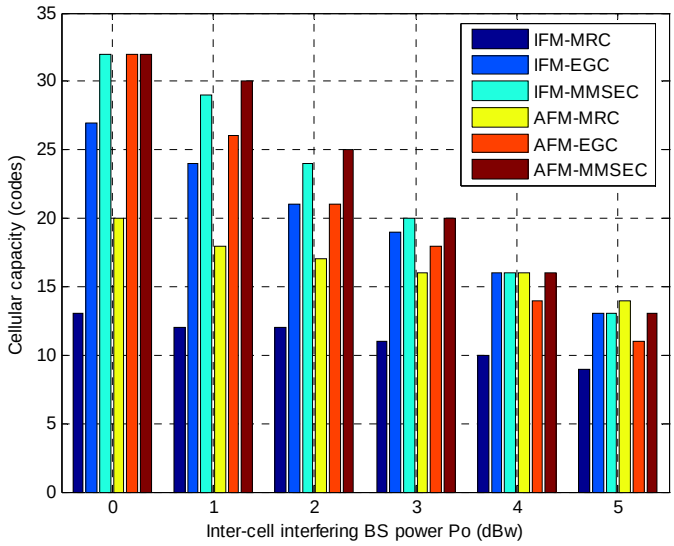

Figure 6-9: Capacity in codes versus the inter-cell interfering BS power in dBW for IFM and AFM chip mappings with EGC, MRC, and MMSEC equalizations.

As shown in Figure 6-9, to achieve capacity values more than 20 codes, i.e., ≈ 60% of the available codes, the level of inter-cell interference should be low enough with P_o lower than 3 dBW. In this range of capacity values, we can see that AFM-MMSEC and IFM-MMSEC

have similar performances with small advantage for AFM-MMSEC, and they outperform all other configurations. For the other configurations, they can be classified from the best to the worst as follows: AFM-EGC, IFM-EGC, AFM-MRC, IFM-MRC. For lower capacity values in the range between 10 and 20 codes, i.e., ≈ 30% and ≈ 60% of the available codes, AFM-MMSEC and IFM-MMSEC are shown to still provide the highest capacity, which is also provided by other configurations like IFM-EGC and AFM-MRC. These results match very well the results of the link level capacity indicator illustrated in Figure 6-6.

Thus, amongst all configurations, AFM-MMSEC and IFM-MMSEC are the most suitable to achieve capacity values more than 30% of the available codes. Moreover, for high capacity values (more than 60% of the available codes), AFM is found always better than IFM for all equalization schemes considered here. This leads to conclude that AFM is more suitable than IFM to achieve high capacity. The higher capacity provided by AFM means that the MAI reduction achieved by AFM has a stronger impact than the higher diversity gain achieved by IFM. These conclusions suggest that the trade-off between MAI and diversity is to favor MAI reduction than diversity gain, which is an important conclusion for MC-CDMA system design.

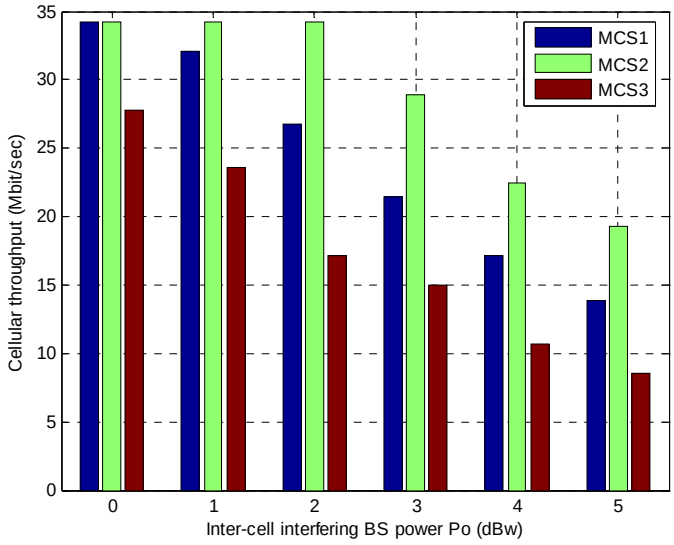

Figure 6-10: Cell throughput in Mbit/sec versus the inter-cell interfering BS power in dBW for AFM-MMSEC configuration with three different MCS.

Figure 6-10 depicts the cell throughput versus the inter-cell interfering BS power P_o (dBW) for AFM-MMSEC with MCS1, MCS2, and MCS3 (cf. Table 6-2). In Figure 6-10, it is shown that for moderate to high inter-cell interference, MCS2 achieves an important gain of about 30% compared to MCS1. This gain was estimated to be about 25% from the analysis of

the link level capacity indicator (cf. Figure 6-7). This shows once more the good match between link and system level capacity analysis. For MCS3, it is shown in Figure 6-10 that it provides much lower cellular throughputs than MCS1 and MCS2. This is mainly due to the tight constraint of maximum power P_{max} = 10.5 dBW.

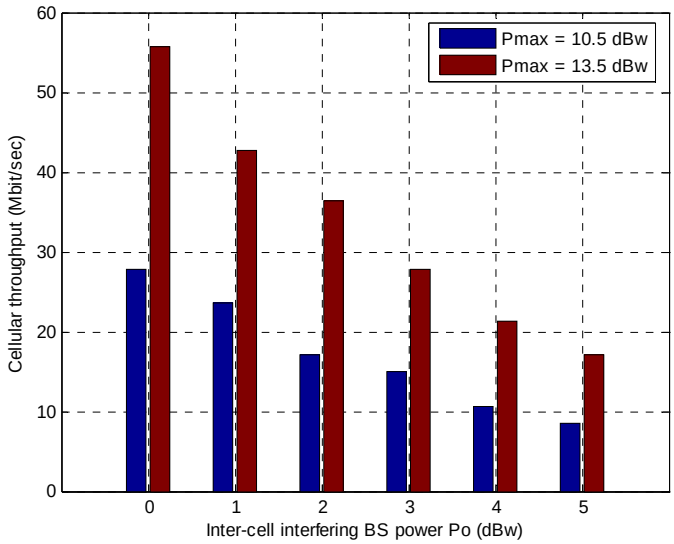

Figure 6-11: Cell throughput in Mbit/sec versus the inter-cell interfering BS power in dBW for AFM-MMSEC with MCS3 and two different maximum powers.

If we double the maximum power so that P_{max} = 13.5 dBW, the cellular throughput doubles as shown in Figure 6-11. In this case, MCS3 achieves high cellular throughputs that cannot be achieved by MCS1 and MCS2 for low inter-cell interference level. The latter result could be expected from the analysis of the link level capacity indicator (cf. Figure 6-7).

Thus, to sum up, UMTS turbo-code is found to achieve about 30% cellular throughput gain compared to UMTS convolutional code. Moreover, 16QAM modulation is shown to be more suitable than QPSK modulation to achieve high cellular throughputs of up to 68 Mbit/sec, at the cost of higher transmission power. For lower throughputs up to 34 Mbit/sec, QPSK modulation is found much better than 16QAM modulation for any level of inter-cell interference and any given transmission power.

6.4.4 Remarks and Discussions

It is important to point out that the gain obtained in term of the target SINR required to achieve the target FER does not necessarily result in a capacity gain. For instance, although the target SINR required to achieve 1% target FER is lower for IFM than AFM (cf. Table 6-3), AFM provided higher capacity than IFM for the different equalization techniques. On

the other hand, the target SINR gain of 1 dB achieved by UMTS turbo code compared to convolutional code converted directly into about 30% capacity gain.

Indeed, two cases should be distinguished depending on whether the physical layer module under consideration affects jointly the MAI and diversity or it affects only diversity. If the physical layer module affects only diversity, it will then only change the target SINR required to achieve the target FER while keeping the value of received SINR unchanged. For instance, this is the case of the modulation and coding schemes. In this case, it is straightforward that the SINR gain obtained thanks to a higher diversity will directly convert into a capacity gain. The capacity analysis allows here to select the best configurations of these modules based on the best trade-off between diversity and implementation complexity. In the other case, where the physical layer module affects jointly the MAI and diversity, both the target SINR and the value of received SINR are affected. This is the case of modules like for instance chip mapping, equalization, channel estimation, etc. In this case, the capacity performances of a given module reflect its joint impact on MAI and diversity. Thus, for these modules, a higher capacity means a better trade-off between MAI and diversity.

6.5 Conclusions

This chapter investigated the cellular capacity for MC-CDMA physical layer algorithms in the downlink of an urban macro-cellular environment. The cellular capacity is defined as the maximum number of users simultaneously served by the central base station with satisfied transmission quality requirements. The cellular capacity was evaluated at the system level through static Monte-Carlo simulations using the multi-frame oriented link to system interface developed in Chapter 5. Besides Monte-Carlo system level simulations, a novel link level capacity indicator was introduced in order to allow simple capacity analysis at the link level. The capacity analysis at the link level was shown to have very good agreement with the results obtained from system level simulations as it concisely captures the main effects impacting the capacity, namely, the diversity gain and MAI reduction.

The performances of different MC-CDMA configurations were evaluated in the context of the ETSI BRAN E channel model. It was shown that in particular, amongst all considered configurations, AFM-MMSEC and IFM-MMSEC are best suited to achieve capacity values more than 30% of the available codes. Furthermore, for high capacity values above 60% of the available codes, AFM chip mapping was found to ensure a better trade-off between MAI and diversity than IFM mapping for all considered equalization schemes. On the other hand, it

was shown that using UMTS turbo code instead of convolutional code results in about 30% capacity gain. At last, by comparing QPSK and 16QAM modulations, it was shown that for cellular throughputs up to 34 Mbit/sec, QPSK modulation is better than 16QAM modulation. However, for higher cellular throughputs up to 68 Mbit/sec, 16QAM should be used with high enough transmission power.

It is important to point out that the algorithms and configurations compared in this chapter represent an illustrative example of the results that can be obtained from the analysis of the cellular capacity. Indeed, the methodology and tools developed here are probably much more important than the example itself as they allow to evaluate the capacity for other physical layers and compare them to MC-CDMA scheme. This is with the aim of identifying the best suited physical layer algorithms and configurations for a given environment.

6.6 References

[1] Nortel Networks, "Update of OFDM SI simulation methodology," *3GPP TSG-RAN-1*, *Meeting #31, R1-030328*, Feb. 2003.

[2] J. Zander, S. Kim, "Radio Resource Management for Wireless Networks," *Artech House Publishers*, 2001.

[3] E. Seneta, "Non-negative matrices and Markov chains," *Springer-Verlag, 2nd edition*, 1981.

[4] S. V. Hanly, D. N. Tse, "Power Control and Capacity of Spread Spectrum Wireless Networks," *Automatica,* vol. 35, no. 12, pp. 1987—2012, Dec. 1999.

[5] K. Hiltunen, R. De Bernardi, "WCDMA Downlink Capacity Estimation," *Proc. IEEE Vehicular Technology Conference (VTC)*, pp. 992-996, May 2000.

[6] N. Enderlé, X. Lagrange, "Analyse de la Capacité Descendante d'un Système WCDMA," *Actes du congrès DNAC*, Nov. 2001.

[7] H. Holma, "A Study of UMTS Terrestrial Radio Access Performance," *Ph.D. thesis*, *Helsinki University of Technology,* Oct. 2003.

[8] IST European project MATRICE, "MC-CDMA Transmission Techniques for Integrated Broadband Cellular Systems," *website: www.ist-matrice.org*.

[9] W. Choi, J. Y. Kim, "Forward-Link Capacity of a DS/CDMA System with Mixed Multirate Sources," *IEEE Transactions on Vehicular Technology*, vol. 50, no. 3, pp. 737-749, May 2001.

[10] K. S. Gilhousen, I. M. Jacobs, R. Padovani, A. J. Viterbi, L. A. Weaver, C. E. Wheatley, "On the Capacity of a Cellular CDMA System," *IEEE Transactions on Vehicular Technology*, vol. 40, no. 2, pp. 303-312, May 1991.

[11] K. S. Gilhousen, I. M. Jacobs, R. Padovani, L. A. Weaver, "Increased Capacity Using CDMA for Mobile Satellite Communication," *IEEE Journal on Selected Areas in Communications (JSAC)*, vol. 8, no. 4, pp. 503-514, May 1990.

[12] IST European project FITNESS, "System-Level Simulation Methodology Defined," *Deliverable 4.1*, Oct. 2002.

[13] IST European project 4MORE, "4G MC-CDMA multiple antenna system On chip for Radio Enhancements," *website: www.ist-4more.org*.

[14] IST European project 4MORE, "Definition of the Carrier Frequency," *Deliverable 1.1*, Feb. 2004.

[15] B. C. V. Johansson, "Packet Data Capacity in a Wideband CDMA System," *Proc. IEEE Vehicular Technology Conference (VTC)*, vol. 3, pp. 1878-1883, May 1998.

[16] S. J. Lee, H. W. Lee, D. K. Sung, "Capacities of Single-Code and Multicode DS-CDMA Systems Accommodating Multiclass Services," *IEEE Transactions on Vehicular Technology,* vol. 48, no. 2, pp. 376-384, Mar. 1999.

[17] T. Neubauer, T. Baumgartner, E. Bonek, "Necessary and Sufficient Network Size for Pole Capacity Estimation in UMTS FDD," *Proc. European Conference on Wireless Technology (ECWT)*, Oct. 2000.

[18] UMTS 30.03 version 3.2.0, "Selection Procedures for the Choice of Radio Transmission Technologies of the UMTS," *ETSI TR 101 112 V3.2.0*, 1998.

[19] V. V. Veeravalli, A. Sendonaris, "The Coverage-Capacity Tradeoff in Cellular CDMA Systems," *IEEE Transactions on Vehicular Technology*, vol. 48, no. 5, pp. 1443-1450, Sep. 1999.

[20] A. M. Viterbi, A. J. Viterbi, "Erlang Capacity of a Power Controlled CDMA System," *IEEE Journal on Selected Areas in Communications (JSAC)*, vol. 11, no. 6, pp. 892-900, Aug. 1993.

[21] A. J. Viterbi, "CDMA: Principles of Spread Spectrum Communication," *Addison-Wesley Publishing Company*, 1995.

[22] R. D. Yates, "A Framework for Uplink Power Control in Cellular Radio Systems," *IEEE Journal on Selected Areas in Communications (JSAC)*, vol. 13, no. 7, pp. 1341-1348, Sep. 1995.

Chapter 7
Frame Oriented Link to System Interface

In this chapter, we investigate adequate link quality measures for accurate prediction of the probabilities of bit and frame error given a particular fading channel realization. This work is motivated by the practical need for such measures for accurate and realistic evaluation of the system level performance and for proper development of link adaptation algorithms such as adaptive modulation and coding, packet scheduling, hybrid-ARQ, etc.

7.1 Problem Statement

The term *frame oriented* refers to when the *Transmission Time Interval* (TTI) at the system level is equal to the frame duration. At the system level, in order to perform link adaptation, there is a need to predict the bit and frame error probabilities conditioned on the particular fading that affects the transmission of each frame of each radio link in the system [1][2]. We assume that the only measure available at the system level about the frame transmission quality is a profile of received SINR over the frame. Thus arises the problem of defining an accurate method to predict the bit and frame error probabilities from the only knowledge of the profile of received SINR over the frame.

Let N denote the frame size in complex data symbols. In general, the data symbols in the frame are transmitted over different resource elements (e.g. sub-carriers, antennas, etc.), and therefore they may experience different propagation and interference conditions. Thus, the data symbols may have different SINR values. Let **SINR** be the vector of N instantaneous SINR received at the output of the detector. The problem of determining an accurate prediction method comes back to looking for a relationship

$$P_e = f(\mathbf{SINR}) \tag{7.1}$$

where P_e denotes the frame error probability and f is the *prediction function*, which should fulfill the following requirements [3]:

1) f should be invariant with respect to the fading realization and system level parameters such as the cell load and the long-term received useful and interference powers.

2) f should be invariant with respect to the multi-path channel model as in general different radio links in the system have different channel delay profiles.

3) *f* should be applicable to different *Modulation and Coding Schemes* (MCS) in a soft way, i.e., by changing the values of some generic parameters. Considering link adaptation, this allows the prediction of the performance change by changing the MCS, based only on the received vector SINR. This is a crucial feature.

In the particular context of an AWGN channel, i.e., without fading and interference, the SINR becomes a *Signal to Noise Ratio* (SNR) and it remains constant over the frame. In this context, a direct relationship *h* exists between the SNR and error probability

$$P_{e,AWGN} = h(SNR) \tag{7.2}$$

The function *h* is called the *mapping function* and it is specific to the physical layer configuration. It is obtained through theoretical analysis or link level simulation with an AWGN channel. For instance, $h(x)$ is simply given by $Q(\sqrt{x})$ in the case of QPSK modulation without channel coding, where Q is the complementary error function.

In the general context of a fading channel, where the SINR varies over the frame, the prediction function *f* in (7.1) can be written exactly and without loss of generality as a compound function of the AWGN mapping function *h* and a compression function *g* [4]:

$$P_e = h \circ g(\mathbf{SINR}) = h(SINR_{eff}) \quad ; \quad SINR_{eff} = g(\mathbf{SINR}) \tag{7.3}$$

The function *g* is referred to as the *compression function* since its role is to compress the vector **SINR** of N_{fs} components into one scalar $SINR_{eff}$. The scalar $SINR_{eff}$ is called the *effective SINR* and it is defined as the SINR which would yield the same error probability in an equivalent AWGN channel as the associated vector **SINR** in a fading channel [4].

By writing (7.3), we have merely turned the problem of determining the prediction function *f* into the problem of determining the compression function *g*. We can anticipate that in order to be accurate, the compression function *g* should also account for the two following effects [5]:

- The SINR variation over the frame degrades the performance compared to the AWGN channel context, where the SINR is constant over the frame. Indeed, the SINR variation over the frame due to the frequency selectivity and/or time variation of the fading channel reflects the diversity achieved before decoding. The larger the SINR variation is, the lower the diversity achieved before decoding is.

- Bit interleaving in the context of selective fading channels improves the performance when channel coding is used. Indeed, bit interleaving changes the distribution of the SINR over the frame by making adjacent SINR before channel decoding independent, so that channel decoding recovers the maximum diversity.

7.2 Basic Solutions

These solutions have little or no theoretical justification but as they are proposed in the literature they represent part of the state of the art. It is therefore worth reviewing them and comparing them with new proposed solutions. The first solution that immediately comes to mind consists in approximating the effective SINR by the *Arithmetic Average SINR* (AAS) of the vector **SINR** [4], which is given by

$$SINR_{eff} = \frac{1}{N}\sum_{n=1}^{N} SINR_n \tag{7.4}$$

where $SINR_n$ denotes the instantaneous SINR for the n-th detected symbol in the frame. This solution typically underestimates the frame error probability because it overestimates the effective SINR by favoring the highest SINR components.

A second trivial solution consists in approximating the error probability by the average of the error probabilities obtained with the N components of the vector **SINR** in an AWGN channel. This can be written as [4]

$$SINR_{eff} = h^{-1}\left(P_e\right) = h^{-1}\left(\frac{1}{N}\sum_{n=1}^{N} P_{e,n}\right) = h^{-1}\left(\frac{1}{N}\sum_{n=1}^{N} h\left(SINR_n\right)\right) \tag{7.5}$$

where h^{-1} denotes the inverse of the mapping function h. This second solution typically overestimates the error probability. This is because the average error probability is generally dominated by the highest error probabilities obtained with the lowest SINR components [4].

A third solution in between the two above can also be proposed. This solution consists in taking the effective SINR as the geometric average of the vector **SINR**, which is given by

$$SINR_{eff} = \left(\prod_{n=1}^{N} SINR_n\right)^{\frac{1}{N}} \tag{7.6}$$

The *Geometric Average SINR* (GAS) is nothing else but the arithmetic average of the logarithm of **SINR**, i.e., average of **SINR** in dB which can be found in the literature [2]. The geometric average is equal to or smaller than the arithmetic average in (7.4), and it decreases

as the variance of **SINR** increases. That is why the GAS solution performs better than the two previous immediate solutions.

The three solutions described above give effective SINR estimates that do not depend on interleaving or on how the SINR varies within the frame. Hence, these solutions do not fulfill the expected properties listed in Section 7.1 relative to channel coding and interleaving, and are therefore likely to be inappropriate or inaccurate.

7.3 Enhanced Solutions

The enhanced solutions presented in this section are all derived from an analysis of the actual performance of a soft-input channel decoder over fading channel with bit interleaving. Part of these solutions is found in the literature, others are new. The effects of the following generic receiver modules are particularly considered: symbol demapping, bit de-interleaving, and soft-input convolutional decoding (see Figure 7-1).

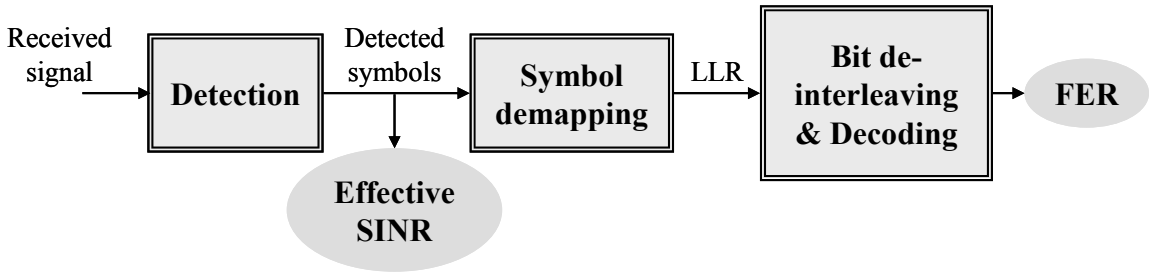

Figure 7-1: Receiver modules considered in the derivation of the effective SINR.

At the input of the symbol demapping module, the *n*-th received data symbol can generally be written as [6]

$$\hat{d}_n = A_n d_n + \nu_n \quad ; \quad \forall n = 1 \ldots N \tag{7.7}$$

where d_n is the *n*-th transmitted data symbol, A_n is the channel gain affecting data symbol d_n, and ν_n is the interference plus noise term modeled by a complex-valued Gaussian random variable with zero mean and variance σ_n^2.

The symbol demapping outputs the *Log-Likelihood Ratios* (LLR) of the bits $b_n^{(1)} b_n^{(2)} \ldots b_n^{(M)}$ mapped onto the 2^M-ary data symbol d_n. After symbol demapping, the *MN* LLR of the *MN* bits in the frame go into the bit de-interleaving module that changes their distribution in the frame. Next, the *MN* LLR after bit de-interleaving go into the decoding module that recovers the information bits transmitted within the frame.

Let us focus on the pair-wise error probability with the assumption that an effective SINR that maps well to the pair-wise error probability will also map well to the bit and frame error probabilities. Let $P_2(C,\hat{C})$ denote the pair-wise error probability between the transmitted codeword C and candidate codeword $\hat{C}$ at Hamming distance δ from C. For a given fading realization $\mathbf{H}$, the conditional pair-wise error probability is given by [6][7]

$$\begin{aligned} P_2\left(C,\hat{C}\middle|\mathbf{H}\right) &= \Pr\left\{\sum_{i=1}^{MN}\left|y_i-\hat{x}_i\right|^2 < \sum_{i=1}^{MN}\left|y_i-x_i\right|^2\right\} = \Pr\left\{\sum_{i=1}^{MN} 2y_i\left(\hat{x}_i-x_i\right)>0\right\} \\ &= \Pr\left\{\sum_{k=1}^{\delta} 4y_{i_k}\hat{x}_{i_k}>0\right\} = \Pr\left\{\sum_{k=1}^{\delta}\chi_{i_k}>0\right\} = \Pr\{X>0\} \end{aligned} \tag{7.8}$$

where y_i denotes the i-th input LLR, x_i is equal to 1 if the i-th bit in the codeword C is equal to 0, and –1 otherwise, and $i_k \in \{1, \ldots, MN\}$ gives the position of the k-th differing bit between codewords C and $\hat{C}$.

The variables $\{\chi_{i_k} = y_{i_k}\hat{x}_{i_k}\}$ are independent thanks to the independence of the AWGN samples $\{\nu_{i_k}\}$ and, thus, by applying the *Central Limit Theorem* (CLT) to X, we can justify that X follows a Gaussian distribution with mean m_X and variance σ_X^2. Thus, (7.8) can simply be rewritten as

$$P_2\left(C,\hat{C}\middle|\mathbf{H}\right) = \mathrm{Q}\left(\sqrt{\frac{m_X^2}{\sigma_X^2}}\right) \tag{7.9}$$

The problem of determining the pair-wise error probability in (7.9) turns therefore into determining the conditional mean m_X and variance σ_X^2, which are given by

$$m_X = \sum_{k=1}^{\delta} E_\nu\left\{\chi_{i_k}\right\} \quad ; \quad \sigma_X^2 = \sum_{k=1}^{\delta}\mathrm{var}_\nu\left\{\chi_{i_k}\right\} \tag{7.10}$$

where $E_\nu\{z\}$ and $\mathrm{var}_\nu\{z\}$ denote respectively the expectation value and variance of the random variable z with respect to the distribution of ν.

In the case of QPSK modulation with Gray mapping (cf. Figure 4-2), the LLR of the bits $b_n^{(1)}$ and $b_n^{(2)}$ mapped onto data symbol d_n are found from (7.7) as (cf. Appendix B.1)

$$y_n^{(1)} = -\frac{2\sqrt{2}A_n\Re\left(\hat{d}_n\right)}{\sigma_n^2} \quad ; \quad y_n^{(2)} = -\frac{2\sqrt{2}A_n\Im\left(\hat{d}_n\right)}{\sigma_n^2} \tag{7.11}$$

where $\Re(z)$ and $\Im(z)$ denote respectively the real and imaginary parts of the complex variable z. From (7.7) and (7.11), the following equations are obtained

$$E_\nu\left\{\chi_n^{(1)}\right\}=E_\nu\left\{\chi_n^{(2)}\right\}=2SINR_n \quad ; \quad \mathrm{var}_\nu\left\{\chi_n^{(1)}\right\}=\mathrm{var}_\nu\left\{\chi_n^{(2)}\right\}=4SINR_n \tag{7.12}$$

where $\chi_n^{(i)}=y_n^{(i)}\hat{x}_n^{(i)}$ (cf. (7.8)) and $SINR_n$ is the SINR for data symbol d_n:

$$SINR_n=\frac{A_n^2}{\sigma_n^2} \tag{7.13}$$

From (7.10) and (7.12), the pair-wise error probability in (7.9) and its Chernoff bound denoted by $B_2(C,\hat{C})$ [8] are therefore obtained as

$$P_2\left(C,\hat{C}\middle|\mathbf{H}\right)=\mathrm{Q}\left(\sqrt{\sum_{k=1}^{\delta}SINR_{i_k}}\right)\le B_2\left(C,\hat{C}\middle|\mathbf{H}\right)=\exp\left(-\frac{1}{2}\sum_{k=1}^{\delta}SINR_{i_k}\right) \tag{7.14}$$

Since it is easier to handle the exponential function than the Q function, the Chernoff bound B_2 replaces the pair-wise error probability P_2 to derive the effective SINR.

7.3.1 Minimum Based Effective SINR

This solution considers only the free distance δ_f of the convolutional code and makes the approximation of replacing δ_f by another distance D called *minimum distance error event*. In other terms, the distance D is the minimum length of the sequence of contiguous bits that includes the δ_f erroneous bits, and it is determined from the constraint length, rate, and generator polynomials of the convolutional code [4]. As mentioned in [4], the approximation of replacing the free distance δ_f by D is valid only for slowly varying SINR over the frame.

In this solution, the effective SINR is derived from the maximum value of the Chernoff bound (cf. (7.14)) taken over all the $2N$-D+1 possible sequences $\{S_m\}$ of D contiguous bits in the frame of $2N$ bits, where S_m denotes here the sequence of D contiguous de-interleaved bits starting at index $m \in [1,2N\text{-}D\text{+}1]$. From (7.3) and (7.14), the effective SINR can be calculated as [4]

$$\exp\left(-\frac{1}{2}DSINR_{eff}\right)=\max_{m=1\ldots 2N-D+1}\left(\prod_{k=0}^{D-1}\exp\left(-\frac{1}{2}SINR_{P(m+k)}\right)\right) \tag{7.15}$$

which reduces to

$$SINR_{eff} = \frac{1}{D} \min_{m=1\ldots 2N-D+1} \left(\sum_{k=0}^{D-1} SINR_{P(m+k)} \right) \tag{7.16}$$

where P is the de-interleaving function, i.e., $P(m+k)$ is the position of the bit b_{m+k} after de-interleaving, and $SINR_m$ is the SINR for encoded bit b_m.

As discussed in [4], the *Minimum Based Effective SINR* (MBES) solution in (7.16) typically overestimates the error probability. This is because it evaluates the worst combination of D contiguous SINR in the frame without taking into account the error patterns that are specific to the code. Thus, it considers error patterns that may not exist, and therefore, it tends to overestimate the error probability. Here, it is important to point out that MBES requires knowledge of the convolutional code parameter D and de-interleaving function P. Moreover, it requires the vector **SINR** to be processed bit wise.

7.3.2 Exponential Effective SINR

This solution proposed by [9] is currently the most commonly used state of the art solution. The main idea behind this solution is to assume that the positions $\{i_k\}$ of the δ erroneous bits are independent and uniformly distributed over the frame when considering all codewords at distance δ. This also implicitly assumes that the channel interleaver is ideal and allows relaxing the constraint of knowing and accounting for the specificity of the interleaver. The effective SINR is then found by averaging the Chernoff bound in (7.14) over the variables $\{i_k\}$. Assuming that the variables $\{ SINR_{i_k} \}$ are independent and identically distributed taking values in the vector **SINR** with equal probabilities, the effective SINR is calculated as

$$\begin{aligned} \exp\left(-\frac{\delta}{2} SINR_{eff} \right) &= E\left\{ \exp\left(-\frac{1}{2} \sum_{k=1}^{\delta} SINR_{i_k} \right) \right\} = E\left\{ \prod_{k=1}^{\delta} \exp\left(-\frac{1}{2} SINR_{i_k} \right) \right\} \\ &= \prod_{k=1}^{\delta} E\left\{ \exp\left(-\frac{1}{2} SINR_{i_k} \right) \right\} = \left(\frac{1}{N} \sum_{n=1}^{N} \exp\left(-\frac{1}{2} SINR_n \right) \right)^{\delta} \end{aligned} \tag{7.17}$$

which simplifies to

$$SINR_{eff} = -2 \log\left(\frac{1}{N} \sum_{n=1}^{N} \exp\left(-\frac{1}{2} SINR_n \right) \right) \tag{7.18}$$

The effective SINR in (7.18) is called the *Exponential Effective SINR* (EES) and it has been shown in [9] to provide good performances in the case of QPSK modulation. Furthermore, as shown in (7.18), the EES can easily be evaluated since it does not require

knowledge of the convolutional code and de-interleaving characteristics. Here, the effects of convolutional code and de-interleaving are included only in the mapping function *h* but not in the compression function *g*. Moreover, the vector **SINR** is only required to be provided symbol wise.

Being inspired by the form of the EES in (7.18), the authors in [9] propose the following *Generalized EES* (GEES) solution for any modulation scheme:

$$SINR_{eff} = -\beta \log\left(\frac{1}{N} \sum_{n=1}^{N} \exp\left(-\frac{1}{\beta} SINR_n \right) \right) \tag{7.19}$$

where β is an optimization factor specific to the physical layer configuration. Denoting by N_r the number of runs or simulations, β is determined according to the *Least Mean Square Error* (LMSE) criterion applied to the simulated and predicted FER as given below [9]

$$\beta_{opt} = \arg\min_{\beta} \left(\sum_{r=1}^{N_r} \left(FER_s^{(r)} - FER_p^{(r)}(\beta) \right)^2 \right) \tag{7.20}$$

where $FER_s^{(r)}$ is the FER obtained from simulation at the *r*-th run, and $FER_p^{(r)}(\beta)$ is the FER predicted at the *r*-th run from the GEES in (7.19).

7.3.3 Chi-square Effective SINR

Here, we propose a novel solution that we call *Chi-square Effective SINR* (CES). In this solution, we approximate the distribution of the summation *S* of the δ SINR variables in (7.14) by a noncentral chi-square distribution, which is given by [8]

$$p_S(s) = \frac{1}{\sqrt{2\pi\sigma^2 s}} \exp\left(-\frac{\left(s + m^2\right)}{2\sigma^2} \right) \cosh\left(\frac{\sqrt{s}m}{\sigma^2} \right), \quad s \geq 0 \tag{7.21}$$

where the parameters *m* and σ^2 are determined from the following equations:

$$\begin{aligned} m^2 &= \sqrt{E\{S\}^2 - \frac{1}{2}\mathrm{var}\{S\}} \quad ; \quad \sigma^2 = E\{S\} - m^2 \\ E\{S\} &= \delta\, E\{\mathbf{SINR}\} \quad ; \quad \mathrm{var}\{S\} = \delta\, \mathrm{var}\{\mathbf{SINR}\} \end{aligned} \tag{7.22}$$

In (7.22), $E\{\mathbf{SINR}\}$ and $\mathrm{var}\{\mathbf{SINR}\}$ denote respectively the mean and variance of the vector **SINR**.

There are mainly two reasons behind our choice of the noncentral chi-square distribution. The first reason is that it models better the actual distribution of the summation of the δ SINR

variables than a Gaussian distribution. This result has been validated through simulations. Figure 7-2 illustrates an example of the distribution of the summation S for $\delta = 12$ assuming real interleaving and the associated chi-square noncentral approximation. This example considers the general context of correlated channel coefficients obtained from AFM chip mapping over the urban ETSI BRAN E channel. As shown in Figure 7-2, the chi-square noncentral distribution matches very well the distribution obtained from simulation.

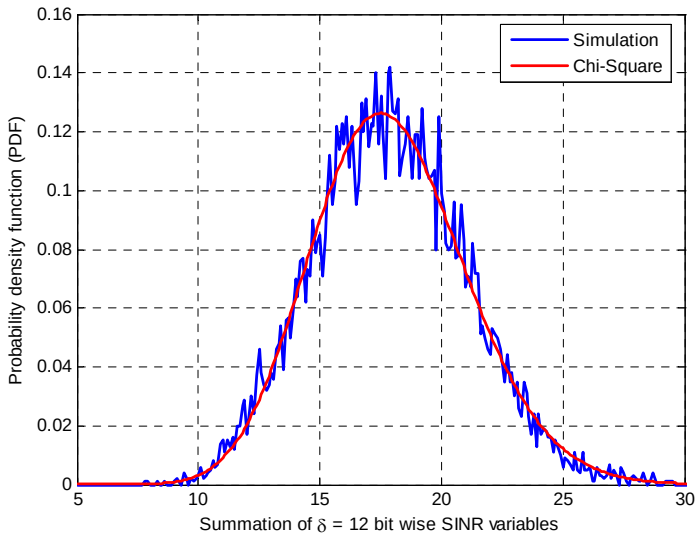

Figure 7-2: PDF of the summation of 12 SINR variables.

The second reason is that with the chi-square noncentral distribution, we are able to extract an analytical form of the effective SINR, which is obtained as:

$$\exp\left(-\frac{\delta\, SINR_{eff}}{2}\right) = \int_0^{+\infty} \exp\left(-\frac{s}{2}\right) p_S(s)\, ds \tag{7.23}$$

which simplifies to

$$SINR_{eff} = \frac{1}{\delta}\left(\frac{m^2}{1+\sigma^2} + \log\left(1+\sigma^2\right)\right) \tag{7.24}$$

The effective SINR in (7.24) depends explicitly on the distance δ. Through simulations, we have studied the variation of the $SINR_{eff}$ in (7.24) with respect to distance δ. We have found that it is almost invariant with respect to δ. From this observation, the case $\delta = 1$ immediately suggests itself, and the effective SINR becomes

$$SINR_{eff} = \frac{m^2}{1+\sigma^2} + \log\left(1+\sigma^2\right) \tag{7.25}$$

where m and σ^2 are determined from (7.22) for $\delta = 1$.

Thus, similarly to EES (cf. Section 7.3.2), CES in (7.25) does not require knowledge of the channel code characteristics. This facilitates its extension to other types of channel codes like turbo codes, which free distances are more complex to determine and do not have the same impact on the performance as in convolutional codes. Compared to EES, CES benefits from the advantages of being easier to implement and less sensitive to errors that may occur in the estimation of the vector **SINR**. This is because CES requires the calculation of only the mean and variance of the vector **SINR**, whereas EES requires the calculation of the summation of the exponential of the N components in the vector **SINR**.

Following the same intuitive EES generalization in (7.19), the following *Generalized CES* (GCES) can be proposed for any modulation scheme:

$$SINR_{eff} = \frac{m^2}{1+\frac{2}{\beta}\sigma^2} + \frac{\beta}{2}\log\left(1+\frac{2}{\beta}\sigma^2\right) \tag{7.26}$$

where β minimizes the mean square error between the predicted and simulated FER as given in (7.20).

7.3.4 Refined Generalized Exponential and Chi-Square Effective SINR

Here, we propose new refined expressions of the GEES and GCES solutions based on an analysis of the pair-wise error probability in the case of 16QAM modulation.

In the case of 16QAM modulation with Gray mapping (cf. Figure 4-2), the LLR of the bits $b_n^{(1)}$ and $b_n^{(3)}$ mapped onto data symbol d_n are well approximated by (cf. Appendix B.2)

$$y_n^{(1)} \approx -\frac{4A_n}{\sigma_n^2\sqrt{10}}\Re\left(\hat{d}_n\right) \quad ; \quad y_n^{(3)} \approx -\frac{4A_n}{\sigma_n^2\sqrt{10}}\left(\left|\Re\left(\hat{d}_n\right)\right| - \frac{2A_n}{\sqrt{10}}\right) \tag{7.27}$$

The LLR $y_n^{(2)}$ and $y_n^{(4)}$ of the bits $b_n^{(2)}$ and $b_n^{(4)}$ have the same expressions as $y_n^{(1)}$ and $y_n^{(3)}$ respectively except that the imaginary part replaces the real part in (7.27) (cf. Appendix B.2).

Let us consider the first bit $b_n^{(1)}$. The mean and variance of $\chi_n^{(1)}$ are found equal to

$$E\{\chi_n^{(1)}\}=\begin{cases}\frac{2}{5}SINR_n \text{ for } \Re(d_n)=\frac{1}{\sqrt{10}} \\ \frac{6}{5}SINR_n \text{ for } \Re(d_n)=\frac{3}{\sqrt{10}}\end{cases} \quad ; \quad \text{var}\{\chi_n^{(1)}\}=\frac{4}{5}SINR_n \tag{7.28}$$

As shown in (7.28), $E\{\chi_n^{(1)}\}$ takes two values depending on whether the real part of the data symbol d_n is equal to $1/\sqrt{10}$ or $3/\sqrt{10}$. The mean and variance of $\chi_n^{(2)}$ are exactly the same as in (7.28) except that $\Re(d_n)$ should be changed into $\Im(d_n)$.

Let us now consider the bit $b_n^{(3)}$. In order to derive the mean and variance of $\chi_n^{(3)}$, we make the following approximation

$$E\{|a+x|\}=\sqrt{\frac{2\sigma^2}{\pi}}\exp\left(-\frac{a^2}{2\sigma^2}\right)-a\left(1-2Q\left(\frac{-a}{\sigma}\right)\right)\approx|a|\left(1-2Q\left(\sqrt{\frac{a^2}{\sigma^2}}\right)\right)\approx|a| \tag{7.29}$$

where a is a constant and x is a real-valued zero mean Gaussian random variable of variance σ^2. In (7.29), the ratio a^2/σ^2 is assumed to be large enough.

Using the approximation in (7.29), the mean and variance of $\chi_n^{(3)}$ are obtained as

$$E\{\chi_n^{(3)}\}=\frac{2}{5}SINR_n \quad ; \quad \text{var}\{\chi_n^{(3)}\}=\frac{4}{5}SINR_n \tag{7.30}$$

As well, the mean and variance of $\chi_n^{(4)}$ are found to have the same expressions as in (7.30). From (7.28) and (7.30), the mean and variance in (7.10) are then obtained as

$$m_X=\frac{2}{5}\left(\sum_{k=1}^{\delta}SINR_{i_k}+2\sum_{k\in E_0}SINR_{i_k}\right) \quad ; \quad \sigma_X^2=\frac{4}{5}\sum_{k=1}^{\delta}SINR_{i_k} \tag{7.31}$$

The set E_0 in (7.31) denotes the set of indexes $k = 1\ldots\delta$ such that the k-th erroneous bit b_{i_k} occupies the first position $b^{(1)}$ in the binary representation $b^{(1)}b^{(2)}b^{(3)}b^{(4)}$ of data symbol d and $\Re(d) = 3/\sqrt{10}$, or it occupies the second position $b^{(2)}$ and $\Im(d) = 3/\sqrt{10}$.

From (7.31), the pair-wise error probability in (7.9) can be expressed as

$$P_2\left(C,\hat{C}|\mathbf{H}\right)=\mathrm{Q}\left(\sqrt{\frac{1}{5}\frac{\left(\sum_{k=1}^{\delta}SINR_{i_k}+2\sum_{k\in E_0}SINR_{i_k}\right)^2}{\sum_{k=1}^{\delta}SINR_{i_k}}}\right) \tag{7.32}$$

Here, it is important to point out that unlike the case of QPSK modulation, the pair-wise error probability in this case of 16QAM modulation varies with respect to the transmitted codeword C since the set E_0 is specific to codeword C. This is because the symbol mapping in 16QAM modulation is nonlinear.

Taking at first the particular context of an AWGN channel, (7.32) reduces to

$$P_{2,AWGN}\left(C,\hat{C}\right)=\mathrm{Q}\left(\sqrt{\frac{1}{5}\left(1+2\frac{i_0}{\delta}\right)^2\delta\,SNR}\right) \tag{7.33}$$

where $i_0 = \mathrm{card}(E_0)$. In order to remove the dependency of the pair-wise error probability in (7.33) on the codeword C, we make the approximation

$$P_{2,AWGN}\left(C,\hat{C}\right)=\mathrm{Q}\left(\sqrt{\frac{2}{\beta_1}\delta\,SNR}\right) \tag{7.34}$$

where β_1 is an optimization factor. The approximation done in (7.34) suggests that the mapping between the error probability and SINR for 16QAM modulation in the context of an AWGN channel is a simple shift of the mapping obtained for QPSK modulation (cf. (7.14)).

$$h_{16QAM}\left(SNR\right)=h_{QPSK}\left(\frac{2}{\beta_1}SNR\right) \tag{7.35}$$

In the 16QAM Gray modulation, among all the 64 bits only 8 belong to the set E_0 (cf. Figure 4-2). Thus, the probability for a bit to belong to the set E_0 is equal to 1/8. Taking this probability into account, we approximate the ratio i_0/δ in (7.33) by 1/8, and therefore, we get an approximated value of β_1 equal to 6.4.

In the context of a fading channel, we introduce another optimization factor β_2 and approximate (7.32) by

$$P_2\left(C,\hat{C}|\mathbf{H}\right)=\mathrm{Q}\left(\sqrt{\frac{2}{\beta_2}\sum_{k=1}^{\delta}SINR_{i_k}}\right) \tag{7.36}$$

Assuming that the approximations made in (7.35) and (7.36) still hold for any modulation scheme, we propose a *Refined GEES* (RGEES) that can be determined as:

$$\exp\left(-\frac{\delta\,SINR_{eff}}{\beta_1}\right)=\prod_{k=1}^{\delta}E\left\{\exp\left(-\frac{SINR_{i_k}}{\beta_2}\right)\right\}=\left(\frac{1}{N}\sum_{n=1}^{N}\exp\left(-\frac{SINR_n}{\beta_2}\right)\right)^{\delta} \tag{7.37}$$

which reduces to

$$SINR_{eff} = -\beta_1 \log\left(\frac{1}{N} \sum_{n=1}^{N} \exp\left(-\frac{SINR_n}{\beta_2} \right) \right) \tag{7.38}$$

In the same way, we propose a *Refined GCES* (RGCES) as:

$$SINR_{eff} = \frac{\beta_1}{\beta_2} \left(\frac{m^2}{1 + \frac{2}{\beta_2}\sigma^2} + \frac{\beta_2}{2} \log\left(1 + \frac{2}{\beta_2}\sigma^2 \right) \right) \tag{7.39}$$

The value of β_1 is determined according to the LMSE criterion applied to the AWGN mapping function h for the modulation scheme under consideration and for QPSK as

$$\beta_{1opt} = \arg\min_{\beta_1} \left(\sum_{r=1}^{N_r} \left(h_{MS}\left(SNR^{(r)}\right) - h_{QPSK}\left(\frac{2}{\beta_1} SNR^{(r)} \right) \right)^2 \right) \tag{7.40}$$

The value of β_2 is determined according to the LMSE criterion applied to the simulated and predicted FER as given in (7.20).

Thus, the RGEES and RGCES solutions use two parameters β_1 and β_2 instead of only one parameter β for the GEES and GCES solutions.

7.4 Numerical Results

In this section, we compare the performances of the following effective SINR solutions: AAS (cf. (7.4)), GAS (cf. (7.6)), MBES (cf. (7.16)), GEES (cf. (7.19)), GCES (cf. (7.26)), RGEES (cf. (7.38)), and RGCES (cf. (7.39)). We evaluate the performances in the context of the MC-CDMA physical layer in the downlink. In this context, the instantaneous SINR at the output of the SUD detector associated with data symbol d_n has the form (cf. (5.29))

$$SINR_n = \frac{P_u R_n^2}{S_n \sigma_B^2 + T_n \sigma_{\xi+\nu}^2} \tag{7.41}$$

where P_u is the transmission power, σ_B^2 is the OGN variance, $\sigma_{\xi+\nu}^2$ is AWGN variance representing the inter-cell interference plus noise at the link level, and the quantities R_n, S_n, and T_n are given in (5.30) (cf. Section 5.3.2).

The key simulation parameters are summarized in Table 7-1 [10]. The choice of adjacent frequency chip mapping (AFM), which results in significantly correlated channel coefficients,

is motivated by the aim for a large variation of the SINR within the vector **SINR**. On the other hand, we consider both the urban ETSI BRAN E and indoor ETSI BRAN A channel models [10] in order to verify the second requirement in Section 7.1 of invariance with respect to the multi-path channel model.

Channel coding	¤ UMTS convolutional code (R_c = ½) ¤ Frame size = 736 information bits ¤ Soft input Viterbi decoding algorithm
Symbol mapping	¤ QPSK-Gray mapping ¤ 16QAM-Gray mapping
Chip mapping	Adjacent Frequency Mapping (AFM)
Receiver type	SUD-MMSEC
Channel model	¤ Urban ETSI BRAN E ¤ Indoor ETSI BRAN A

Table 7-1: MC-CDMA link level simulation parameters.

In order to ensure a high accuracy, we perform several runs of the link to system level interface simulator. All runs have the same physical layer configuration but different fading channel realizations. For each run, a large number of frames are transmitted through the same fading realization but with different interference plus noise realizations. The FER is calculated as the ratio of the number of erroneous frames to the total number of transmitted frames.

Each run r yields a couple ($SINR_{eff}^{(s)}$, $FER^{(s)}$). From the AWGN mapping function h, we deduce the value $SINR_{eff}^{(p)}$ of effective SINR required to predict the simulated value $FER^{(s)}$. The difference between $SINR_{eff}^{(s)}$ and $SINR_{eff}^{(p)}$ in dB is denoted by *Diff*. It represents the prediction error for the given run. From all runs, we evaluate the performance in terms of the average of |*Diff*| denoted by *AverageDiff* and the maximum of |*Diff*| for 95% of the time denoted by $MaxDiff_{95\%}$. This latter quantity is given by

$$MaxDiff_{95\%} = \arg\max_{x}\left(\Pr\left(|Diff| < x\right) \le 0.95\right) \tag{7.42}$$

Obviously, the lower *AverageDiff* and $MaxDiff_{95\%}$ are, the better the performance of the effective SINR becomes.

Table 7-2 summarizes the values of *AverageDiff* and $MaxDiff_{95\%}$ for all compared solutions in the case of QPSK modulation. The value of β is found equal to 1.89 and 1.85 for EES and CES respectively. For REES and RCES, the value of β_1 is obviously equal to 2 in this case of QPSK modulation, and β_2 is found equal to 2.04 and 2.05 respectively.

	AAS	GAS	MBES	GEES $\beta = 1.89$	GCES $\beta = 1.85$	RGEES $\beta_1 = 2, \beta_2 = 2.04$	RGCES $\beta_1 = 2, \beta_2 = 2.05$
AverageDiff (dB)	1.03	0.10	0.32	0.04	0.08	0.03	0.08
$MaxDiff_{95\%}$ (dB)	1.30	0.26	0.72	0.08	0.16	0.07	0.17

Table 7-2: Performances of different effective SINR solutions with QPSK modulation.

From Table 7-2, we can see that RGEES and RGCES have quite the same performances as GEES and GCES respectively. This is normal because we are in the case of QPSK modulation and the proposed refinement should enhance the performances for higher order modulations than QPSK. We can also notice from Table 7-2 that GCES (RGCES) provides good results that are slightly lower than GEES (RGEES). However, it is worth recalling here that GCES (RGCES) is easier to implement and less sensitive to **SINR** estimation errors. By ordering from the best to the worst, the compared solutions can be classified as follows: RGEES, GEES, RGCES, GCES, GAS, MBES, and AAS.

Figure 7-3 and Figure 7-4 illustrate the performance of the RGEES solution in the case of QPSK modulation. Figure 7-3 depicts the simulated and predicted bit and frame error probabilities. It shows the very good agreement between the prediction and simulation results. Figure 7-4 depicts the CDF of the difference in absolute value between the measured RGEES and RGEES required to predict the measured frame error probability. The very small values of *AverageDiff* equal to 0.03 dB and $MaxDiff_{95\%}$ equal to 0.07 dB reflect the very good performance of the RGEES solution.

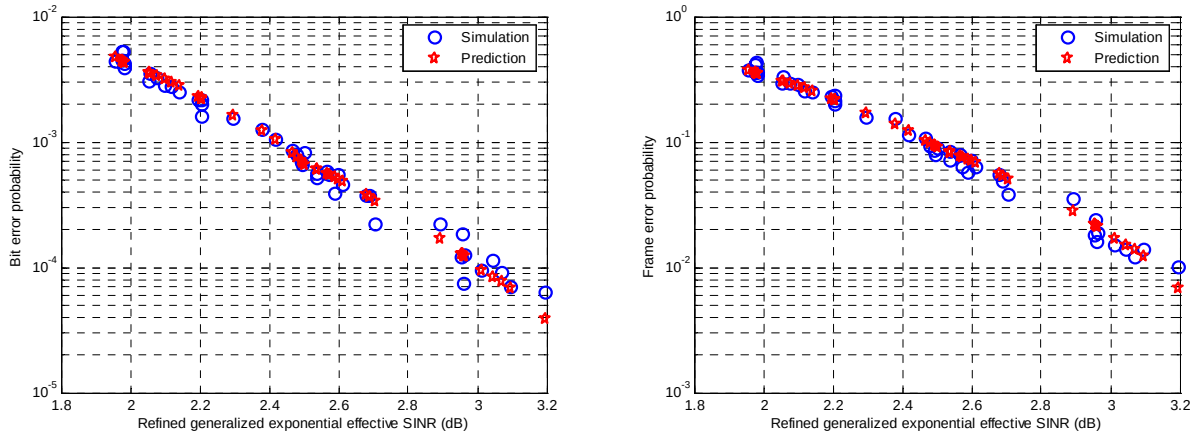

Figure 7-3: Bit and frame error probabilities for RGEES solution with QPSK modulation.

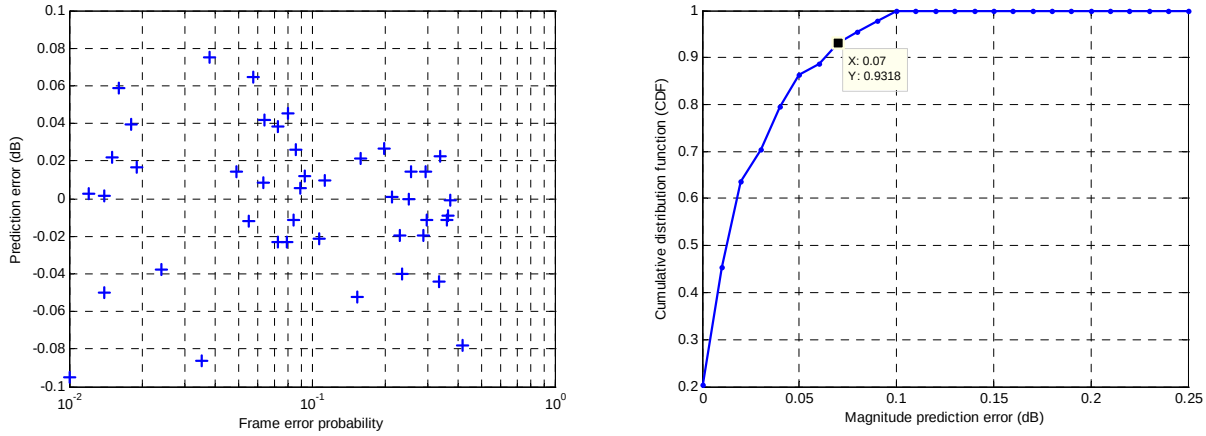

Figure 7-4: Prediction error for RGEES solution with QPSK modulation.

Table 7-3 summarizes the values of *AverageDiff* and $MaxDiff_{95\%}$ in the case of 16QAM modulation. The value of β is equal to 5.28 and 5.55 for GEES and GCES respectively. For RGEES and RGCES, β_1 is equal to 6.91 and β_2 is found equal to 7.67 and 7.56 respectively.

	AAS	GAS	MBES	GEES $\beta = 5.28$	GCES $\beta = 5.55$	RGEES $\beta_1 = 6.91$, $\beta_2 = 7.67$	RGCES $\beta_1 = 6.91$, $\beta_2 = 7.56$
AverageDiff (dB)	1.33	0.4	0.33	0.1	0.14	0.05	0.08
$MaxDiff_{95\%}$ (dB)	1.64	0.57	0.54	0.19	0.29	0.1	0.15

Table 7-3: Performances of different effective SINR solutions with 16QAM modulation.

From Table 7-3, we notice the better performance of RGEES and RGCES compared to GEES and GCES respectively. Thus, the proposed refinement improves the performance with no additional complexity. We can also see that RGEES provides the best performance, while RGCES performs slightly worse than RGEES but it has the advantages of an easier implementation and a lower sensitivity to **SINR** estimation errors. From Table 7-3, we can classify the solutions from the best to the worst as follows: RGEES, RGCES, GEES, GCES, MBES, GAS, and AAS.

Figure 7-5 and Figure 7-6 illustrate the RGEES performance in the case of 16QAM modulation. The optimal value of β_1 is found from (7.40) equal to 6.91, which is not far from the expected value of 6.4 found by approximating the ratio i_0/δ in (7.33) by 1/8. Figure 7-5 depicts the simulated and predicted bit and frame error probabilities, while Figure 7-6 shows the difference between the measured and required RGEES and the CDF of its absolute value. Figure 7-5 shows the very good match between prediction and simulation results. From

Figure 7-5, we can also notice the high sensitivity of the BER and FER to small differences in the effective SINR, as small as 0.1 dB. For instance, a difference of 0.2 dB leads to 5% FER instead of 10%. From Figure 7-6, the very small values of *AverageDiff* equal to 0.05 dB and $MaxDiff_{95\%}$ equal to 0.1 dB reflect once more the effectiveness of the RGEES solution in this case of 16QAM modulation.

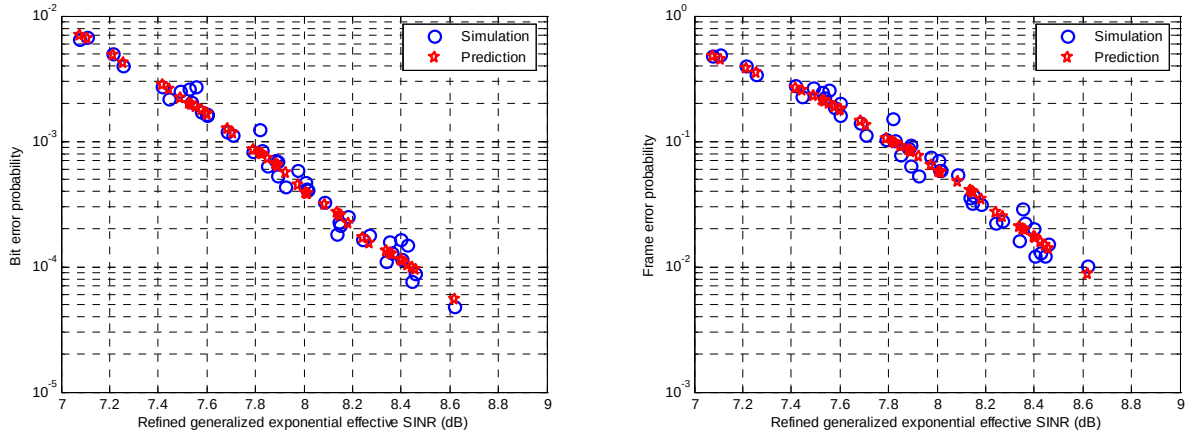

Figure 7-5: Bit and frame error probabilities for RGEES solution with 16QAM modulation.

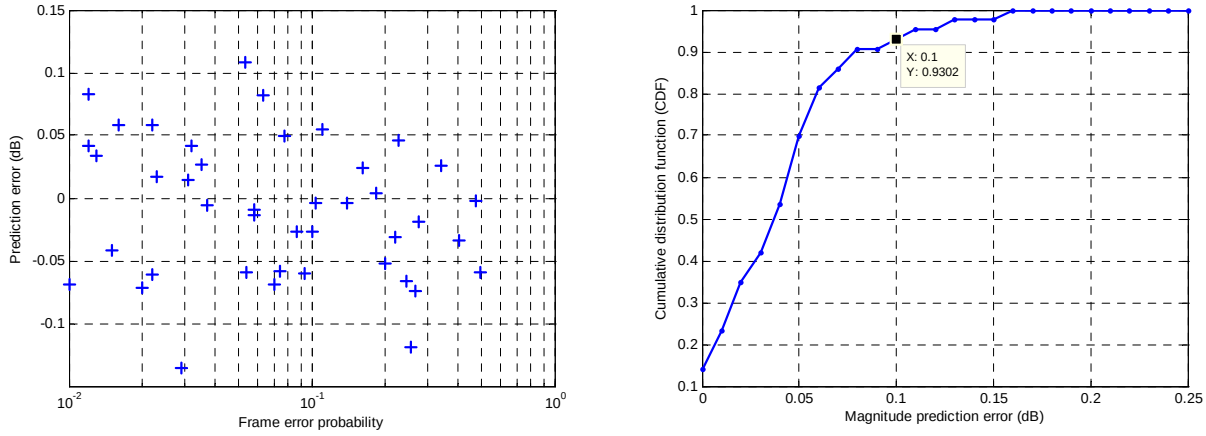

Figure 7-6: Prediction error for RGEES solution with 16QAM modulation.

7.5 Conclusions and Perspectives

In this chapter, we investigated the problem of link quality prediction at the system level for frame oriented channel encoded transmissions over fading channels. Based on the concept of effective SINR, we proposed a new solution called the chi-square effective SINR. This solution assumes a noncentral chi-square distribution for the summation of the instantaneous SINR of the erroneous bits in the frame. Compared to the exponential effective SINR, which

is the most commonly used solution in the literature, we showed that our chi-square solution has slightly lower performance. However, it benefits from an easier implementation and a lower sensitivity to SINR estimation errors since it requires knowledge of the mean and variance of the SINR values, while the exponential solution requires the summation of the exponential of the SINR values over the frame. Through an analysis of the pair-wise error probability of a soft input Viterbi decoder with 16QAM modulation, we proposed refinement for both exponential and chi-square solutions. We showed that the refined solutions improve the performance with no additional complexity.

Future research will be devoted to study the applicability of the proposed effective SINR solutions to turbo-codes, which seems promising since these solutions do not require up to now any knowledge of the channel code characteristics. The applicability to multiple antenna techniques constitutes as well an important issue for future investigations.

7.6 References

[1] A. Alexiou, "WINNER Link to System Interface," *IST-Broadband Air Interfaces (BAI) cluster*, Dec. 8, 2004.

[2] H. Holma, "A Study of UMTS Terrestrial Radio Access Performance," *Ph.D. thesis, Helsinki University of Technology,* Oct. 2003.

[3] A. Tee, S. Yoon, J. Cleveland, "Link-System Interface Simulation Methodologies," *IEEE 802.20 Working Group on Mobile Brodband Wireless Access (MBWA), website: www.ieee802.org/20,* C802.20-04/67, June 2004.

[4] S. Nanda, K. M. Rege, "Frame Error Rates for Convolutional Codes on Fading Channels and the Concept of Effective E_b/N_0," *IEEE Transactions on Vehicular Technology,* vol. 47, no. 4, Nov.1998.

[5] Third Generation Partnership Project 2 (3GPP2), "CDMA2000 Evaluation Methodology," *TSG-C.R1002-0 V1.0*, Dec. 2004.

[6] J. Yuan, W. Feng, B. Vucetic, "Performance of Parallel and Serial Concatenated Codes on Fading Channels," *IEEE Transactions on Communications*, vol. 50, no. 10, pp. 1600-1608, Oct. 2002.

[7] A. J. Viterbi, "Convolutional Codes and Their Performance in Communication Systems," *IEEE Transactions on Communications Technology*, vol. 19, no. 5, pp. 751-772, Oct. 1971.

[8] J. G. Proakis, "Digital Communications," *3rd edition, McGraw-Hill*, 1995.

[9] Third Generation Partnership Project (3GPP), "System-Level Evaluation of OFDM – Further Considerations," *TSG-RAN, WG1 #35, R1-031303*, Nov. 2003.

[10] IST European project MATRICE, "MC-CDMA Transmission Techniques for Integrated Broadband Cellular Systems," *website: www.ist-matrice.org*.

[11] IST European project I-METRA, "Performance Evaluation," *Deliverable D4, website: www.ist-imetra.org*, Sep. 2003.

[12] IST European project 4MORE, "4G MC-CDMA multiple antenna system On chip for Radio Enhancements," *website: www.ist-4more.org*.

[13] Third Generation Partnership Project (3GPP), "Considerations on the System-Performance Evaluation of HSDPA Using OFDM Modulation," *TSG-RAN, WG1 #34, R1-030999*, Oct. 2003.

[14] Third Generation Partnership Project (3GPP), "Feasibility Study for OFDM for UTRAN enhancement," *TSGRAN TR 25.892 V2.0.0*, June 2004.

[15] S. Valle, A. Poloni, G. Villa, "802.11 TGn Proposal for PHY abstraction in MAC simulators," *IEEE 802.11-04/0184*, Feb. 2004.

[16] J. Zander, S. Kim, "Radio Resource Management for Wireless Networks," *Artech House Publishers*, 2001.

Conclusions and Prospects

The thesis addressed the problem of link to system level interface and the evaluation of the capacity performances of MC-CDMA physical layer algorithms and configurations in the downlink of a multi-cellular environment. Two kinds of link to system level interfaces were investigated, namely, the multi-frame and frame oriented interfaces.

For the multi-frame oriented interface, we showed that the local mean SINR at the output of the detection module can be used to predict the average BER and FER at the system level. Thanks to analytical derivation of the intra-cell and inter-cell interference power factors, the local mean SINR can easily and accurately be evaluated at the system level. Moreover, thanks to the OGN and AWGN models proposed respectively for the intra-cell multiple access signal at the transmitter and the inter-cell interference at the receiver, we developed an accurate and low complexity multi-frame oriented link to system level interface simulator in order to provide the mappings between the local mean SINR and average BER and FER. These mappings were shown to be generally specific not only to the given physical layer configuration and channel model but also to the cell load.

Using the multi-frame oriented interface, we then presented a semi-analytical methodology to evaluate the capacity benefits of MC-CDMA physical layer algorithms and configurations in the downlink of an urban macro-cellular environment. The cellular capacity is defined as the maximum number of users that can be served simultaneously by the central base station with a given average FER transmission quality requirement. The capacity was evaluated at both the link and system levels respectively through a novel link level capacity indicator and Monte-Carlo system level simulations. The results provided by both capacity evaluation approaches were checked to be consistent with each other, although the Monte Carlo system level simulation approach is more accurate. In particular, the novel link level capacity indicator was shown to concisely and quantitatively capture the main effects impacting the cellular capacity, namely, the diversity gain and MAI reduction.

The capacity performances of different MC-CDMA configurations were evaluated using the urban ETSI BRAN E channel model. It was shown that in particular, adjacent frequency chip mapping (AFM) is more suitable than interleaved frequency mapping (IFM) to achieve high capacity values. This suggests that the trade-off between MAI and diversity is to favor MAI reduction rather than diversity gain, which is an important conclusion for MC-CDMA system design. Furthermore, it was shown that MMSEC equalization technique generally

provides higher capacity than MRC and EGC techniques. On the other hand, we found that using high performance channel coding schemes such as turbo codes results in a significant cellular capacity gain. As well, we found that for a given transmit power, QPSK modulation outperforms 16QAM modulation in the range of throughputs reachable by QPSK modulation. However, for higher cellular throughputs, 16QAM should be used but at the expense of higher transmission power. The methodology developed in this thesis allows to evaluate the capacity performances of other MC-CDMA algorithms and configurations, as well as other physical layers. This methodology enables identifying the best suited physical layer algorithms and configurations for a given environment, i.e., those providing the best performance for the whole cellular system. It is worth pointing out that such algorithm classification cannot be always anticipated by traditional link level approaches.

For the frame oriented interface, we investigated adequate link quality measures that allow accurate prediction of the short term error probability for frame oriented channel encoded transmissions over fading channels. Physical layer abstraction with such small granularity is relevant for dynamic system level simulations, e.g., to evaluate the impact of physical layer and upper layers mechanisms on the whole system performance, but also to implement efficient link adaptation algorithms in real systems. Based on the concept of effective SINR, we studied some state of the art solutions and proposed novel solutions, namely, GCES, RGCES, and RGEES. The RGCES and RGEES are refinements of the new GCES solution and the GEES state of the art solution respectively. The GCES (RGCES) solution assumes a noncentral chi-square distribution for the summation of instantaneous SINR for the erroneous bits in the frame, while the GEES (RGEES) assumes independent instantaneous SINR for the erroneous bits in the frame. Performance evaluation showed that the proposed GCES solution performs slightly lower than GEES solution but it benefits from a lower implementation complexity and lower sensitivity to SINR estimation errors. We also showed that the proposed refinements RGCES and RGEES improve the performances of GCES and GEES with no additional complexity.

Prospects

The thesis provided a framework that naturally extends to investigate future research topics of interest among which we mention the following:

- Evaluation of the cellular capacity benefits of *Multiple Input Multiple Output* (MIMO) multiple antenna techniques in the context of MC-CDMA systems.

- Evaluation of the cellular capacity for other physical layers and comparison with MC-CDMA, in particular, *Orthogonal Frequency Division Multiple Access* (OFDMA), which is another promising technique for future broadband 4G systems.
- Study of the applicability of the proposed effective SINR solutions to turbo-codes and MIMO multiple antenna techniques.
- Development of a dynamic system level simulator using the frame oriented interface for accurate and realistic capacity evaluation and for proper development of RRM and link adaptation algorithms.

Appendix A

Mobile Radio Channel

A.1. Power Delay Profile of ETSI BRAN E Channel Model

The urban ETSI BRAN E channel model has the following power delay profile when sampled at frequency f_s = 57.6 MHz.

Delay τ_p (ns)	Variance $2\sigma_p^2$ (dB)
0	-4.90
17.361	-2.71
34.722	-0.72
69.444	-1.29
104.167	-1.70
138.889	-0.28
190.972	-1.22
243.056	-2.00
312.5	0.10
434.028	-1.93
555.556	-2.74
711.805	-5.42
885.417	-7.37
1076.389	-10.66
1284.722	-13.45
1510.417	-17.40
1753.472	-20.92

Table A-1: Power delay profile of the urban ETSI BRAN E channel model.

A.2. Simulation Approach with Doppler

In this section, we present the simulation approach used for generating the time variant channel transfer function $H(t,f)$ with Jakes Doppler power spectrum (cf. (2.30)). The main idea here is to filter a frequency domain white Gaussian random process $w_p(\nu)$ by the square root of the Jakes Doppler spectrum denoted by $SQRJ(\nu)$. The subscript p in $w_p(\nu)$ designates the p-th multi-path component.

In the frequency domain ν, filtering is simply achieved by multiplying $w_p(\nu)$ by $SQRJ(\nu)$. The inverse Fourier transform of the multiplication result gives the p-th time variant complex gain $g_p(t)$, which has the form

$$g_p(t) = \int_{-\infty}^{+\infty} w_p(\nu) SQRJ(\nu) \exp(j2\pi\nu t) d\nu \tag{A.1}$$

The spaced-time correlation function of $g_p(t)$ is then obtained as

$$\begin{aligned} \Gamma_p(\Delta t) = \frac{1}{2} E\{g_p(t) g_p^*(t-\Delta t)\} &= \sigma_p^2 \int_{-\infty}^{+\infty} SQRJ^2(\nu) \exp(j2\pi\nu\Delta t) d\nu \\ &= \sigma_p^2 \, \mathrm{J}_0(2\pi f_d \Delta t) \end{aligned} \tag{A.2}$$

The summation of all the N_p spaced-time correlations $\{\Gamma_p(\Delta t)\}$ gives

$$\Gamma_H(\Delta t) = \frac{1}{2} E\{H(t,f) H^*(t-\Delta t, f)\} = \mathrm{J}_0(2\pi f_d \Delta t) \tag{A.3}$$

where J_0 is the zero order Bessel function of the first kind given in (2.29).

A sketch diagram of the channel simulation approach is depicted in Figure A-1 below. The input parameters are: the power delay profile with delays $\{\tau_p\}$ and variances $\{\sigma_p^2\}$ of the N_p multi-path components, the maximum Doppler frequency f_d, and the discrete time vector **t** and frequency vector **f**. At first, the square root of the Jakes Doppler power spectrum **SQRJ**(**ν**) is calculated for a discrete Doppler frequency vector **ν**. Then, for each multi-path component p, a zero mean complex-valued Gaussian random vector $\mathbf{w_p}$ is generated with variance $2\sigma_p^2$ and then element-wise multiplied by **SQRJ**(**ν**), which results in vector $\mathbf{v_p}$. The p-th time variant complex gain $\mathbf{g_p}(\mathbf{t})$ is then determined from the inverse Fourier transform of $\mathbf{v_p}(\boldsymbol{\nu})$. The time variant transfer function $H(t_m,f_n)$ at time t_m and frequency f_n is then obtained as

$$H(t_m, f_n) = \sum_{p=0}^{N_p-1} g_p(t_m) \mathrm{e}^{-j2\pi f_n \tau_p} \tag{A.4}$$

Equation (A.4) represents the Fourier transform with respect to the time delay τ of the time variant channel impulse response.

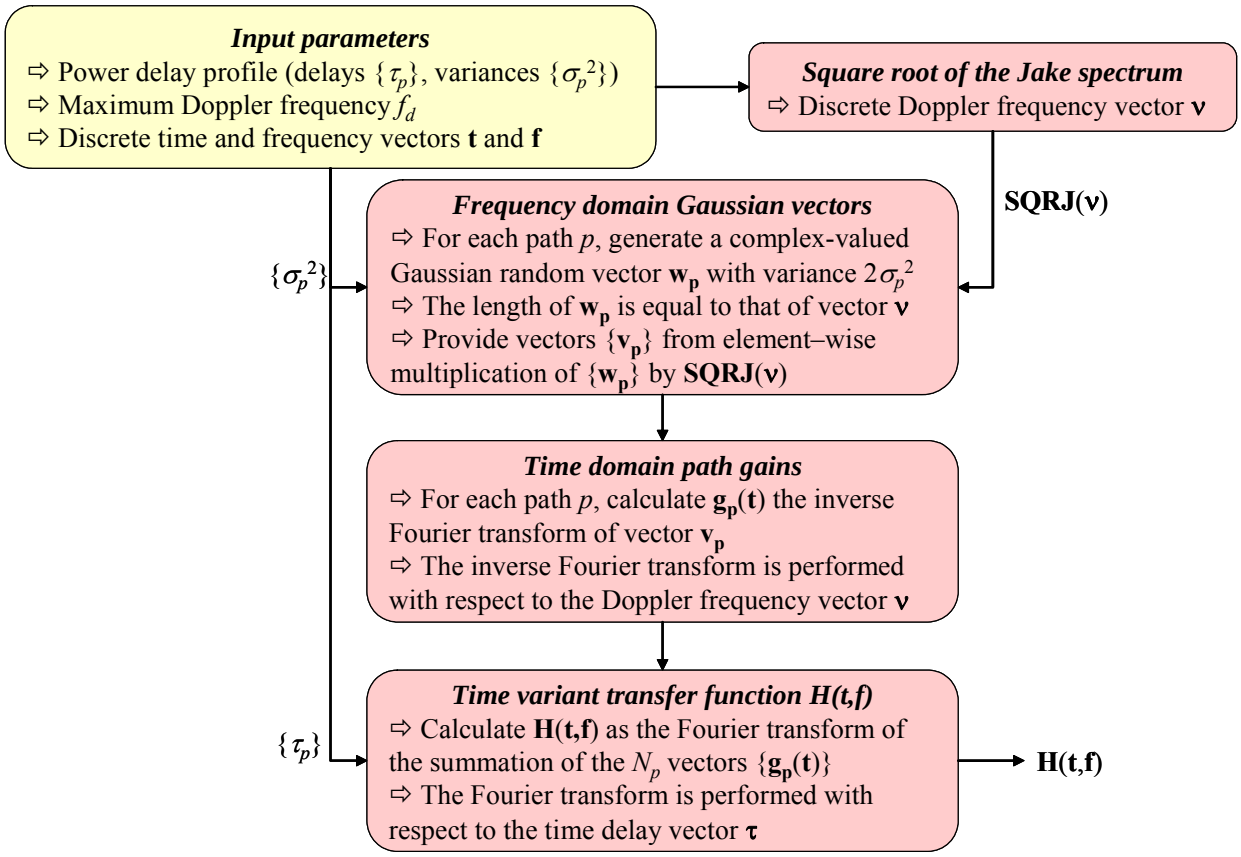

Figure A-1: Sketch diagram of the channel simulation approach with Doppler.

Appendix B

Log Likelihood Ratios

This appendix presents the calculation of the log likelihood ratios (LLR) for QPSK and 16QAM modulations with Gray mapping. The decision variable has the form (cf. (7.7))

$$\hat{d}_n = A_n d_n + \nu_n \tag{B.1}$$

where $A_n > 0$ denotes the equalized channel gain affecting the transmitted data symbol d_n, and ν_n denotes the interference plus noise experienced by data symbol d_n, which is modeled by a zero mean complex-valued Gaussian random variable of variance σ_n^2.

Assuming equal a priori probabilities $\Pr\{b_n^{(i)} = 1\} = \Pr\{b_n^{(i)} = 0\}$, The LLR of the bit $b_n^{(i)}$ in the binary representation of data symbol d_n is given by

$$y_n^{(i)} = \log\left(\frac{\Pr\left\{\hat{d}_n \middle| b_n^{(i)} = 1\right\}}{\Pr\left\{\hat{d}_n \middle| b_n^{(i)} = 0\right\}} \right) \tag{B.2}$$

B.1. Case of QPSK Modulation

In the case of QPSK modulation, the binary representation of data symbol d_n is $b_n^{(1)} b_n^{(2)}$. As shown in Figure 4-2, $b_n^{(1)}$ is equal to 0 for the two constellation points for which real parts are equal to $+1/\sqrt{2}$ and it is equal to 1 for the two other points for which real parts are equal to $-1/\sqrt{2}$. Thus, we can write

$$\Pr\left\{\hat{d}_n \middle| b_n^{(1)} = 0\right\} = \frac{1}{2} \sum_{d \,\middle|\, \Re(d) = \frac{1}{\sqrt{2}}} \frac{1}{\pi \sigma_n^2} \mathrm{e}^{-\frac{\left|\hat{d}_n - A_n d\right|^2}{\sigma_n^2}} \tag{B.3}$$

After some simplifications, (B.3) reduces to

$$\Pr\left\{\hat{d}_n \middle| b_n^{(1)} = 0\right\} = \frac{1}{2\pi\sigma_n^2} \mathrm{e}^{-\frac{\left|\Re\left(\hat{d}_n\right) - A_n \frac{1}{\sqrt{2}}\right|^2}{\sigma_n^2}} \left(\mathrm{e}^{-\frac{\left|\Im\left(\hat{d}_n\right) - A_n \frac{1}{\sqrt{2}}\right|^2}{\sigma_n^2}} + \mathrm{e}^{-\frac{\left|\Im\left(\hat{d}_n\right) + A_n \frac{1}{\sqrt{2}}\right|^2}{\sigma_n^2}} \right) \tag{B.4}$$

In the same way, we obtain

$$\Pr\left\{\hat{d}_n \middle| b_n^{(1)}=1\right\}=\frac{1}{2\pi\sigma_n^2}\mathrm{e}^{-\frac{\left|\Re\left(\hat{d}_n\right)+A_n\frac{1}{\sqrt{2}}\right|^2}{\sigma_n^2}}\left(\mathrm{e}^{-\frac{\left|\Im\left(\hat{d}_n\right)-A_n\frac{1}{\sqrt{2}}\right|^2}{\sigma_n^2}}+\mathrm{e}^{-\frac{\left|\Im\left(\hat{d}_n\right)+A_n\frac{1}{\sqrt{2}}\right|^2}{\sigma_n^2}}\right) \tag{B.5}$$

By substituting (B.5) and (B.4) into (B.2), we obtain the LLR $y_n^{(1)}$ for the bit $b_n^{(1)}$ as

$$y_n^{(1)}=\frac{-2\sqrt{2}A_n\Re\left(\hat{d}_n\right)}{\sigma_n^2} \tag{B.6}$$

Following the same procedure, we obtain the LLR $y_n^{(2)}$ for the bit $b_n^{(2)}$ as

$$y_n^{(2)}=\frac{-2\sqrt{2}A_n\Im\left(\hat{d}_n\right)}{\sigma_n^2} \tag{B.7}$$

B.2. Case of 16QAM Modulation

In the case of 16QAM modulation, the binary representation of data symbol d_n becomes $b_n^{(1)}b_n^{(2)}b_n^{(3)}b_n^{(4)}$. Starting with bit $b_n^{(1)}$, as shown in Figure 4-2, this bit is equal to 0 for the 8 constellation points for which real parts are positive and it is equal to 1 for the 8 other points for which real parts are negative. Thus, we have

$$\Pr\left\{\hat{d}_n \middle| b_n^{(1)}=0\right\}=\frac{1}{8}\sum_{d|\Re(d)>0}\frac{1}{\pi\sigma_n^2}\mathrm{e}^{-\frac{\left|\hat{d}_n-A_nd\right|^2}{\sigma_n^2}} \tag{B.8}$$

From (B.8) and after some simplifications, the LLR $y_n^{(1)}$ can exactly be found equal to

$$y_n^{(1)}=\log\left(\frac{\mathrm{e}^{-\frac{\left|\Re\left(\hat{d}_n\right)+A_n\frac{1}{\sqrt{10}}\right|^2}{\sigma_n^2}}+\mathrm{e}^{-\frac{\left|\Re\left(\hat{d}_n\right)+A_n\frac{3}{\sqrt{10}}\right|^2}{\sigma_n^2}}}{\mathrm{e}^{-\frac{\left|\Re\left(\hat{d}_n\right)-A_n\frac{1}{\sqrt{10}}\right|^2}{\sigma_n^2}}+\mathrm{e}^{-\frac{\left|\Re\left(\hat{d}_n\right)-A_n\frac{3}{\sqrt{10}}\right|^2}{\sigma_n^2}}}\right) \tag{B.9}$$

Two cases are distinguished depending on whether $\Re\left(\hat{d}_n\right)$ is greater or less than 0. When $\Re\left(\hat{d}_n\right) < 0$, we approximate the denominator of the ratio in (B.9) by its dominant term, which is the first term. This approximation assumes a relatively low variance σ_n^2. The LLR in (B.9) can then be expressed as

$$y_n^{(1)} = \log\left(\mathrm{e}^{-\frac{4A_n \Re\left(\hat{d}_n\right)}{\sigma_n^2\sqrt{10}}} + \mathrm{e}^{-\frac{4A_n}{\sigma_n^2\sqrt{10}}\left(2\Re\left(\hat{d}_n\right)+\frac{2A_n}{\sqrt{10}}\right)} \right) \tag{B.10}$$

Now, we consider the following approximation

$$\log\left(\mathrm{e}^a + \mathrm{e}^b\right) \approx \max(a,b) \tag{B.11}$$

By applying (B.11) to (B.10), we obtain

$$y_n^{(1)} = \begin{cases} \dfrac{-4A_n \Re\left(\hat{d}_n\right)}{\sigma_n^2\sqrt{10}} & \text{for} \quad \dfrac{-2A_n}{\sqrt{10}} < \Re\left(\hat{d}_n\right) < 0 \\ -\dfrac{4A_n}{\sigma_n^2\sqrt{10}}\left(2\Re\left(\hat{d}_n\right)+\dfrac{2A_n}{\sqrt{10}}\right) & \text{for} \quad \Re\left(\hat{d}_n\right) < \dfrac{-2A_n}{\sqrt{10}} \end{cases} \tag{B.12}$$

In the region where $\Re\left(\hat{d}_n\right) < \dfrac{-2A_n}{\sqrt{10}}$, the LLR $y_n^{(1)}$ is sufficiently large so that the risk of error is very small. Thus, in this region, an underestimation of $y_n^{(1)}$ by $\dfrac{-4A_n \Re\left(\hat{d}_n\right)}{\sigma_n^2\sqrt{10}}$ will have negligible impact on the performances. Taking this into account, (B.12) reduces to

$$y_n^{(1)} = \frac{-4A_n \Re\left(\hat{d}_n\right)}{\sigma_n^2\sqrt{10}} \quad \text{for} \quad \Re\left(\hat{d}_n\right) < 0 \tag{B.13}$$

Now when $\Re\left(\hat{d}_n\right) > 0$, we approximate the numerator of the ratio in (B.9) by its dominant term, which is the first term. This approximation yields

$$y_n^{(1)} = -\log\left(\mathrm{e}^{\frac{4A_n \Re\left(\hat{d}_n\right)}{\sigma_n^2\sqrt{10}}} + \mathrm{e}^{\frac{4A_n}{\sigma_n^2\sqrt{10}}\left(2\Re\left(\hat{d}_n\right)-\frac{2A_n}{\sqrt{10}}\right)} \right) \tag{B.14}$$

Using the approximation given in (B.11), (B.14) reduces to

$$y_n^{(1)} = \begin{cases} \dfrac{-4A_n \Re\left(\hat{d}_n\right)}{\sigma_n^2\sqrt{10}} & \text{for} \quad 0 < \Re\left(\hat{d}_n\right) < \dfrac{2A_n}{\sqrt{10}} \\ -\dfrac{4A_n}{\sigma_n^2\sqrt{10}}\left(2\Re\left(\hat{d}_n\right)-\dfrac{2A_n}{\sqrt{10}}\right) & \text{for} \quad \Re\left(\hat{d}_n\right) > \dfrac{2A_n}{\sqrt{10}} \end{cases} \tag{B.15}$$

Similarly to (B.13), since underestimating $y_n^{(1)}$ by $\frac{-4A_n\Re\left(\hat{d}_n\right)}{\sigma_n^2\sqrt{10}}$ for $\Re\left(\hat{d}_n\right) > \frac{2A_n}{\sqrt{10}}$ will have a negligible impact on the performances, we consider $y_n^{(1)}$ equal to

$$y_n^{(1)} = \frac{-4A_n\Re\left(\hat{d}_n\right)}{\sigma_n^2\sqrt{10}} \quad \text{for} \quad \Re\left(\hat{d}_n\right) \geq 0 \tag{B.16}$$

Thus, from (B.13) and (B.16), we obtain the following approximated LLR

$$y_n^{(1)} \approx \frac{-4A_n\Re\left(\hat{d}_n\right)}{\sigma_n^2\sqrt{10}} \tag{B.17}$$

Similarly to $y_n^{(1)}$, the LLR $y_n^{(2)}$ corresponding to the bit $b_n^{(2)}$ can be found as

$$y_n^{(2)} \approx \frac{-4A_n\Im\left(\hat{d}_n\right)}{\sigma_n^2\sqrt{10}} \tag{B.18}$$

Now, considering the bit $b_n^{(3)}$, its LLR $y_n^{(3)}$ can exactly be expressed as

$$y_n^{(3)} = \log\left(\frac{e^{-\frac{\left|\Re\left(\hat{d}_n\right)-A_n\frac{1}{\sqrt{10}}\right|^2}{\sigma_n^2}} + e^{-\frac{\left|\Re\left(\hat{d}_n\right)+A_n\frac{1}{\sqrt{10}}\right|^2}{\sigma_n^2}}}{e^{-\frac{\left|\Re\left(\hat{d}_n\right)-A_n\frac{3}{\sqrt{10}}\right|^2}{\sigma_n^2}} + e^{-\frac{\left|\Re\left(\hat{d}_n\right)+A_n\frac{3}{\sqrt{10}}\right|^2}{\sigma_n^2}}}\right) \tag{B.19}$$

Two cases are distinguished here as well. When $\Re\left(\hat{d}_n\right) < 0$, we approximate the numerator and denominator of the ratio in (B.19) by the second terms, which dominate the first ones. Using the approximation in (B.11), we obtain

$$y_n^{(3)} \approx \frac{4A_n}{\sigma_n^2\sqrt{10}}\left(\Re\left(\hat{d}_n\right) + \frac{2A_n}{\sqrt{10}}\right) \quad \text{for} \quad \Re\left(\hat{d}_n\right) < 0 \tag{B.20}$$

When $\Re\left(\hat{d}_n\right) > 0$, the numerator and denominator of the ratio in (B.19) are approximated by their first terms, which become now the dominant values. Using (B.11), we can write

$$y_n^{(3)} \approx \frac{-4A_n}{\sigma_n^2\sqrt{10}}\left(\Re\left(\hat{d}_n\right) - \frac{2A_n}{\sqrt{10}}\right) \quad \text{for} \quad \Re\left(\hat{d}_n\right) \geq 0 \tag{B.21}$$

Equations (B.20) and (B.21) can then be rewritten with the same equation below

$$y_n^{(3)} \approx \frac{-4A_n}{\sigma_n^2\sqrt{10}}\left(\left|\Re\left(\hat{d}_n\right)\right| - \frac{2A_n}{\sqrt{10}}\right) \tag{B.22}$$

Similarly to $y_n^{(3)}$, the LLR $y_n^{(4)}$ corresponding to the bit $b_n^{(4)}$ is found as

$$y_n^{(3)} \approx \frac{-4A_n}{\sigma_n^2\sqrt{10}}\left(\left|\Im\left(\hat{d}_n\right)\right| - \frac{2A_n}{\sqrt{10}}\right) \tag{B.23}$$

Ecole Nationale Supérieure des Télécommunications de Bretagne
Technopôle Brest Iroise – CS 83818 – 29238 Brest Cedex 3 – France
Tel: +33 (0)2 29 00 10 43 – Fax: +33 (0)2 29 00 10 97
www.enst-bretagne.fr